



Combining bioorthogonal labeling and advanced microscopy to
study GPCR dynamics in intact cells

Master thesis

Presented by

Pauline Sophie Löffler

371845

Submitted to

Technische Universität Berlin

Institut für Biotechnologie

Fachgebiet Angewandte Biochemie

Prof. Dr. Jens Kurreck

(1. Examiner)

Performed at:

Max Delbrück Center for Molecular Medicine

Research Group:

AG Receptor Signaling

Supervised by:

Prof. Dr. Paolo Annibale

(2. Examiner)

Berlin, January 10, 2022

Eidesstattliche Erklärung

Ich versichere hiermit an Eides Statt, dass ich die von mir eingereichte Masterarbeit selbständig verfasst und ausschließlich die angegebenen Hilfsmittel und Quellen verwendet habe.

Declaration of originality

I hereby declare that this thesis and the work described in it are my own work, unaided except as may be specified below, and that the thesis does not contain material that has already been used to any substantial extent for a comparable purpose.

Berlin, January 10, 2022



(Pauline Löffler)

Contents

Abbreviations	V
1. Abstract	VII
2. Zusammenfassung	VIII
3. Introduction	1
3.1. Aim of this Thesis	1
3.2. G protein coupled receptor (GPCR)s and their signaling pathways	2
3.3. Linking the receptor diffusion behaviour to its activation status	5
3.4. The incorporation of a non-canonical amino acid (ncAA) and bio-orthogonal labeling	7
3.5. Microscopy	8
3.5.1. total internal reflection fluorescence (TIRF) microscopy and single molecule tracking (SMT)	9
3.5.2. Confocal microscopy	9
3.6. Analyzing the membrane receptor behaviour with Fluorescence correlation spectroscopy (FCS)	10
3.6.1. Fluorescence correlation spectroscopy (FCS) compared to other common methods	10
3.6.2. Diffusion and the Mean Square Displacement (MSD)	11
3.6.3. Autocorrelation	12
3.6.4. The correlation of fluctuations and the spatiotemporal image correlation spectroscopy (STICS) function	13
3.7. Python	16
4. Materials and Methods	17
4.1. Materials	17
4.2. Methods	22
4.2.1. Cell culture	22
4.2.2. Transfection	22
4.2.3. Construction of the M2 receptor variants	23
4.2.4. Fragment production by Polymerase chain reaction and gel electrophoresis	23

4.2.5. Cloning	24
4.2.6. Site-directed Mutagenesis	25
4.2.7. Transformation	25
4.2.8. Plasmid Miniprep	25
4.2.9. Plasmid Midiprep	26
4.2.10. Enzyme-linked Immunosorbent Assay	26
4.2.11. Microscopy	27
4.2.11.1. Line scan microscopy	27
4.2.11.2. Single Molecule Tracking	28
4.2.12. Functionality Assay	29
4.2.13. Programming in Python	30
5. Results	31
5.1. Expression of the human M2 muscarinic acetylcholine receptor (M2R)-Amber-mutant	31
5.2. Functionality of the human M2 muscarinic acetylcholine receptor (M2R)-Amber-mutant	35
5.3. Developing a Python3 script for line-scan analysis	39
5.3.1. Verifying the results of the Python-implemented line-scan analysis	44
5.4. Analysing the diffusion behaviour of the M2R-Amber-mutated at AA-position 8 (M2R-Mut8) - Cy3	46
5.5. Analysing the diffusion behaviour of the M2R-Amber-mutated at AA-position 8 (M2R-Mut8) upon receptor activation	54
5.6. Analysing the diffusion behaviour with single molecule tracking (SMT)	57
6. Discussion	60
6.1. A functional Python script for line scan (LS)-Fluorescence correlation spectroscopy (FCS) analysis was developed	60
6.2. A data-preselection was shown to be unnecessary and the analysis could thus be performed user-bias free	62
6.3. The single molecule tracking (SMT) does not record a change in diffusion behaviour upon receptor activation	62
6.4. The human M2 muscarinic acetylcholine receptor (M2R) was successfully expressed and labelled at amino acid position 8	63
6.5. The M2R-Amber-mutated at AA-position 8 (M2R-Mut8) shows clear compartmentalization and a considerable cell-to-cell variability	64
6.6. The diffusion behaviour of the M2R-Amber-mutated at AA-position 8 (M2R-Mut8) might support the hypothesis of G protein pre-coupling	65
7. Outlook	66

8. Acknowledgements	67
Appendix	68
A. Expression and functionality of the human M2 muscarinic acetylcholine receptor (M2R)-Amber-mutant	68
B. Developing a Python3 script for line-scan analysis	69
C. Verifying the results of the Python-implemented line-scan analysis	71
D. Analysing the diffusion behaviour of the M2R-Amber-mutated at AA-position 8 (M2R-Mut8) - Cy3 with the Python script	73
E. Analysing the diffusion behaviour of the M2R-Amber-mutated at AA-position 8 (M2R-Mut8) upon receptor activation	77
F. Settings to be checked and adapted by the user	86

Abbreviations

AC Autocorrelation

ACh Acetylcholine

BSA Bovine serum albumin

cAMP Cyclic adenosine monophosphate

CFP Cyan Fluorescent Protein

DMSO Dimethylsulfoxid

EDTA Ethylenediaminetetraacetic acid

EGFP Enhanced green fluorescent protein

EKAR Extracellular signal-regulated kinase activity reporter

ELISA Enzyme-linked Immunosorbent Assay

ERK Extracellular signal-regulated kinase

FBS Fetal bovine serum

FCS Fluorescence correlation spectroscopy

FRAP Fluorescence recovery after photobleaching

FRET Fluorescence resonance energy transfer

GDP Guanosine diphosphate

GPCR G protein coupled receptor

GRK G protein-coupled receptor kinases

GTP Guanosine triphosphate

HA Human influenza hemagglutinin

LS Line scan

LSCM Laser scanning confocal microscope

M2R Human M2 muscarinic acetylcholine receptor

M2R-Mut8 M2R-Amber-mutated at AA-position 8

mGluR3 Metabotropic glutamate receptor 3

MSD Mean Square Displacement

ncAA Non-canonical amino acid

PBS Phosphate-buffered saline

PSF Point Spread Function

PTX Pertussis toxin

ROI Region of interest

RT Room temperature

SMT Single molecule tracking

SPIEDAC Strain-promoted inverse electron-demand Diels-Alder cycloaddition

STICS Spatiotemporal image correlation spectroscopy

STICS Spatiotemporal image correlation spectroscopy

TCO*A Trans-Cyclooct-2-en-L-Lysine

Tet-Cy3 Cy3-Tetrazine

Tet-Cy5 Cy5-Tetrazine

TIRF Total internal reflection fluorescence

wt Wild-type

YFP Yellow Fluorescent Protein

1. Abstract

G protein coupled receptors (GPCRs) are the largest and most diverse group of membrane receptors. They are involved in countless essential cell and body functions and therefore, also a popular drug target. Despite being a mainstream research target over the last 40 years, they remain an attractive research focus given the rich modulation of the signalling canon that can be observed in the complex environment of the cell membrane. However, many of the intricacies of G protein coupled receptor (GPCR) signalling are still to be investigated. For this reason, we decided to study the dynamics of the prototypical GPCR human M2 muscarinic acetylcholine receptor (M2R) using a minimally invasive labeling technique, combined with advanced microscopy.

Specifically, we show, that the receptor was successfully mutated to incorporate a non-canonical amino acid (ncAA) at position eight from the N-terminus. Thus, enabling the minimal invasive bioorthogonal labeling of the M2R for subsequent diffusion analysis experiments via Fluorescence correlation spectroscopy (FCS). The M2R was also proven to be still able to induce downstream signalling upon activation and thus was shown to have preserved its functionality also in the mutated version.

The subsequent FCS experiments investigated the diffusion behaviour of the M2R-Mut8 both without stimulus and under Acetylcholine (ACh) stimulation. Additionally, the same conditions were tested under Pertussis toxin (PTX) treatment, thus disrupting the downstream G protein signalling. The extracted data suggests a possible influence of the G protein coupling onto the receptor diffusion coefficient as the PTX treated samples showed a considerably lower diffusion coefficient than the non-treated samples. In the untreated samples, the diffusion rate of the M2R was observed to become slower upon activation by the agonist. Further experiments are needed to confirm this assessment. Pilot experiments using single molecule tracking (SMT) were also performed to observe the behavior of the receptor in the isolated, single molecule regime.

The data analysis of the line scan (LS)-FCS experiments within this thesis was realized by the development of a Python3 script. This enables the user to either analyse individual LSs or perform an averaged analysis over several samples of a certain condition. The script was proven to generate reliable analysis results by comparing it to the analysis of standard datasets, stored in public repositories and previously analysed with established algorithms.

2. Zusammenfassung

G Protein-gekoppelte Rezeptoren (GPCRs) sind die größte und vielfältigste Gruppe von Membranrezeptoren. Sie sind an unzähligen wichtigen Zell- und Körperfunktionen beteiligt und daher auch ein beliebtes Ziel für Arzneimittel. Obwohl sie in den letzten 40 Jahren intensiv erforscht wurden, sind sie nach wie vor ein attraktiver Forschungsschwerpunkt, da sich in der komplexen Umgebung der Zellmembran zahlreiche Modulationen des Signalkanons beobachten lassen. Viele der Feinheiten der Signalweiterleitung sind jedoch noch nicht erforscht. Aus diesem Grund haben wir uns entschlossen, die Dynamik des prototypischen GPCR M2R mit Hilfe einer minimal invasiven Labelingtechnik in Kombination mit hochspezialisierten Mikroskopietechniken zu untersuchen.

Konkret zeigen wir, dass der Rezeptor erfolgreich mutiert wurde, um eine nicht-kanonische Aminosäure an Position acht des N-Terminus einzubauen. Dies ermöglicht die minimal invasive bioorthogonale Markierung des M2R für anschließende Diffusionsanalyseexperimente mittels Fluoreszenzkorrelationsspektroskopie (FCS). Außerdem zeigen wir, dass der mutierte M2R bei Aktivierung immer noch in der Lage ist, nachgeschaltete Signalwege zu induzieren. Somit hat er seine Funktionalität auch in der mutierten Version beibehalten.

In den anschließenden FCS-Experimenten wurde das Diffusionsverhalten des M2R-Mut8 sowohl ohne Stimulus als auch unter Acetylcholin-Stimulation untersucht. Zusätzlich wurden die gleichen Bedingungen nach Pertussis toxin (PTX)-Behandlung getestet, wodurch die nachgeschaltete G Protein-Signalkaskade unterbrochen wurde. Die extrahierten Daten deuten auf einen möglichen Einfluss der G Protein-Kopplung auf den Rezeptordiffusionskoeffizienten hin, da die mit Pertussis toxin (PTX) behandelten Proben einen deutlich niedrigeren Diffusionskoeffizienten aufwiesen als die unbehandelten Proben. In den unbehandelten Proben wurde beobachtet, dass die Diffusionsrate des M2R bei Aktivierung durch den Agonisten sinkt. Weitere Experimente sind erforderlich, um diese Einschätzung zu bestätigen. Es wurden auch Pilotexperimente mit Einzelpartikelverfolgung durchgeführt, um das Verhalten des Rezeptors im isolierten Einzelmolekülregime zu beobachten.

Die Datenanalyse der FCS-Experimente im Rahmen dieser Arbeit wurde durch die Entwicklung eines Python3-Skripts realisiert. Dieses ermöglicht es dem Benutzer, entweder einzelne Experimente zu analysieren oder eine gemittelte Analyse über mehrere Experimente einer bestimmten Bedingung durchzuführen. Es wurde nachgewiesen, dass das Skript zuverlässige Analyseergebnisse liefert, indem es mit der Analyse von Standarddatensätzen verglichen wurde, die

in öffentlichen Datenbanken gespeichert sind und zuvor mit etablierten Algorithmen analysiert wurden.

3. Introduction

3.1. Aim of this Thesis

G protein coupled receptors (GPCRs) are the largest and most diverse group of membrane receptors[1], [2]. They transduce a multitude of extra- to intra-cellular signaling. Therefore, they are also a very interesting and important drug target[3]. GPCRs recognize extracellular signals and translate them to a coordinated second messenger response and downstream signaling pathways [4]. While the range of different signals is huge and encompasses anything from light to ions and small molecules to hormones, the underlying mechanism of conformational change of the receptor and subsequent G protein signaling pathway is largely conserved as is outlined in section 3.2.

This imbalance of a variety of incoming signals on the one hand and an apparently clearly defined set of intracellular pathways on the other hand, raises the question, how the highly specific cell responses are achieved. To answer this question, one needs to understand the receptor dynamics and signal transduction upon receptor activation in a time and space resolved manner [5]. One piece of this puzzle lies in the investigation of the diffusion behaviour of GPCRs in different activation states. The coupling to a G protein, for example, implies the formation of a complex, that may have distinct diffusional properties compared to the individual components [6]. However, the diffusion of the complex is also influenced by further factors like the cortical actin mesh or the receptors position regarding membrane micro-domains [7]. Many studies targeting the diffusion behaviour of GPCRs have already been performed but they mostly utilize receptor-tagging methods that imply the addition of a fluorescent protein or a self-labeling protein-tag. These tags may have an impact on the receptor behaviour and functionality [8]–[10]. A good alternative is the use of bioorthogonal labeling via the introduction of a ncAA, as this strategy allows a minimal invasive labeling of the receptor[8], [10]. The minimally invasive nature of the bioorthogonal label becomes evident when comparing the molecular mass introduced by this labeling strategy compared to other common methods. Incorporating the here used ncAA together with the click-dye adds an additional molecular mass of about 1.1 kDa (0.3 kDa trans-Cyclooct-2-en-L-Lysine (TCO*A) [11] and 0.8 kDa Cy3-Tetrazine (Tet-Cy3) [12]) to the M_{2R} of about 50 kDa. Introducing the widely used enhanced green fluorescent protein (EGFP) or a SNAP-tag instead, means adding 27 kDa or 20kDa to the receptor [13], [14].

Therefore, the aim of this thesis was to investigate the diffusion behaviour of the prototypical

G_i -coupled M2R using FCS, developing on the measurements originally provided in “Quantitative Single-Residue Bioorthogonal Labeling of G Protein-Coupled Receptors in Live Cells” [10]. To achieve this goal, the M2R needed to be labelled by genetic incorporation of TCO*A and subsequent cycloaddition of Tet-Cy3 as further introduced in section 3.4. This mutated and labelled receptor needed to be checked for functionality and was subsequently used for line-scan diffusion-analysis experiments, as described in more detail in section 3.5.2 [15]–[17]. One of the goals of my thesis was to develop an open-source, freely downloadable script for LS analysis based on Python 3. This script, working on the principles of spatiotemporal image correlation spectroscopy (STICS), as explained in detail in section 3.6.4, needed also to be tested on functionality by applying it to data of known outcome and was afterwards used for analysis of receptor diffusion behaviour.

3.2. GPCRs and their signaling pathways

G protein coupled receptor (GPCR)s are remarkable in their diversity of functions in the human body. They control hormone responses, enable us to see, smell and taste and regulate pain [1]. This makes them very interesting for basic research as well as for drug development. Roughly one-third of the approved drugs in the US already target GPCRs, including well-known examples like Candesartan (Angiotensin II Receptor Type 1, high blood pressure treatment) or Lorazepam (GABA receptors, status epilepticus)[18]. As the superfamily of GPCRs comprises a large diversity of primary structures, it can be subdivided into five main families that each can be identified by sharing a common and distinct set of highly conserved residues and motifs: The Glutamate-, Rhodopsin-, Adhesion-, Frizzled/Taste2- and Secretin-family. The Rhodopsin family is the largest of those with around 670 full-length human receptor proteins, one of them being the M2R studied here [2].

Despite the differences, all members of the superfamily share a common basic quaternary structure of seven transmembrane helices [1] that enables them to relay information from the outside of the cell to the inside by 'allosteric coupling'. This means that an extracellular ligand binding leads to conformational changes in the receptor protein which in turn allosterically favours the binding and activating of G proteins at the intracellular site of the receptor [19], [20]. This common mechanism and the entailing different downstream effects are summarized in figure 3.1.

The ligand binds to the GPCR and induces the conformational change (most pronounced a outward swing of the transmembrane domain 6[19]) that favours the binding of the G protein. The inactive heterotrimeric G protein (comprising the guanosine diphosphate (GDP)-carrying α -subunit, the β -subunit and the γ -subunit) binds to the receptor. This results in the α -subunit releasing the previously bound GDP in exchange for a guanosine triphosphate (GTP)[6]. This exchange leads to the dissociation of the G protein from the receptor, leaving it free to activate the next G protein and thus amplify the incoming signal. The G protein disassembles into the

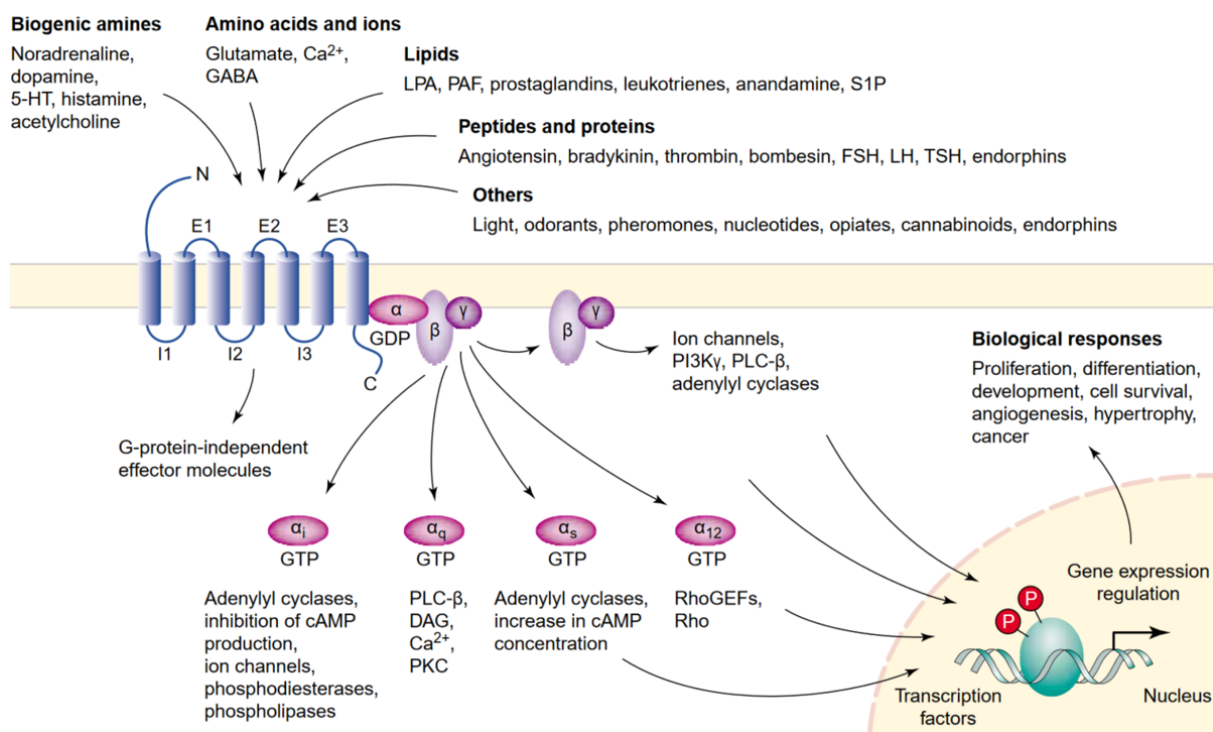


Figure 3.1.: Overview of the GPCR activation and subsequent G protein downstream effects.

GPCRs can get activated by a plethora of different ligands, including biogenic amines, amino acids, peptides and ions, lipids and many others like photons or pheromones. The ligand binding enables G protein binding by allosteric coupling. The G protein in the receptor bound conformation can exchange guanosine diphosphate (GDP) against guanosine triphosphate (GTP) and thus changes into the activated status. It dissociates from the GPCR, divided into the α -subunit and the $\beta\gamma$ -heterodimer. These entities induce diverse and partly divergent effects in the cell depending on the subunit-family they belong to, for example, Adenylyl cyclase activation in case of $\text{G}\alpha_s$ or Adenylyl cyclase inhibition in case of $\text{G}\alpha_i$.

Adapted from: "G-protein-coupled receptors and signaling networks" by Marinissen and Gutkind[6]

α -subunit, now carrying the GTP, and the $\beta\gamma$ -heterodimer. The effects they now induce in the cell depend on the families of the G protein subunits. There are four main families of the $\text{G}\alpha$ -subunit: $\text{G}\alpha_s$, $\text{G}\alpha_{i/o}$, $\text{G}\alpha_{q/11}$ and $\text{G}\alpha_{12/13}$. Each of those consisting of various members with specific expression patterns throughout the body [21].

The downstream effects of those subunits are again summarized in figure 3.1 and can be very divergent. While the $\text{G}\alpha_s$ for example activates the Adenylyl cyclase, and thus enhances cyclic adenosine monophosphate (cAMP) production, the $\text{G}\alpha_i$ instead inhibits it and therefore lowers the cAMP production. The M2R is a classical $\text{G}\alpha_i$ coupling receptor.

The $\text{G}\beta\gamma$ -heterodimer also induces diverse downstream effects after dissociation from the $\text{G}\alpha$ -subunit (figure 3.1). For example, in case of the M2R, the released $\text{G}\beta\gamma$ -heterodimer can slow the heart rate by activating G protein-activated inward rectifier K⁺ (GIRK) ion channels [22], but it can also interact with the G protein-coupled receptor kinases (GRK)s, thereby localize them at the membrane near their target and thus influence the receptor trafficking as described below.

The GPCR signaling regulates many essential cell functions and comprises several signal am-

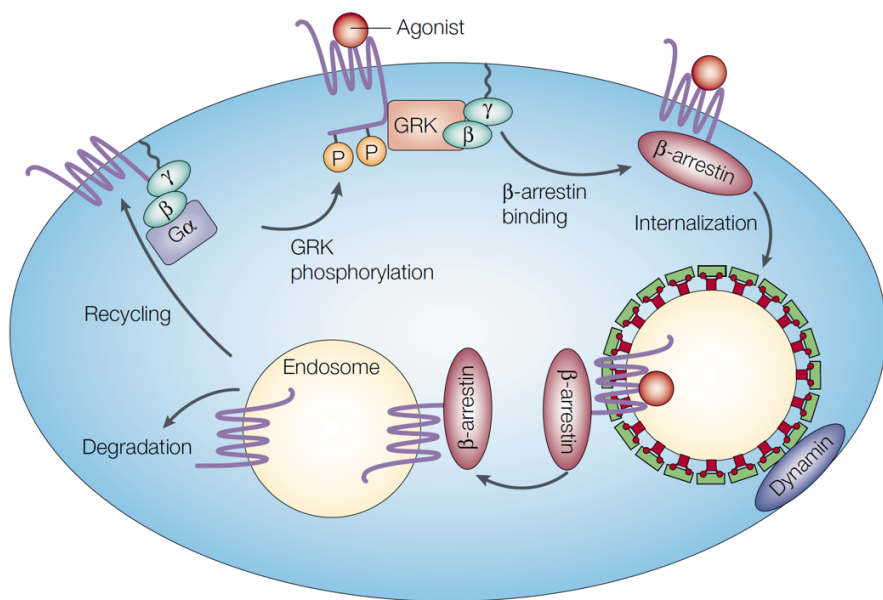


Figure 3.2.: Mechanisms of receptor trafficking.

The activated GPCR can get phosphorylated by GRKs and thus bind β -arrestin. This may lead to further interactions with endocytosis-inducing proteins and receptor internalization. The endosomal GPCR is then either recycled to the membrane or degraded.

Adapted from: "Seven-transmembrane receptors" by [1]

plifying mechanisms. Therefore, it needs to be tightly regulated and fine-tuned. This involves several distinct feed-back mechanisms with very different modes of action. One of those essential mechanisms is the GRK- β -arrestin system. A brief overview of this is outlined in figure 3.2.

The ligand binding to the GPCR and its subsequent conformational change make it susceptible for phosphorylation by the GRK. This mechanism thus selectively regulates the amount of activated GPCRs in the membrane. This process is again the target of other feedback-mechanisms as, for example, the Protein Kinase A can phosphorylate the GRK, promoting its interaction with the $G\beta\gamma$ -heterodimer and thereby increasing the phosphorylation activity of the GRK. This example shows the complexity of the interwoven regulatory mechanisms [1].

The receptor phosphorylation in turn promotes β -arrestin binding. The patterns of this phosphorylation can differ from receptor to receptor, as different GRKs preferably phosphorylate specific C-terminal GPCR sites. This 'barcode' in turn influences what kind of β -arrestin mediated function is invoked by influencing the β -arrestin conformation upon binding [23]. The bound β -arrestin desensitizes the GPCR to its external stimulus by steric hindrance of the G protein binding and thus interrupting the signaling pathway at that point [24]. At the same time it can serve as scaffold protein for steps further downstream in the signaling cascade like Raf-MEK-ERK. The GPCR-bound β -arrestin can also bind clathrin and the adaptor-related protein complex 2 (AP2). This leads to internalization of the receptor, followed either by fast or slow recycling of the deactivated receptor to the membrane (resensitization) or to its degradation (figure 3.2)[1], [24]).

3.3. Linking the receptor diffusion behaviour to its activation status

Based on the steps highlighted in the previous section, the question is now, how these mechanisms unfold at high spatial and temporal resolution on the plasma membrane, impacting the biophysical properties and thus the diffusion behaviour of the receptor.

The obvious first candidate to influence the diffusion behaviour of the receptor is the binding of the hetero-trimeric G protein. Models describing the mode of this interaction back in the 1980s suggested a collision coupling model [25], [26] which assumes a fluid mosaic model of the plasma membrane. This describes the lipid bilayer as a two dimensional plane where the embedded proteins diffuse and collide randomly[27]. This oversimplification was already questioned in the 1990s [28] and is now known to be an imprecise model. Instead, the plasma membrane was found to be a more complex and inhomogeneous system than accounted for in the classic fluid mosaic model. It instead encompasses elements like planar lipid rafts and caveolae which are both areas of GPCR clustering [29],[30]. The size of these individual membrane micro-domains may vary between few nanometres to several micrometers [31] and is highly dependant on the individual lipid composition [32]. The lipid rafts are highly dynamic structures as they can merge, split or form anew, influenced by several parameters besides the lipid composition, including the pH, the interaction with the cytoskeleton or membrane proteins [33]. This compartmentalisation of the membrane is one of the key aspects to explain the highly specific cellular responses upon signaling due to specific combinations of effector and regulatory proteins co-localizing in 'signalosomes'[34]. The same logic applies to the downstream second-messengers like cAMP. For those, a confinement due to cAMP-degrading phosphodiesterases has been proposed [35]. This organization of the GPCR signaling can be expected to have a two-fold effect on the diffusive behaviour of the receptor. First, the receptor should show a partly confined diffusion if organized in micro-domains. Second, the interaction with its G protein can no longer be expected to be modelled by random collisions as proposed earlier. Instead, newer research suggests, that the inactive GPCR can be already pre-coupled to its correspondent specific G protein subfamily[36], thereby enabling the fast interaction upon stimulation.

This has been documented, for example, by Yanagawa, Hiroshima, Togashi, *et al.* in "Single-molecule diffusion-based estimation of ligand effects on G protein-coupled receptors" [37]. While mainly focusing on the ligand effects on the receptor diffusion speed, they also tested for the effect of PTX on the diffusion of metabotropic glutamate receptor 3 (mGluR3) (also a $G_{i/o}$ coupler, in this case fused with a Halo-Tag). They showed three things. First, that

3.3. Linking the receptor diffusion behaviour to its activation status

the fast diffusion state of this receptor seems to be coupled to the G protein. An interesting finding in itself as the G protein in-fact makes the complex bigger / bulkier and the intuitive guess would have been a slowing of diffusion upon coupling. Second, and related to this finding, they show that adding PTX, and thus disrupting the GPCR-G protein complex formation, significantly slows the receptor. They also show, relating to their main focus, that agonists and therefore mGluR3 activation, generally resulted in a dose depended decrease of the Mean Square Displacement (MSD) while a inverse agonist showed the opposite effect.

Still, the coupling or uncoupling of the G protein is not the only step along the signaling cascade of GPCRs that may show up in a change of diffusion behaviour. The ability of the receptors to form hetero- or homo-oligomers also impacts not only the size of the diffusing specimen but also its conformation and thus its ability to interact with a different repertoire of intracellular proteins. The oligomerization is also highly influenced by the localisation within the membrane and vice versa [38]. This makes the influence of the oligomerization onto the diffusion behaviour more complex than a simple size dependent logic. There are for example cases, where the monomeric receptors showed a slower diffusion than the homo-dimer while a hetero-dimer exceeded the diffusion coefficient of both the monomeric and dimeric receptor state (study done on adenosine A₁ and A_{2A} receptors, tagged with full-length Yellow Fluorescent Protein (YFP) in [39]). The M2R has been reported to be monomeric, dimeric, trimeric or tetrameric by individual authors [40]–[42].

For larger receptor aggregates the intuitive logic of the larger complex having the smaller diffusion coefficient holds true [43]. This was for example pointed out by Cordeaux, Briddon, Alexander, *et al.* who showed that larger molecule species diffuse slower through the FCS confocal volume [44]. Examples for such complexes might be caveola or the clathrin coated pits. The clathrin coated pits are formed upon the β-arrestin induced internalization process of the receptor as explained in the previous chapter. The time course of this internalisation process varies between different receptor/β-arrestin combinations but reaches its minimum of receptors in the membrane after five to thirty minutes after stimulation [45]–[48]. This internalization process can also be observed for the M2R as shown in figure 3.3 adapted from [49]. The M2R was stimulated with 10 μM carbachol and imaged 30 and 90 min after stimulation. The M2R underwent translocation from the plasma membrane to distinct endosomes and small vesicles as indicated by the arrows.

All in all, the diffusion behaviour analysis can provide an insight into GPCR signaling in a very different way than classic receptor activation assays do. Thus, the insights gained with the different methods can complement each other to yield a clear picture of the real processes in the cell membrane.

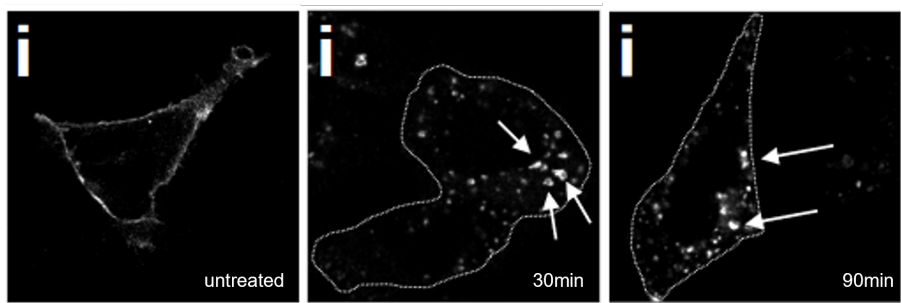


Figure 3.3.: M2R Internalization upon stimulation with 10 μ M Carbachol. The arrows indicate examples of endosomes. They used a Flag-tagged M2R with a fluorescent M1 anti-flag antibody for the labeling. Figure adapted from [49].

3.4. The incorporation of a ncAA and bio-orthogonal labeling

Most of the diffusion behaviour studies cited in the previous section utilized the addition of quite big fluorescent tags to the receptor. As mentioned before, adding an EGFP to a M2R means for example a considerable change in mass as the native receptor is around 50 kDa while the EGFP features a mass of about 27 kDa [13]. Therefore, doing so does not mean inserting a silent tagging tool into the receptor, but instead altering the receptor properties to a non-native structure that may behave differently than the unaltered native version. Examples of this may be found in [10], were a tagged EGFP slowed the receptor diffusion in a position and receptor specific manner or in [9], were they pointed out, that the addition of EGFP can abolish the receptors signaling capacities depending on the positioning.

One alternative to the addition of bulky fluorescent proteins is the incorporation of a non-canonical amino acid and subsequent bioorthogonal labeling which will add only about 1 kDa to the receptor of interest [11], [12]. This approach allows for a stable labeling of the receptor in a minimal invasive fashion as pointed out in [50] and [10] and is described in more detail in this section.

The set of natural occurring amino acids is limited to twenty amino acids and evolutionary optimized to contain stable side-chains (under biological conditions) while still enabling specific catalytic interactions when needed. This small set is naturally extended by post-translational modifications but can also be synthetically expanded by incorporating ncAA into proteins as has been shown already in 1956 by Munier and Cohen ([51]). Since then, the idea has grown to a wide field of diverse methods, enabling scientists to, for example, engineer the properties of enzymes in a precisely targeted manner or solve protein structures by X-ray crystallography [52].

There are generally two main approaches for the incorporation of ncAA in in-vivo systems. Either by residue-specific incorporation of ncAA instead of the natural variants using auxotrophic

3.5. Microscopy

strains, or by site-specific incorporation via genetic modification [52][53]. The later approach was used for this thesis and is therefore described in more detail in the following paragraphs. By mutating the amino acid position of interest to an amber stop codon (UAG), one forces the otherwise unchanged mammalian cell, to stop the protein synthesis at this point. To now instead have it incorporate the ncAA at this position, one needs to add a tRNA/amino-acyl-tRNA-synthetase pair that recognizes this stop-codon as coding for the ncAA. As this incorporation must be independent of the naturally occurring tRNA/amino-acyl-tRNA-synthetase pairs of the used cells (no cross-talk allowed), it is classified as bio-orthogonal system[54]. The systems used for mammalian cell culture are mostly derived from an archaeal pair that naturally incorporates pyrrolysine (Pyl) in *Methanosarcina* species (PylRS/tRNA^{Pyl}). The here used system, MbPylRS^{AF}/tRNA^{M15}, has been optimized by Serfling, Lorenz, Etzel, *et al.* for the usage in mammalian cells ([55]). This was achieved by enhancing the compatibility of the tRNA with the mammalian system due to rationally designed mutations of the tRNA, thus, increasing its intracellular concentration 2-5 fold compared to the non-optimized version in the same expression cassettes.

The ncAA that is to be incorporated can be added to the medium and is subsequently taken up by the cell. Using trans-Cyclooct-2-en-L-Lysine (TCO*A) for in-vivo experiments has the substantial advantage that it is a suitable reaction-partner for a catalyst-free, fast, specific, and bioorthogonal strain-promoted inverse electron-demand Diels-Alder cycloaddition (SPIEDAC) reaction with tetrazine. Bio-orthogonality here again implies, that neither the TCO*A nor the tetrazine show unwanted cross-reactions in the cell while the SPIEDAC reaction takes place under cell-physiological conditions [54]. As several fluorophore-tetrazine combinations are available, this opens a range of possibilities for individual staining [56].

3.5. Microscopy

Fluorescence microscopy has branched into a wide selection of techniques that each offer a individual set of advantages and disadvantages [57]. While a basic bright field microscope may be found in most laboratories, more specialised microscopes are rarer.

Four different kinds of microscopes were used for this thesis. A bright field epifluorescence microscope for cell culture monitoring, an inverted, dual channel epifluorescence microscope for the receptor functionality assay, a confocal microscope for the main work on LS imaging and subsequently a total internal reflection fluorescence (TIRF) microscope for the single molecule tracking. A short introduction to the last two more complex techniques is given in the following sections.

3.5.1. TIRF microscopy and SMT

TIRF microscopy uses a special illumination technique that generates an evanescent field at the cell membrane/glass interface and thus selectively illuminates a thin sample layer ($< 200\text{ nm}$ depth). This is achieved by setting the laser to a 'critical angle' relative to the cover slip so that the light does not get refracted any more but instead gets internally reflected in the coverslip and an exponentially decaying evanescent wave is generated at the interface [58][59]. This technique allows the user to selectively illuminate the basal plasma membrane and thus monitor the dynamics of labelled membrane proteins with reduced background fluorescence when compared to wide-field techniques. Given a suitably low receptor number, each receptor can be followed individually (single molecule/particle tracking SMT). Thus, it is possible to extract a plethora of data like the MSD curves and individual tracks but also co-localization times. A graphical overview is given in figure 3.4(a)(from "Single molecule techniques for the study of membrane proteins", García-Sáez and Schwille[60]). The time-lapse series is acquired in short time intervals (in the experiments done in this thesis one picture about every 30 ms) and the time-stack subsequently used for particle detection via two dimensional Gaussian fitting (e.g. with MatLab 'uTrack') [61]. Subsequently the peak positions are followed through the time stack and thus the individual tracks extracted. These tracks can subsequently be used to calculate the MSD as further introduced in section 3.6.2. That in turn gives insight into the diffusion properties. The examples shown here are (A) normal diffusion and thus a linear MSD curve and (B) a confined diffusion indicated by a plateauing MSD curve.

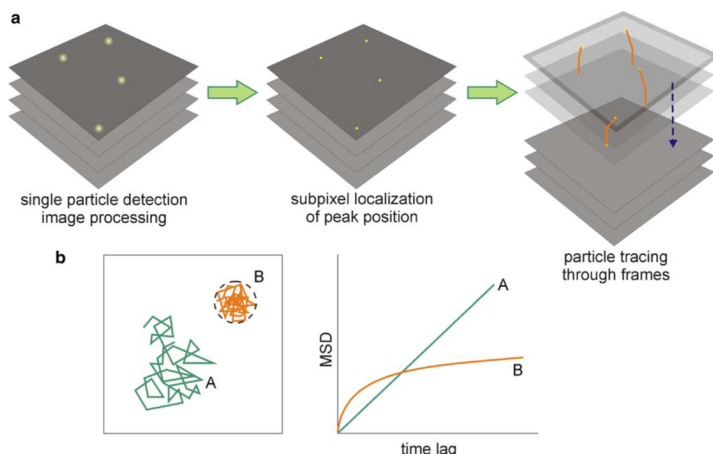


Figure 3.4.: Overview of the SMT principles. The time-lapse series is acquired and the signal peaks localized via Gaussian fitting. Subsequently these peak positions can be followed over time, resulting in individual molecule tracks. These can be used for MSD calculation and diffusion analysis. Picture taken from "Single molecule techniques for the study of membrane proteins", García-Sáez and Schwille[60]

3.5.2. Confocal microscopy

A laser scanning confocal microscope (LSCM) has the specific characteristic that it focuses the illumination and detection optics on the very same diffraction limited point in the sample

(confocal = having the same focus)[62]. It thereby avoids the blur by out-of focused fluorescence signal. Such a blur may be seen for example in the inverted fluorescence microscope mentioned above when out-of focus specimen get excited and contribute to the detected signal. On the other hand, the single-spot detection technique, as it is applied by the confocal microscope, makes it necessary to move the excitation volume point-by-point (raster-scanning) in order to collect the whole image. It thus builds the picture from a mosaic of individually detected spots.

In case of the LS acquisitions conducted in this thesis, always the same line is imaged again and again instead of moving over the sample in two dimensions. This allows small time intervals in-between measurements of the same spot. For the setting used in this thesis (1800 Hz) each spot/pixel (with a diameter of 50 nm) was observed approximately every 0.5 ms. The small imaging interval combined with a precise photon-counting detector makes this a valuable tool for FCS which is further explained in the next section 3.6.

3.6. Analyzing the membrane receptor behaviour with Fluorescence correlation spectroscopy (FCS)

3.6.1. FCS compared to other common methods

There are several biophysical techniques available to investigate the molecular mobility and diffusion behaviour of fluorescent particles in a membrane. Three widely known examples are fluorescence recovery after photobleaching (FRAP), SMT and FCS. All of them have different advantages and disadvantages depending on the intended application [63].

FRAP uses the selective destruction of fluorescent molecules in the region of interest and subsequently monitors the recovery of fluorescence due to new fluorescent molecules diffusing into the observed region. This technique is especially suitable for high fluorophore concentrations which are in turn not useable for FCS or SMT. FRAP is on the one hand limited in the achievable resolution (μm spatial scale and seconds in the temporal scale). On the other hand, it also offers information about the immobile fraction of the investigated fluorophores.

SMT follows the individual paths of single particles, thereby extracting the individual trajectories and MSDs. In order to follow those particles individually, the fluorophore concentrations must be quite low. As less and less particles can be followed with growing time intervals, the uncertainty in the MSD extraction increases with higher τ -values. An advantage of this technique is that the variety of different diffusion modes can be directly observed in the individual trajectories.

FCS detects the intensity fluctuations of individual confocal areas induced by fluorophores passing through. While this does not offer individual trajectories, it offers information about the diffusion processes that can be extracted via spatio-temporal correlation in a high temporal resolution (ms to seconds). It is furthermore applicable for a fairly wide range of concentrations

even though the precision decreases with the shrinking fluctuation amplitude for increasing particle densities. It is furthermore very versatile in its applications. It is possible to use FCS to analyse binding or interaction kinetics, to name only two examples. [64][60]

The focus of this thesis lays on the diffusion analysis (diffusion coefficient, - mode and confinement analysis) with FCS in a high temporal resolution. The basic principles needed for this analysis are therefore explained in the following sections.

3.6.2. Diffusion and the Mean Square Displacement (MSD)

Diffusion, thus the movement of particles, can have quite different modes of action. In the simplest case it is purely Brownian motion, which means a random movement of particles influenced only by thermal fluctuations. In case of receptors in a membrane, the situation is more complex due to a generally highly crowded environment paired with diverse interactions as pointed out above. One of the main tools to analyse the diffusion behaviour is the measurement of the Mean Square Displacement (MSD). It describes the mean deviation of the position of an observed object after a given time interval τ when compared to its position at $\tau = 0$. For a two dimensional system this is shown in figure 3.5 which is taken from "SPT and Imaging FCS Provide Complementary Information on the Dynamics of Plasma Membrane Molecules" by Harwardt, Dietz, Heilemann, et al.[65].

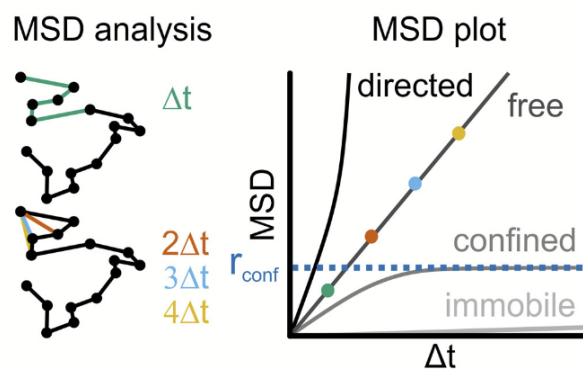


Figure 3.5.: An exemplary particle track with individual colour coded time-steps taken for MSD calculation. The resultant MSD curve of a free diffusion is depicted in the graph on the right, together with prototypical curves for directed/ super-diffusion and confined/sub-diffusion. The picture is taken from "SPT and Imaging FCS Provide Complementary Information on the Dynamics of Plasma Membrane Molecules" by Harwardt, Dietz, Heilemann, et al.[65]

On the left hand it shows an exemplary single particle track in a two dimensional plane. The dots indicate the particle positions for every (equally spaced) measurement time-point. The smallest τ of the analysis and thus the time resolution of the MSD depends on the acquisition time and is purely the mean squared distance between the consecutive dots/positions delineated in green. This results in the first data-point of the MSD-curve. This logic is subsequently extended to bigger τ -values. Thus, the next step is to take the mean squared distance

3.6. Analyzing the membrane receptor behaviour with Fluorescence correlation spectroscopy (FCS)

between every second dot (orange) and plot this against two times the acquisition interval and so forth. By doing so, the analysis yields a MSD-plot like the one on the right hand side of figure 3.5. The different MSD values delineated over the corresponding Δt or τ -values are again colour coded. If the observed particle behaves in a unobstructed, non-influenced mode, it shows normal/free diffusion and thus a linear MSD growth over time. In this case, the diffusion constant D can be derived by linear fitting and using the slope $\frac{\Delta \text{MSD}}{\Delta \tau}$.

$$\frac{\Delta \text{MSD}}{\Delta \tau} = 2nD \quad (3.1)$$

The n stands for the dimensions in which the observed particle is moving. For a membrane diffusion, this would be considered to be two while a diffusing dye in the cytoplasm would have three dimensions to move around in[16]. This slope - D relation is shown in figure 3.6 (B). Also the apparent particle size can be deduced from the MSD curve as the squared apparent particle size corresponds to the y-intercept of the MSD curve. If the Point Spread Function (PSF) is known, one could also calculate the actual particle size as shown in 3.6 (A).

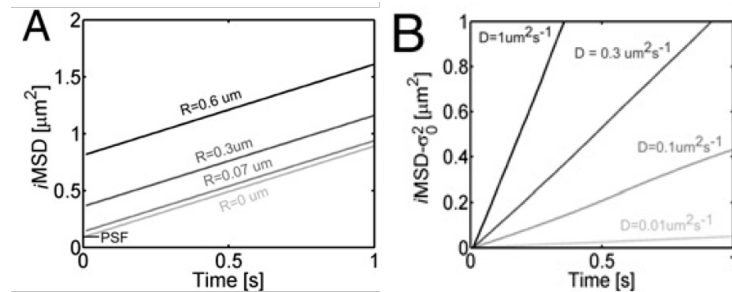


Figure 3.6.: Examples for MSD-plot readouts. (A) illustrates the connection between y-intercept and particle size and (B) depicts the relation between MSD-curve slope and the diffusion coefficient. The picture is adapted from “Fast spatiotemporal correlation spectroscopy to determine protein lateral diffusion laws in live cell membranes” by Di Rienzo, Gratton, Beltram, et al.[16]

3.6.3. Autocorrelation

The basic procedure of all LS-FCS experiments is the repeated acquisition of one particular line in the field of view in defined time intervals. Taking a step back to understand the concepts at work within these experiments, one can also describe this kind of data-set more general as discrete time series, containing observations made at different, successive time points [66].

The autocorrelation function defines how the data-points in a time series are related (on average) to their preceding data points[66], [67]. Or, in other words, the autocorrelation function describes how well the signal correlates to shifted versions of itself [68]. For a time (t) series and the time delay τ , the autocorrelation of the signal x is defined as [68], [69]:

$$r_{(xx)}(\tau) = \frac{1}{T} \int_0^T x(t)x(t + \tau)dt \quad (3.2)$$

Figure 3.7, adapted from [68], shows exemplary autocorrelation plots (right side) and their correspondent signal plots (left side). On the left side are the signal intensities plotted (y-axis), that vary over the time (x-axis). An example could be the fluorescence intensity in a single point of a LS varying over the time (with the difference that the plotted example is a continuous signal). The autocorrelation (right plots) in this example is normalized to its variance and varies therefore between one and zero. As it is a measure of similarity, the autocorrelation of a signal at a time delay zero (not shifted) must be one.

Thus, the signal is identical with itself. For a completely random signal (A), the autocorrelation for any other time delay but zero immediately drops to zero autocorrelation (no correlation between the individual data-points). For a slowly changing signal as shown in (B), the autocorrelation drops slowly over increasing time lags. Thus, the signal decorrelates way slower in (B) than in (A).

This principle of autocorrelation is adapted, as outlined in the next section, to measure the intensity fluctuations evident in the individual LS.

3.6.4. The correlation of fluctuations and the spatiotemporal image correlation spectroscopy (STICS) function

As explained before, the line scanning, as performed in the FCS experiments in this thesis, does not yield individual receptor tracks but instead the signal intensity fluctuations of individual pixels over time. In order to connect these to the actual diffusion happening in the sample, one needs to correlate those fluctuations [70].

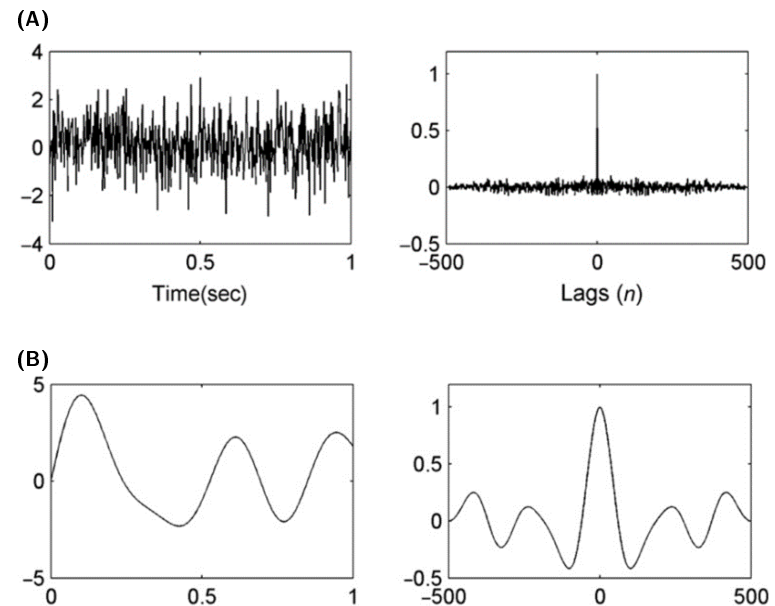


Figure 3.7.: Exemplary autocorrelation curves (right side) of two different signals (left side). (A) for a random signal, (B) for a slowly changing signal. Adapted from “Basic Concepts in Signal Processing” [68]

3.6. Analyzing the membrane receptor behaviour with Fluorescence correlation spectroscopy (FCS)

The generalized spatio-temporal intensity fluctuation correlation function [16][70] is given in equation 3.3 that applies to a two dimensional space (x,y) acquired over the time t.

$$G(\xi, \chi, \tau) = \frac{\langle I(x, y, t) \cdot I(x + \xi, y + \chi, t + \tau) \rangle}{\langle I(x, y, t) \rangle^2} \quad (3.3)$$

This equation was modified for the use on line scans as they are only one pixel wide in y direction and thus can not be correlated in this dimension. The resulting simplified version is given in equation 3.4.

$$G(\xi, \tau) = \frac{\langle I(x, t) \cdot I(x + \xi, t + \tau) \rangle}{\langle I(x, t) \rangle^2} \quad (3.4)$$

Here, ξ stands for the distance between the correlated pixels along the line (spacial distance), while τ is the time lag between the correlated pixels. The $\langle \rangle$ imply averaging over time and space. [16]. It is thus basically a way to calculate the similarity of the signal to it self over time and space as explained in more detail in section 3.6.3. As this calculation is computationally inefficient, the alternative is to harvest the connection between the autocorrelation (AC) to the power spectral density (PSD) of the signal as they are Fourier-transform pairs. Fourier transformations are a classic tool in signal processing and their computationally calculation was considerable sped up with the development of the fast Fourier transform (FFT) algorithms in the 1960s. This method is by now highly optimized and a widely implemented tool [71][72]. The Fourier transform of the LS (*FTLS*) is calculated by a fast Fourier Transform over both dimensions, thus here denoted as *2DFFT*[73]. The PSD of the LS can now be calculated by multiplying the *FTLS* with its complex conjugate \overline{FTLS} . As the PSD and the autocorrelation are Fourier pairs, one can get the STICS function by calculation the inverse Fourier transform (inverse two dimensional fast Fourier = *2DIFTT*) of the PSD as summarized in equation 3.6 [74].

$$FTLS = 2DFFT(LS) \quad (3.5)$$

$$STIC = 2DIFTT(FTLS \cdot \overline{FTLS}) \quad (3.6)$$

Now there are different ways to yield insight into the diffusion behaviour from the STICS matrix. One is, to fit diffusion models to the autocorrelation function (STICS function at position $x=0$). Standard diffusion models for two dimensional diffusion (e.g. membrane diffusion) and three dimensional diffusion (e.g. cytoplasm) are given in equation 3.7 for the 3D case and in equation 3.8 for the 2D case [15].

$$G(x = 0, \tau) = G(0) \cdot \frac{1}{(1 + \frac{4D\tau}{\omega_0^2}) \cdot \sqrt{1 + \frac{4D\tau}{\omega_z^2}}} \quad (3.7)$$

$$G(x = 0, \tau) = G(0) \cdot \frac{1}{(1 + \frac{4D\tau}{\omega_0^2})} \quad (3.8)$$

The used wavelength of the acquisition must be known to use these models, as they take the PSF in the xy plane ω_0 and the beam waist ω_z as model parameters. The models allow a direct readout of the diffusion coefficient D as it also is a model parameter.

A different way to approach the readout of the diffusive behaviour from the STICS function is to use its Gaussian nature. Figure 3.8 [16] shows a visualization of the workflow from the data acquisition to the MSD extraction by Gaussian fitting. In this example a xy-plane is acquired (A) and from here the STICS matrix is calculated (B). Its dimensions correspond to those of the acquisition (taking the time dimension in on the count). The STICS function of a typical LS is therefore here included as the slice at $x = 0$, therefore no variation in that direction. (C) shows the same STICS in individual τ -slices as 3D plot and thus visualizes their Gaussian shape. Fitting those to a classic Gaussian function as it is given in equation 3.9 for the 2D case of line scans, allows the read-out of the model parameters, among them the variance σ . The variable A corresponds to the amplitude and μ to the centre-position of the Gaussian fit [75].

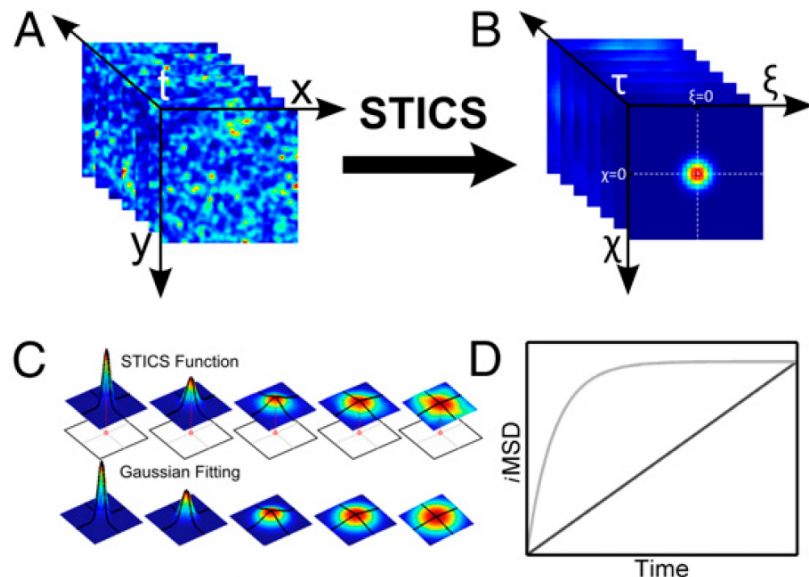


Figure 3.8.: Workflow illustration from the acquisition of the FCS data to the generation of the MSD curves. (A) shows a exemplary xy-plane acquisition stack, (B) a stack of corresponding STICS plots that are shown again in 3D in (C) together with the Gaussian fits. (D) shows an exemplary MSD-plot generated from the Gaussian fitting. Figure from “Fast spatiotemporal correlation spectroscopy to determine protein lateral diffusion laws in live cell membranes” by Di Rienzo, Gratton, Beltram, et al.[16]

$$f(x) = \frac{A}{\sigma\sqrt{2\pi}} \cdot e^{[\frac{-(x-\mu)^2}{2\sigma^2}]} \quad (3.9)$$

As the MSD equals the denominator of the exponent of the Gaussian fit [16], the MSD value for every τ -value can thus be extracted by applying equation 3.10, yielding a MSD-plot as discussed in section 3.6.2 with all its possible read-outs.

$$MSD(\tau) = 2\sigma^2 \quad (3.10)$$

3.7. Python

The Python programming language, first introduced in the 1990s, was designed to be open-source [76] and easily readable in its syntax but still powerful in its application possibilities as it is a multi-paradigm language [77]. The goal of its original creator Guido van Rossum was to design a tool that makes 'Computer Programming for Everybody' possible [78]. Python allows straight forward object-orientated programming with built-in high-level data types. It is supported by a huge library of additional modules for scientific computing, e.g. NumPy [79]. There are currently three main Python versions. Python 2 introduced some major features like a cycle-detecting garbage collector (simplifying memory management) but still maintained backwards-compatibility. However, Python 3 is no longer backwards-compatible as many redundant ways to do the same thing (which accumulated over the previous versions) were removed [80]. The newest version, Python 3.9 was used for this thesis.

4. Materials and Methods

4.1. Materials

This section provides an overview of the material needed for all methods deployed during the research for this thesis. A comprehensive method description can be found in section 4.2.

Table 4.1.: cell cultivation

Cell Culture		
Dulbecco's Phosphate Buffered Saline	D8537-500ML	Sigma-Aldrich Chemie GmbH
DMEM	P04-03600	PAN Biotech GmbH
L-Glutamine	PD4-BOD50	PAN Biotech GmbH
Trypsin/EDTA	P10-023100	PAN Biotech GmbH
Penicillin Streptomycin	15140-122	Gibco™ Thermo Fisher Scientific
FBS SUPERIOR	S0615	Sigma-Aldrich Chemie GmbH
DMEM/F-12	21041-025	Gibco™ Thermo Fisher Scientific
poly-D-lysine hydrobromide	P0899-100MG	Sigma-Aldrich Chemie GmbH
FluoroBrite™ DMEM	A18967-01	Gibco™ Thermo Fisher Scientific

Table 4.2.: All used cell lines

Cell Lines		
293AD cell line	AD-100-GVO-CB	BioCat GmbH
CHO-K1	CCL-61	ATCC®
tsa201 Cell Line human	96121229-1VL	2021 Merck KGaA

4.1. Materials

Table 4.3.: Enzyme-linked Immunosorbent Assay for HA-detection

ELISA			
Dulbecco's Phosphate Buffered Saline	D8537-500ML	Sigma-Aldrich Chemie GmbH	
DMEM	P04-03600	PAN Biotech GmbH	
Citric acid monohydrate (99%)	C1909-1KG	Sigma-Aldrich Chemie GmbH	
Sodium phosphate 96%	342483-500G	Sigma-Aldrich Chemie GmbH	
Hydrogen peroxide	21,676-3	Sigma-Aldrich Chemie GmbH	
Sulfuric acid 96%	4623.3	Carl Roth GmbH + Co. KG	
Anti-HA-Peroxidase High Affinity (3F10)	12013819991	Merck KGaA	
HEPES buffered saline	51558-50ML	Sigma-Aldrich Chemie GmbH	
o-Phenylenediamine Dihydrochloride	615-28-1	Thermo Fisher Scientific	
Paraformaldehyde solution 4% in PBS	sc-281692	Santa Cruz Biotechnology Inc.	

Table 4.4.: Transfection

Transfection			
TCO* storage buffer	selfmade	0.2 M NaOH, 15% (vol/vol) DMSO	
trans-Cyclooct-2-en – L - Lysine (TCO*A)	SC-8008	SiChem GmbH	
Opti-MEM®	11058-021	Gibco™ Thermo Fisher Scientific	
Lipofectamine® 2000	11668-019	Invitrogen™ Thermo Fisher Scientific	

Table 4.5.: Agarose gel electrophoresis

Agarose-Gel Electrophoresis			
Ethidium Bromid	15585-011	Invitrogen™	Thermo Fisher Scientific
UltraPure™Agarose	16500-500	Invitrogen™	Thermo Fisher Scientific

Table 4.6.: Transformation for plasmid production

Transformation			
SOC Outgrowth Medium	B9020S	New England BioLabs™Inc.	
5-alpha competent E.coli	C2987H	New England BioLabs™Inc.	
LB-Medium	X968.2	Carl Roth GmbH + Co. KG	
Agar Bacteriology grade	9002-18-0	AppliChem GmbH	
Kanamycin sulfate 750 I.U./mg	T823.2	Carl Roth GmbH + Co. KG	
Ampicillin sodium salt	K029.1	Carl Roth GmbH + Co. KG	

Table 4.7.: Polymerase Chain reaction reagents for site-directed mutagenesis and cloning

PCR and Cloning		
dNTP Mix	R0192	Thermo Fisher Scientific
DMSO	#B0515A	New England BioLabs® Inc.
Q5® High Fidelity DNA Polymerase	M0491L	New England BioLabs® Inc.
Q5® High GC-Enhancer	B9028A	New England BioLabs® Inc.
Q5® Reaction Buffer	B9027S	New England BioLabs® Inc.
NEBuilder® HiFi DNA Assembly Master Mix	E2621L	New England BioLabs® Inc.
DpnI	R0176L	New England BioLabs® Inc.

Table 4.8.: Primers and plasmids

Primers (5'-3') and Plasmids		
Backbone	Banana split rev	TTGATGAGTTGGACAAACCACAACTAGAAT
	Banana split fwd	ATTCTAGTTGTGGTTGTCCAAACTCATCAA
EGFP-out	P154	ATAGGCGCTACAAGGTAAGCGGCCGCTCGAG
	P155	AGGGGCGATGATCGTCTTCATCAGTGTGATGGATATCTG
	P156	ATGCTCGAGCGGCCGCTTACCTTGATCGCCTAT
	P157	CAGATATCCATCACACTGATGAAGACGATCATGCC
M2R-Mut8	Mut8-F	ACAAACTCCTAGAACAAATAGCC
	Mut8-R	TGAGTTATTCCATCCTTGTAG
Plasmids		pcDNA3.1-SigPep-HA-M2AR-EGFP
		pcDNA3.1-SigPep-HA-M2AR
		pcDNA3.1-SigPep-HA-M2ARMut8-EGFP
		pcDNA3.1-SigPep-HA-M2ARMut8

Table 4.9.: DNA extraction kits

DNA Extraction Kits		
Monarch® Plasmid Miniprep Kit	T1010L	New England BioLabs® Inc.
Monarch® DNA Gel Extraction Kit	T1020L	New England BioLabs® Inc.
Plasmid Plus Midi Kit	12945	Qiagen®

4.1. Materials

Table 4.10.: General technical instruments

General technical Instruments	
Vortex-Genie 2	Scientific Industries, Inc.
Cubis®	Satorius AG
Azure c200	Azure Biosystems, Inc.
PowerPac™Basic Power Supply	Bio-Rad Laboratories, Inc.
Synergy Neo2 Hybrid Multi-Mode Reader	BioTek Instruments, Inc.
Biometra TRIO	Analytic Jena GmbH
arium®pro	Satorius AG
Centrifuge 5424	Eppendorf AG
Centrifuge 5424 R	Eppendorf AG
Eppendorf Research® plus (different sizes)	Eppendorf AG
Eppendorf Xplorer® (different sizes)	Eppendorf AG
Eppendorf ThermoMixer® C	Eppendorf AG
Spectrophotometer DS-11 FX +	DeNovix Inc.
New Brunswick™Galaxy® 48 R	Eppendorf AG
Climo-Shaker ISF1-XC	Adolf Kühner AG
Hermatherm IGS60	Thermo Fisher Scientific
Allegra X-15 R	Beckman Coulter®
DS-11FX+Spectrophoto-/Fluorometer	DeNovix Inc.
Incubator 9140-0039	Nikon (Prafektur Tokio, JPN)
Nikon ECLIPSE Ti2 microscope	DeNovix Inc.

Table 4.11.: Software

Software	
LAS X Life Science	Leica Microsystems GmbH (Wetzlar, GER)
MATLAB	The MathWorks, Inc. (Massachusetts, USA)
NIS-Elements AR	Nikon (Prafektur Tokio, JPN)
Prism7	GraphPad Software (La Jolla, USA)
SnapGene	GSL Biotech LLC (Illinois, USA)
Python 3.9	Python Software Foundation
PyCharm	JetBrains

Table 4.12.: Confocal microscopy setup

Confocal microscope	
Confocal Sp8 (two HyD detectors and WLL laser)	Leica Microsystems
LAS X microscope control software	Leica Microsystems
40x/1.10 water immersion objective	Leica Microsystems
H301-EC-BL Incubation Chamber	OKOLAB
OKO-Touch	OKOLAB

Table 4.13.: Brightfield fluorescence microscopy setup

Brightfield fluorescence microscope (Visitron)	
Leica DMi8 inverted microscope	Leica Microsystems
HC PL APO 40x/1.4-0.60 oil	Leica Microsystems
Dichroic beamsplitter T505lpxr	Visitron Systems
Visichrome high-speed polychromator	Visitron Systems
Xe-Lamp 75 W, 5.7 A	Hamamatsu Photonics
Photometrics Prime 95B CMOS camera	Visitron Systems
Optosplit II dual emission image splitter	Cairn
Visiview 4.0 imaging software	Visitron Systems

4.2. Methods

4.2.1. Cell culture

All cell lines were grown in T75 flasks (SARSTEDT) at 37 °C and 5% CO₂. The 293AD cell line (BioCat) and the tsa201 cell line (Merck) were cultured in Dulbecco's modified Eagle's medium (DMEM) (PAN Biotech) supplemented with 10% (vol/vol) Fetal bovine serum (FBS) (Sigma Aldrich), 1% L-glutamine (PAN Biotech), penicillin (100 U/mL), and streptomycin (100 µg/mL) (Gibco). The CHO-K1 cell line (ATCC) was cultured in phenol red-free DMEM/F12 (Gibco) with the same supplements as mentioned above. The used components are listed in table 4.1.

The cell lines were used in passages five to 20. To passage cells, the medium was aspirated, the cells were washed by adding Phosphate-buffered saline (PBS) (Sigma-Aldrich), followed by treatment with 2,5 mL Trypsin/Ethylenediaminetetraacetic Acid (EDTA) (PAN Biotech) for 0,5 to 1,5 min depending on the cell line. After removing the Trypsin/EDTA, the cells were resuspended in 10 mL medium. They were either split 1:10 for further cultivation or counted with 0.4% Trypan Blue in a Neubauer chamber to be used in experiments.

4.2.2. Transfection

Depending on the planned experiments, cells were plated in a 6-well plate (10⁵ to 10⁶ cells /well) or in an IBIDI slide (5·10⁴ cells/well). In case of microscopy experiments, the cover slips were coated with 125µg/mL poly-D-lysine hydro-bromide (Sigma-Aldrich Chemie GmbH), let sit for 30 min, and then thoroughly washed with PBS for three times before plating the cells. After letting the cells adhere for at least 6h or overnight, the medium was changed to medium without any supplements. For transfections with bio-orthogonally labelled receptors, 0.25mM f.c. TCO*A (SiChem GmbH) was added 1 - 2 h before transfection by first preparing a 100 mM TCO*A - stock using TCO* storage buffer (0.2 M NaOH, 15% (vol/vol) Dimethylsulfoxid (DMSO)) and premixing the needed volume 1:4 with HEPES buffered saline (Sigma-Aldrich Chemie GmbH) before adding the mixture into the medium. The transfections were performed with Lipofectamine®2000 (Invitrogen™Thermo Fisher Scientific). Two separate tubes were prepared. One to dilute the DNA in Opti-MEM®(Gibco™Thermo Fisher Scientific) and the second tube for dilution of Lipofectamine®2000. After 5min incubation at RT, both tubes were combined and gently mixed. After an additional 20 min at RT, the mixture is carefully, drop-wise added to the cells. The Amber-mutated receptor was co-transfected (1:1) with the plasmid that carries the bioorthogonal system for incorporation of the ncAA (MbPyl- SAF/4xtRNAM15). The needed volumes depend on the chosen plates and are given for 6-well plate and 8-well IBIDIs (per well) in table 4.14 The medium was changed to standard cell culture medium 4h after transfection.

Table 4.14.: Transfection (per well)

	Lipofectamin Pre-mix		DNA Pre-mix	
	<i>Opti-MEM®</i> [µL]	<i>Lipofectamine® 2000</i> [µL]	<i>Opti-MEM®</i> [µL]	DNA [µg]
8-well IBIDI	25	0.6	25	0.6
6-well plate	150	3.75	150	1.5

4.2.3. Construction of the M2 receptor variants

All variants of the M2R used in this thesis were generated by utilizing Gibson assembly [81] (to add fluorescent tags) and Site-directed mutagenesis (to introduce the Amber-mutation at position 8). The freshly cloned plasmids were synthesized via *E.Coli* transformation with subsequent Miniprep and send away for sequencing (LGC Genomics GmbH). The correctness of the resulting sequence was verified by in-silico Gibson Assembly in SnapGene and subsequent BlastN analysis. Thereafter, the correct plasmids were multiplied by Midipreps. All herein shortly mentioned steps are outlined in the next few subsections. An overview of the used Plasmids and Primers for this thesis can be found in table Plasmid cards of the constructed plasmids used in the following experiments can be found in the appendix at page

4.2.4. Fragment production by Polymerase chain reaction and gel electrophoresis

All PCRs were performed with Q5® High Fidelity DNA Polymerase (New England BioLabs® Inc.) according to the product protocol. The needed pipetting steps are summarized in Table 13 and were performed on ice. The thermocycling was performed by a Biometra TRIO machine (Analytic Jena GmbH) with a heated lid. The thermocycler settings used are summarized in Table 12. The annealing temperature depends on the used primer pair and was determined with the NEB Tm Calculator (v1.13.0, New England BioLabs® Inc.). The extension time is amplicon dependent and was set to 30sek per kilobase amplicon.

The PCR products were separated by a gel electrophoresis with 1.1% agarose gel (100mL TAE, 1.1g Agarose, 8µl Ethidium-Bromide) for 30 to 45 min at 110V.

The product bands of the expected sizes were excised and purified by using the Monarch® DNA Gel Extraction Kit (New England BioLabs® Inc.). Therefore, the gel piece was dissolved in Gel Dissolving Buffer (400µL per 100mg agarose) for ca. 5min at 50°C, shaking till completely dissolved, applied on a column from the kit and spun down 1min at 16000g. After discarding the flow through and adding 200µl DNA Wash Buffer the centrifugation step was repeated. The cleaned column was transferred to a fresh 1.5mL microfuge tube and the DNA

Table 4.15.: PCR pipetting scheme

Component	Volume [μL]	Stock c.	f.c.
Plasmid DNA	1	100 ng/ μL	2 ng/ μL
Primer forward	2,5	10 μM	0.5 μM
Primer reverse	2,5	10 μM	0.5 μM
dNTPs	1	10 mM	200 μM
Q5 reaction buffer	10	5x	1x
Q5 HiFi GC Enhancer	10	5x	1x
Q5 HiFi DNA Polymerase	0,5	2 U/ μL	0.02 U/ μL
ddH ₂ O			Fill up to 50 μL

Table 4.16.: Thermocycling conditions for PCR

Step	Temperature [°C]	Time	
Initial Denaturation	98	30 s	
Denaturation	98	10 s	
Annealing	Primer dependent	30 s	
Extension	72	Amplicon dependent	$\times 30 \text{ cycles}$
Final Extension	72	2 min	
Hold	4		

eluted by adding 15 μl Nuclease-free water. After letting it sit for a minute, the DNA was collected in the microfuge tube by again centrifuging for 1min at 16000g.

The DNA concentration was determined by a spectrophotometric measurement and the fragments used for subsequent Gibson Assembly.

4.2.5. Cloning

The cloning steps were performed with the NEBuilder® HiFi DNA Assembly Master Mix from New England BioLabs® Inc. Therefore, primers with suitable overlaps were designed in SnapGenes in-silico Gibson Assembly, the PCR was performed as illustrated in the previous section and those fragments used for the cloning step.

The needed amount of each fragment was calculated according to equation 4.1

$$\text{ng} = \frac{\text{pmol} \cdot \text{bp} \cdot 650 \text{ Da}}{1000} \quad (4.1)$$

For 2-3 fragments a 1:2 (vector: insert) molarity was used while in case of more fragments the amounts were set to equal molarities. The total fragment amount was set between 0.2 to 0.5pmol in 10 μl water. The pipetting steps were performed on ice. 10 μl NEBuilder® HiFi DNA Assembly Master Mix was added to the 10 μl fragment premix and incubated in the thermocycler at 50°C for 15min. 2 μl of the resulting mix was subsequently used for transformation.

4.2.6. Site-directed Mutagenesis

The site-directed mutagenesis was used for introducing the amber-mutations. To this end, back-to-back primers were designed that encoded for the exchanged triplet and binding extensions to either side of the mutation of more than 11bp. The primers are optimized in SnapGene in terms of binding specificity and secondary structure avoidance.

With these a PCR was performed as described above. The PCR mix (50 μ l) was then treated overnight at 37°C with 20U DpnI (New England BioLabs® Inc.) and 5.6 μ l 10x CutSmart Buffer (New England BioLabs® Inc.). The enzyme is inactivated at 80°C for 20min and the mixture used for subsequent transformation and Mini-prep as described below.

4.2.7. Transformation

For transformation 50 μ L 5-alpha competent E.coli (New England BioLabs™ Inc.) were thawed on ice. The DNA was added (1-2 μ l) and the tube carefully flicked for a few times. The mix was left to incubate on ice for 30min. Then the sample was heat-shocked at 42°C for 45seconds and placed on ice for two minutes. Thereafter 200 μ l pre-warmed SOC Outgrowth Medium (New England BioLabs™ Inc.) was added, and the bacterial cells were incubated for 45min at 37°C before being spun down at 375g for 2min. The pellet was resuspended in 80 μ l SOC Outgrowth Medium and spread on a prewarmed LB-agar plate with selective antibiotic and incubated overnight at 37°C. The following day colonies are picked and cultivated in 5mL LB-Medium (Carl Roth GmbH + Co. KG) with selective antibiotic overnight. The culture was than used to perform a Mini-Prep and sequence check as described below.

4.2.8. Plasmid Miniprep

The Minipreps were performed with the Monarch® Plasmid Miniprep Kit (New England BioLabs® Inc.). An overnight bacterial culture of 1 to 5 mL was spun down at 16000g for 1min and the pellet resuspended in 200 μ l Resuspension Buffer. Then 200 μ l Plasmid Lysis Buffer was added and the tube gently inverted for a few times to mix. After incubating this Lysis step for 1min at RT 400 μ l Plasmid Neutralization Buffer was added, mixed again by inverting and incubated for 2min at RT. The neutralized sample is than centrifuged at 16000g for 5min and the supernatant transferred onto a spin column. The column was centrifuged 1min at 16000g and the flowthrough discarded. Now the column was washed by adding 200 μ l Plasmid Wash Buffer 1 and repeating the last centrifugation step. The second wash step was performed with 400 μ l Plasmid Wash Buffer 2 and again centrifugation. The column was transferred to a fresh microfuge tube and the DNA eluted by adding 30 μ l nuclease-free water. After 1min incubation at RT, the column was again spun down to collect the DNA in the

4.2. Methods

fresh tube. The sample was than sequenced (LGC Genomics GmbH). and, if resulting in the expected sequence, used for a Midiprep.

4.2.9. Plasmid Midiprep

All Midipreps were performed by using the Plasmid Plus Midi Kit (Qiagen®). 50 mL bacterial overnight culture was spun down at 4°C, 5250g for 15min. The palette was resuspended in 4 mL buffer P1. 4 mL buffer P2 were added for lysis and the sample is mixed by inverting it a few times till homogeneously viscous. Then it was left to incubate at RT for 3min and subsequently neutralized by adding 4 mL buffer S3 and again inverting to mix. The sample was transferred to a QIAfilter Cartridge and incubated 10min at RT. Thereafter it was pushed through the filter into a fresh tube and mixed with 2 mL buffer BB. The sample was now transferred to the QIAGEN Plasmid Plus spin column and drawn through it by applying approximately -300 mbar. The column-bound DNA was now washed by adding first 700 µl ETR buffer, and, after this is drawn through the column, by adding 700 µl PE buffer. To completely remove residual buffer, the column was spun at 10000 g for 1 min and then placed in a fresh microfuge tube. The DNA was eluted by adding 200 µl nuclease-free water, letting it incubate for 3 min and centrifuged at 10000 g for 1 min to collect the DNA in the tube.

4.2.10. Enzyme-linked Immunosorbent Assay

In preparation for the Enzyme-linked Immunosorbent Assay (ELISA), the needed constructs were transfected in a 6-well plate as described in section transfection but without coating. The next day, a clear 96-well plate was coated with 100µl/well 125µg/mL poly-D-lysine hydrobromide (Sigma-Aldrich Chemie GmbH), let sit for 30 min, and then thoroughly washed with PBS for three times before plating the cells. For this, the transfected cells were detached from the 6-well plate and seeded 30000 cells per well in 250µl standard cell culture medium per well. The cells were left to attach for 12 h, then carefully washed with PBS and fixed with Paraformaldehyde solution 4% in PBS (Santa Cruz Biotechnology Inc.) and incubated for min. 15min at RT. Thereafter, the plate was blocked with DMEM + 10% FBS for 1h at 37°C. In the meantime, a 1:200 dilution of the anti-HA antibody (Anti-HA-Peroxidase High Affinity (3F10) by Merck KGaA) was prepared in blocking buffer. The previous blocking buffer was then exchanged to 100 µl blocking buffer containing the antibodies and again left to incubate for 1h at 37°C. After that the cells were again washed three times with PBS. 0.4 mg /mL o-Phenylenediamine Dihydrochloride (OPD) (Thermo Fisher Scientific) was dissolved in preprepared buffer containing 0.05 M Citric acid monohydrate (99%) (Sigma-Aldrich Chemie GmbH) and 0.05 M Sodium phosphate (96%) (Sigma-Aldrich Chemie GmbH) at pH 5. Immediately prior use 4 µl of 30% hydrogen peroxide (Sigma-Aldrich Chemie GmbH) per 10 mL OPD was added and 100 µl OPD solution applied per well. Endpoint absorbance measurement at 450 nm was taken after 30 min incubation at RT. The reaction can also be stopped with 100

μ l 2.5 M sulphuric acid, thus readjusting the pH to 1. In this case the subsequent absorbance measurement was performed at 490 nm.

4.2.11. Microscopy

As a first step, before labeling, the transfection performance was checked by looking for green fluorescence after 488 nm excitation in the M2R-Mut8-EGFP transfected control-well. For all microscopy experiments with the Amber-mutant, the lyophilized Tetrazine-Cy3 or -Cy5 dye was resolubilized in DMSO to a stock concentration of 500 μ M. 27 μ l of this stock are added to 9 mL prewarmed FlouroBrite Medium and mixed (f.c. 1.5 μ M). The medium of each 6-well-plate well containing cells with an Amber-mutant transfection was changed to 1.5 mL staining mix and left to incubate at 37°C for 5min. Then the medium was changed to Flourobrite. Right before using the cover slip, it is washed twice to get rid of left-over unbound dye and imaged in 900 μ L FB buffer.

4.2.11.1. Line scan microscopy

All Line Scans were performed with the same basic settings as summed up in table and a laser intensity between 20 and 50%. The cells chosen for line scans were always also captured at 256x256 pixels, 50nm per pixel at the z-height and xy-position used for subsequent line scans. The x position was used for the line scan was always noted in the file name, making it possible to compare the used areas later-on when analysing the line scans.

For line scan analysis was the self-written Python code used. The function and structure are more closely described in section 5.4. The line scan is first transformed from a multi-paged lif format into a single column tif file by using the stacks 'make Montage' function of Image J. Afterwards the resulting tif is loaded into the 'LS main analysis' program. All basic settings for this analysis are kept the same for analysing the line scans of the M2R experiments as also the relevant acquisition settings were not changed and are given in table. A closer description of those parameters can be found in Appendix (F. The program output contains among other things a contour plot that shows the STICS function results Δ x or tau for optical feedback of the analyzed process, a plot showing the gaussian fits over tau to check if the fitting has worked and a csv-file with the MSD results (tau, MSD, SD). An example of the first two is given in Figure 4.1, which depicts a case of clearly visible diffusion in A) and an example with no detectable diffusion in B). Either the MSD results for the individual LS were than directly used for further analysis in GraphPad Prism or the contour plots for one experimental condition were collected as numpy readable matrices (npy-files, also automatically generated and saved when the code is run) and then cropped to common size and averaged with the other two Python-codes available on GitHub [82]. In GraphPad Prism the MSD curves were then studied to get insides into the receptor behaviour like diffusion coefficient (by fitting the linear part of the curve), confinement of the diffusion (plateauing) and particle size (y-intercept).

4.2. Methods

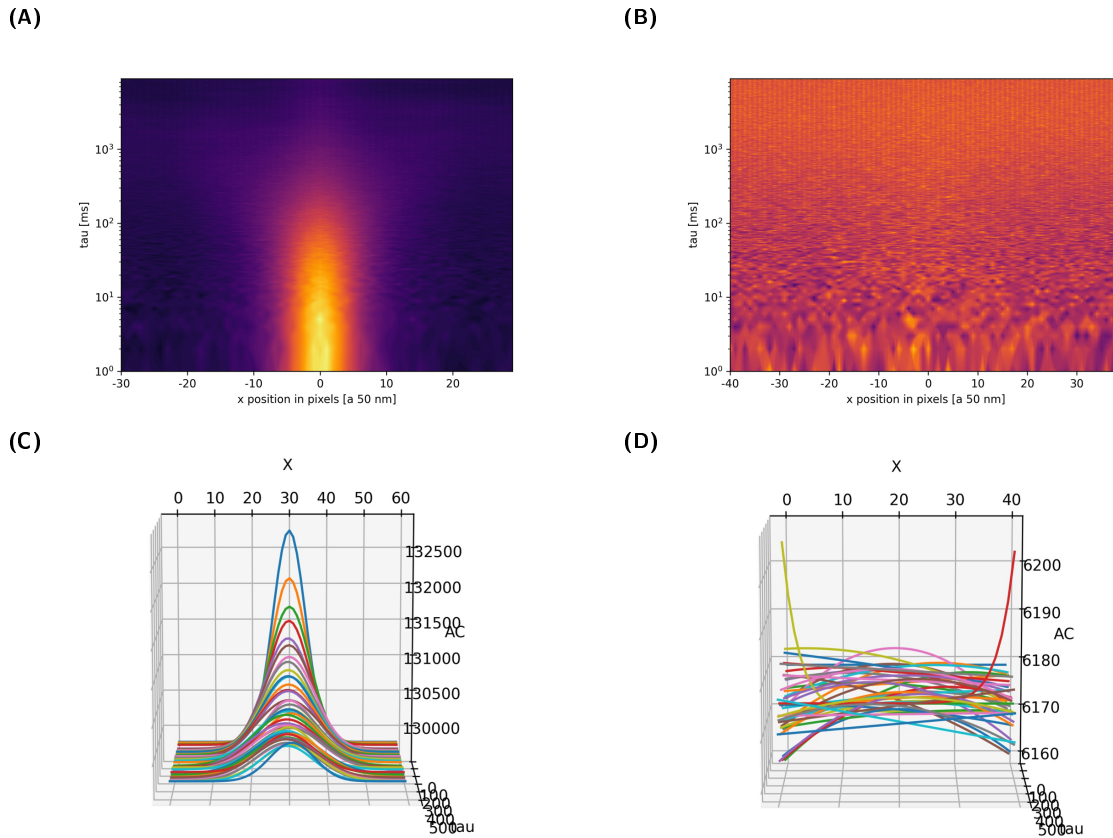


Figure 4.1.: Example STICS function plots and the corresponding Gaussian fits for a clear movement (left) or no detected movement (right). (A) shows the STICS function heat map with a typical plume shaped signal, (B) shows the STICS function heat map with no diffusion signal, (C) shows the Gaussian fitting result corresponding to (A) while (D) shows the fitting of (B).

Also the STICS function matrices of the same experimental condition were averaged and the averaged STICS function subsequently analysed. For this purpose, three additional small python scripts were prepared. One, that checks for the smallest STICS function matrix size in the data-set (depends on the smallest boundaries set by the user as explained above) and crops all matrices of that data-set to this size or a smaller size given by the user. A second script, that takes these cropped matrices (checks for identical sizes to be sure) and averages them to one STICS function matrix. Lastly, a script that simply takes the averaged matrix in form of a NPY-file as input and performs the analysis on this in the same manner as the 'LS main analysis'. All scripts can be viewed on GitHub [82].

4.2.11.2. Single Molecule Tracking

Extra clean coverslips were used for conducting single molecule tracking experiments, as the background due to labeled nonspecifically bound TCO*A on the glass surface needed to be minimized for TIRF microscopy. Therefore, the cover slips were plasma cleaned for 10 min (Zepto, Diener electronic GmbH & Co. KG), ultrasonically cleaned in Helmanex III 5% for four hours and washed three times by moving them through fresh ultrapure water baths and

stored in 6-well plates containing pure ethanol. The cell seeding, transfection and labelling was performed as described above. The movies were recorded six to eight hours after transfection. The applied settings are summed in table. The movies were then first processed in ImageJ and subsequently analyzed by the Matlab program ‘uTrack’. As uTrack needs single images to conduct the analysis, the movie was loaded into ImageJ, the contrast of the whole stack normalized (as the intensity values were not used in the subsequent analysis) and saved as single images. Additionally, an intensity sum picture over the whole stack was saved. In uTrack the functions ‘Detection’ and ‘Track analyses’ were used by applying point source detection. The exact settings can be viewed in the Appendix. The tracking results exported as ‘tracksFinal’ by uTrack were then used for MSD extraction by a Matlab function kindly provided by Holger Boltz (GitHub). The tracking results were filtered by using the ‘tracksfilter’ function on the tracking results and the sum intensity picture (tracksfilter(tracksFinal,Sum-imagename,mindiff,maxdiff,minlength,maxlength)). This prompts the user to define the area to use for the analysis as shown exemplary in Figure. After that the filtered tracks were analyzed by the ‘tracksdiffusion’ function. This results in the MSD data (τ_{MSD} [frames], MSD and SD [pixel^2] which was then converted to milliseconds (30ms per frame) and μm ($0.11 \mu\text{m}$ pixel-length) and saved as csv for subsequent analysis in GraphPad Prism just like done for the LS analysis.

4.2.12. Functionality Assay

The functionality of the M2R-Mut8 was checked by studying its ability to activate the downstream ERK signaling upon M2R-Mut8 stimulation with 1mM Acetylcholine. Therefore, the extracellular signal-regulated kinase activity reporter (EKAR) sensor (first generation [83], with Cyan Fluorescent Protein (CFP)/YFP. The EKAR phosphorylation induces a conformational change and thus increases the fluorescence resonance energy transfer (FRET) signal.) was co-transfected with the receptor (receptor: sensor 1:2) according to the procedure stated in section 4.2.2. Wells with EKAR-only transfected cells and M2R wild-type (wt) EKAR-sensor co-transfected cells were also included as controls. The FRET imaging was conducted 24h after transfection at the microscope setup described in table 4.13. The M2R mutants were Cy5 labelled according to the procedure described in section Microscopy and checked for expression before the FRET change measurements. An excitation of 430nm and emissions at 545 nm /480 nm was set to investigate the FRET changes YFP (mVenus) / CFP (mCerulean). The exposure time was set to 100ms and a delay of 5 seconds. After recording the basal FRET signal, the cells are stimulated by adding 1mM acetylcholine and the recording is continued until the signal has reached its plateau. Subsequently the YFP direct excitation is recorded for 5 to ten data-points at 500 nm excitation for later use in data correction. The movies were analysed with an Image J Action Bar Plug-In ‘ROI extraction’ that simplifies the ROI saving and Donor- and Acceptor-stack to single image saving, provided by Romy Thomas.

The first ROI must always be a cell-free area that was used for background correction. The mean raw intensity data for each ROI and time-point was then extracted by a python script written by me and subsequently analysed by a second python script written by Romy Thomas that does the corrections (Background, Bleed through and direct excitation) and calculates the FRET-ratio according to the procedure described in (2). The resulting FRET ratios over time were then visualized in Graph Pad Prism.

4.2.13. Programming in Python

All Python scripts were run in Python 3.9 (Python Software Foundation), developed using the PyCharm IDE (Community-Version, JetBrains) and pushed on GitHub (Microsoft) [82]. All use packages needed for running the scripts are also listed in individual requirement files for transparency and easy installation. The scripts can be downloaded from the repository: <https://github.com/LynnLangstrumpf/Master-Thesis>

5. Results

5.1. Expression of the M2R-Amber-mutant

Four different plasmid constructs were used for the work summarized in this thesis. The M2R-wt with and without EGFP at the C-terminus and both versions mutated at the amino acid position eight (M2R-Mut8).

The general composition of the construct is shown in Figure 5.2.

They always include a signal peptide (self-cleavable, derived from the human influenza hemagglutinin (HA) [8]) and a HA-tag at the N-terminus, followed by the receptor and in one version by a C-terminally positioned EGFP. The Amber mutation was introduced at position eight in both constructs as marked red in the M2R snake-plot in Figure 5.1.

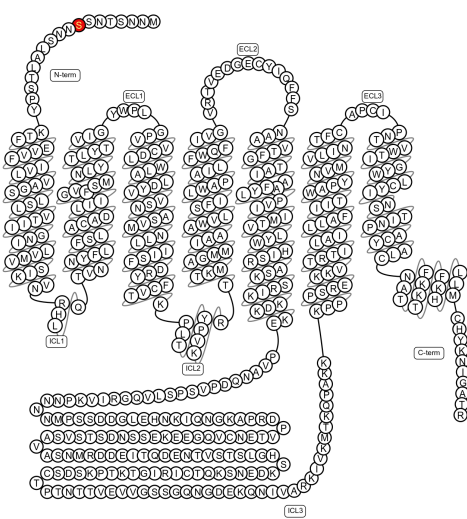


Figure 5.1.: Snake-Plot of the M2R.

The red marked amino acid position was Amber-mutated (TAG).
The plot was downloaded from: https://gpcrdb.org/protein/acm2_human/ [84]

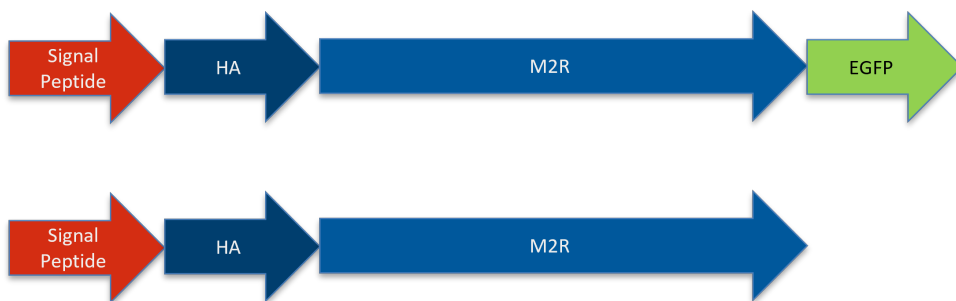


Figure 5.2.: Overview showing the composition of the M2R constructs

All used receptor plasmids encode for a signal peptide, followed by a HA-tag and the receptor. One version additionally contains an EGFP-tag at the C-terminus.

5.1. Expression of the M2R-Amber-mutant

After the successful introduction of the amber-mutation via site-directed mutagenesis, the membrane expression of the receptor variant M2R-Mut8 was checked by a whole cell ELISA targeting the N-terminal HA-epitope of the constructs. The results are summarized in the bar plot in Figure 5.3.

The absorbance result was background corrected by subtracting the mean signal of the non-transfected samples (i.e. zero absorbance) and subsequently normalized to the non-mutated, EGFP-free M2R version, thus setting its normalized absorbance to 1.

The M2R-wt version with the C-terminally added EGFP showed an even higher normalized absorbance of 1.18 [A.U.]. Both mutated versions showed significantly less absorbance signal with only 9% M2R-Mut8-signal compared to the wild type and only 6% for the M2R-Mut8 carrying the EGFP at its C-terminus. Therefore, the mutants are present at the membrane but in significantly lower amount compared to the wild type.

The next question is if the Amber-mutated construct can also be successfully labelled via SPIEDAC-reaction with a Tet-Cy3 dye. Therefore, the M2R-Mut8-EGFP was expressed and labelled as described in 4.2.11 and visualized with the confocal microscope.

An exemplary resulting composite image is shown in Figure 5.4. Only a fraction of the cells is expressing the receptor of interest (the EGFP signal, exited at 488 nm, is shown in green). While some cells show high intracellular EGFP signal, others are almost void of intracellular EGFP signal but show a clear, yellow membrane, indicating the green fluorescence of the receptor that is also labelled with Tet-Cy3 (excited at 561 nm, visualized in red in the figure). Those are the candidates for subsequent diffusion analysis experiments. Examples of the base-membrane of both, the M2R-EGFP variant

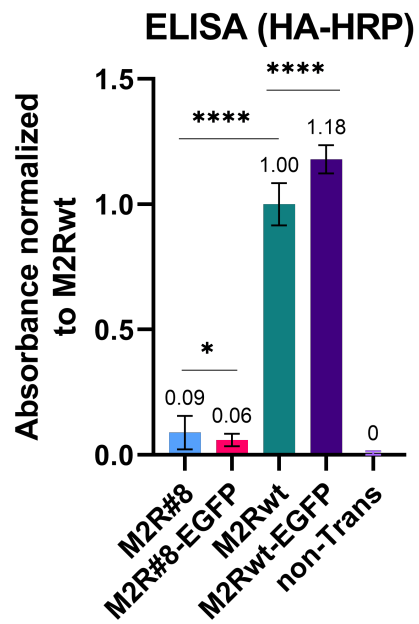


Figure 5.3.: Membrane expression check of the M2R variants by ELISA. The absorbance results are background corrected (non-transfected cells) and normalized to the M2R-wt absorbance. The error bars correspond to the SD and the numbers on top of each bar show the mean normalized absorbance. The Amber-mutated versions show only 5 to 9% absorbance when compared to the M2R-wt. (n=3)

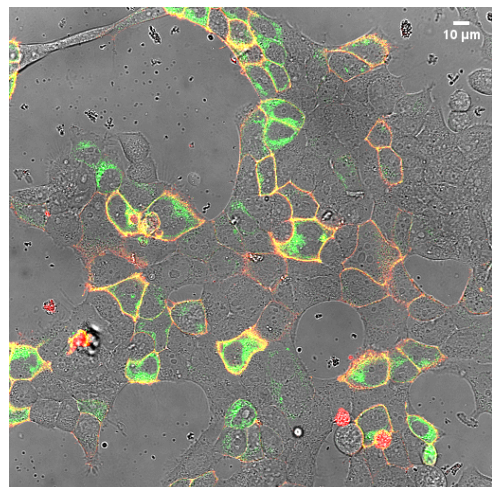


Figure 5.4.: Composite image of cells expressing M2R8-EGFP, Cy3 stained. The image shows a composite of cells expressing M2R8-EGFP. Green fluorescence (EGFP) is shown in green, and red fluorescence (Tet-Cy3) is shown in red. The image reveals a fraction of cells expressing the receptor, with some showing high intracellular EGFP signal and others showing a clear yellow membrane. A scale bar indicates 10 μm.

and the M2R-Mut8-EGFP, are shown in figure 5.5. The M2R-EGFP shows a clear membrane expression excited at 488 nm (green) but is not labelled by the Tet-Cy3 (561 nm, red) while the M2R-Mut8-EGFP shows a clear signal in both channels.

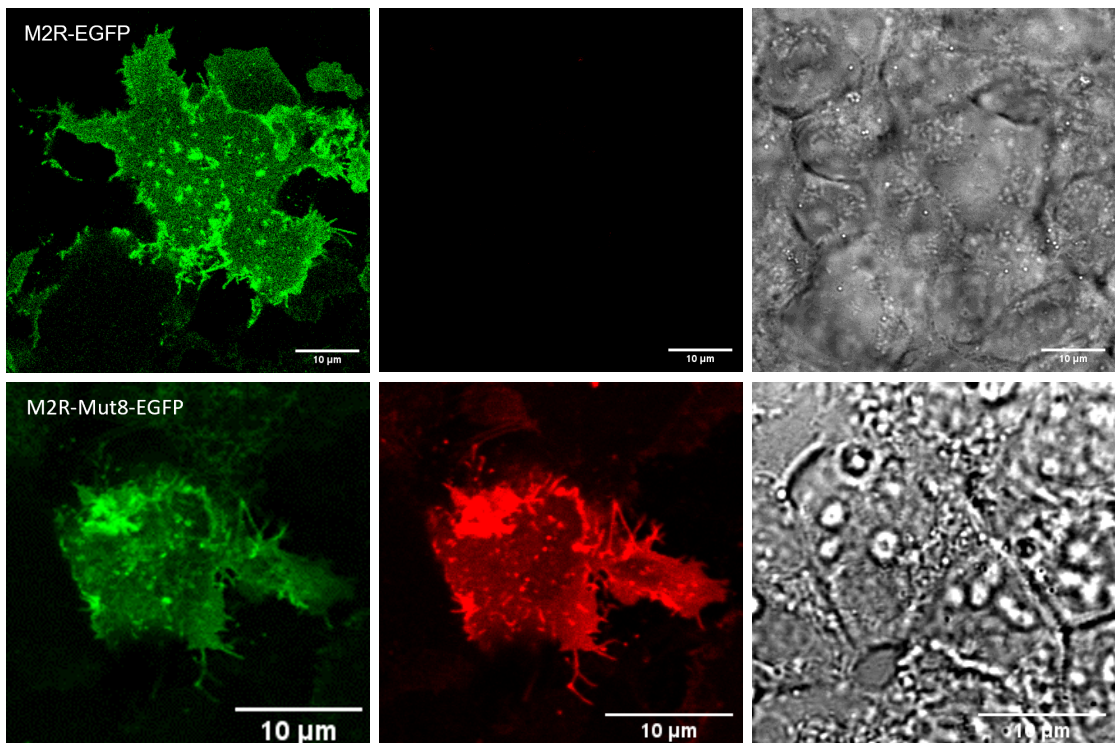


Figure 5.5.: Examples of the basal membrane of both the M2R-EGFP (upper row) and the M2R-Mut8-EGFP (lower row). From left to right excited at 488 nm (green), excited at 561 nm (red) followed by the DIC channel. The samples were labelled with Tet-Cy3.

A consistent workflow was performed when selecting areas for LS experiments, as shown in Figure 5.6. From left to right: the Tet-Cy3-labelled M2R-Mut8 transfected cells were first checked for a cell showing a clearly defined membrane in the Cy3-channel, zoomed, and focused onto its base membrane (middle picture). Then, it was set to a 50 nm per pixel magnification with a picture size of 256x256 pixels (right upper). The position of the LS was then chosen to incorporate as little inhomogeneities as possible. A look at the base membrane in figure 5.6 shows areas of an evenly membrane, homogeneously labelled with Tet-Cy3, therefore areas with membrane located M2R-Mut8 and usable for LS experiments. A typical line scan profile (1x265 pixels) is shown in figure 5.7. The x-axis corresponds to the length of the acquired line while the pixel-intensities (Gray Value) are plotted against the y-axis.

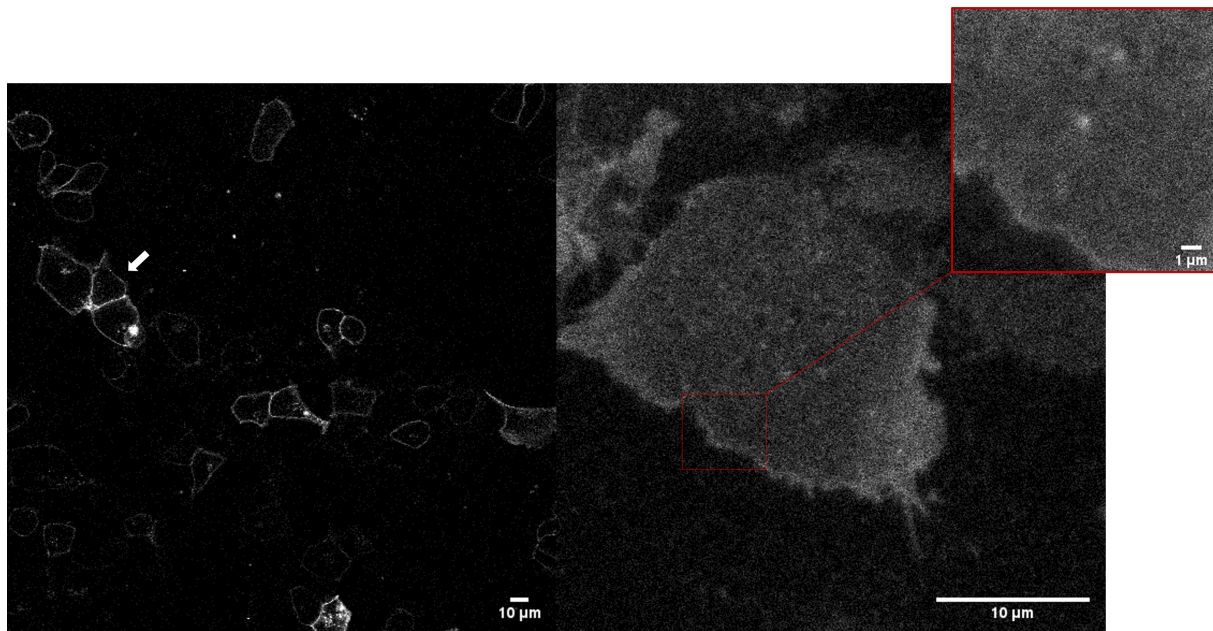


Figure 5.6.: Exemplary cell used for LS experiment, Cy3-channel.

From left to right: First a suitably well labelled cell is chosen, subsequently focused on its base membrane, and set to a 50nm/pixel 256X256 image size. From here, a homogeneous line of pixels is chosen for the LS acquisition.

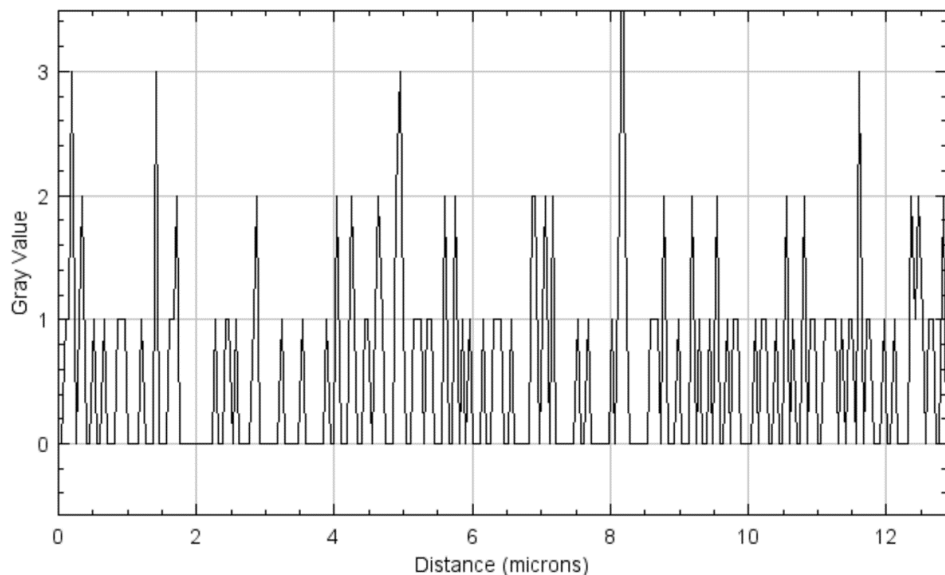


Figure 5.7.: Exemplary line intensity profile. Line width: 256 pixel a 50 nm. Visualized in ImageJ.

5.2. Functionality of the M2R-Amber-mutant

The functionality of the M2R-Mut8 must be ensured when aiming to investigate the actual diffusion behaviour of the M2R in different activation states by LS microscopy. Therefore, it must be verified that the mutation does not impede the receptors' ability to get activated by its ligand and thus still induces the G_i-signalling cascade in the cell. This was checked by co-transfected an EKAR-sensor and measuring the FRET-changes upon stimulus with 1 mM ACh as described in Methods.

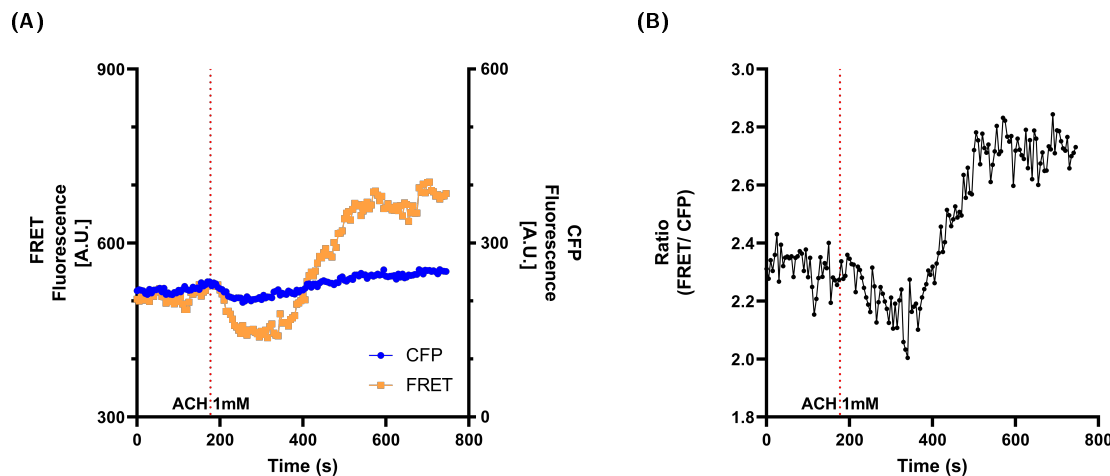


Figure 5.8.: Exemplary FRET-change measurement: M2Rwt-EKAR co-transfection. (A) individual fluorescence intensity over time for the donor- (CFP) and the FRET channel. (B) FRET/Donor ratio.

Cells bearing the M2R-wt co-transfected with the EKAR-sensor, as well as EKAR-only transfected cells, were used to check the proper functioning of this downstream activation assay. Figure 5.8 shows an exemplary set of traces for a M2R-wt, EKAR co-transfected cell. The EKAR-sensor gets activated by phosphorylation by extracellular signal-regulated kinase (ERK). The conformational change upon activation leads to a positive FRET-change [83]. The red dotted line indicates the time point of stimulation by hand-addition of ACh to a final concentration of 1 mM. The individual fluorescence intensities of the donor (plotted against the right y-axis, blue) and the FRET-signal (left y-axis, orange) are delineated in 5.8A. After an initial period of stable fluorescence signal in both channels, there is a considerable drop in the intensities of both channels directly after pipetting the ACh onto the coverslip. This 'addition effect' due to fluid disturbance is an artefact of the method and is visible in several traces. After this drop, the donor channel recovers its initial height after about three minutes. In the case of the FRET signal, the intensity increases considerably till it reaches its plateau five to seven minutes after stimulating the cells. Figure 5.8B shows the FRET signal of the cell as a ratio of the FRET and CFP intensities. Alike the individual traces, it features a constant ratio before stimulation, a slight decrease in FRET signal as addition effect, and then a step

5.2. Functionality of the M2R-Amber-mutant

increases in FRET/donor ratio. It thereby visualizes the activation of the EKAR sensor by a higher FRET signal compared to the CFP channel after stimulation. A second example of such a M2R-wt co-transfection with the EKAR-sensor is given in figure A.1 of the Appendix. Here as well, the plateau is reached after about five minutes. These activation time-scales are consistent with those shown in “A genetically encoded fluorescent sensor of ERK activity” [83], wherein the sensor was characterized.

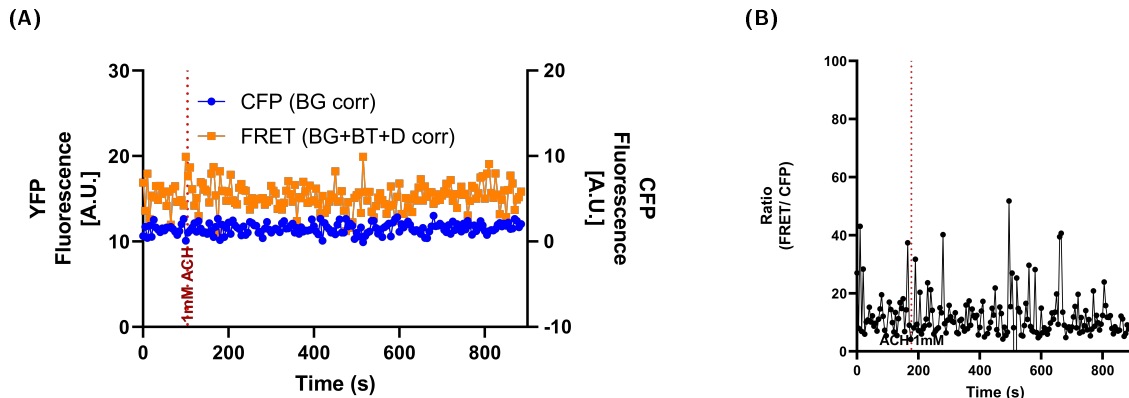


Figure 5.9.: Exemplary trace FRET-change measurement: extracellular signal-regulated kinase activity reporter (EKAR)-only transfection. (A) individual fluorescence intensity over time for the donor- (CFP) and the acceptor-fluorophore (YFP). (B) Acceptor/Donor ratio. No ratio change upon stimulation detectable.

Figure 5.9 shows exemplary data of a EKAR-only transfected cell. Alike in the above shown graph, the donor fluorescence intensity is plotted against the right y-axis in blue and the FRET-signal against the left y-axis in orange. There is no reaction upon stimulation visible. Also, the FRET/CFP ratio shows no increase after stimulation.

The outcome of these two control experiments allows the conclusion, that the assay is working as the M2R-wt can induce downstream ERK signaling after activation by ACh while the EKAR-only transfected cells showed no reaction.

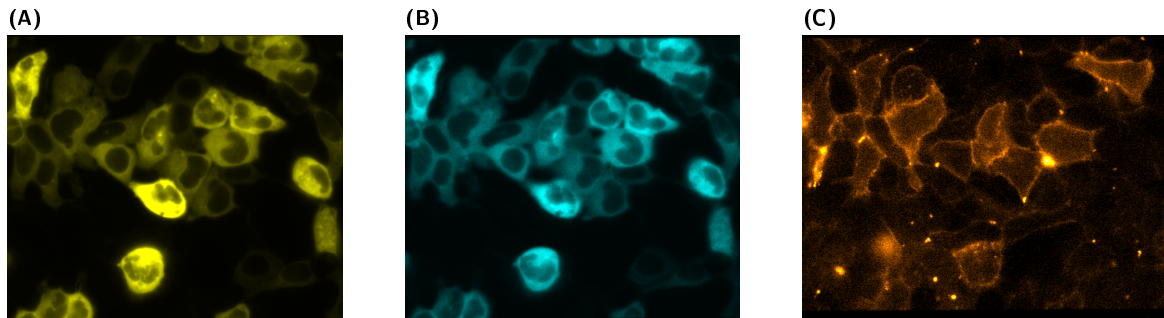


Figure 5.10.: Exemplary M2R-Mut8 cell cluster as used for the functionality assay. (A) and (B) show the cytosolic expression of the EKAR-sensor, both, in the YFP-channel (A) and the CFP-channel (B). The same cluster is also checked for the M2R-Mut8 membrane expression in the Cy5-Channel (C).

Before using the same assay on the M2R-Mut8 EKAR co-transfected cells, those cells were la-

labelled with Cy5-Tetrazine (Tet-Cy5) and checked for M2R-Mut8 expression in the Cy5 channel to be sure to analyse cells that contain both, the receptor and the sensor. An exemplary cell cluster used for the functionality assay is shown in figure 5.10. The cytosolic sensor expression is visible in both, the YFP-channel (A) and the CFP-channel (B). The Cy5-signal after labeling (visualized at the inverted microscope used for the FRET measurements) is given in Figure 5.10 (C). It is evident from these pictures, that the cells with particular strong Cy5 signal are those with a more moderate sensor expression.

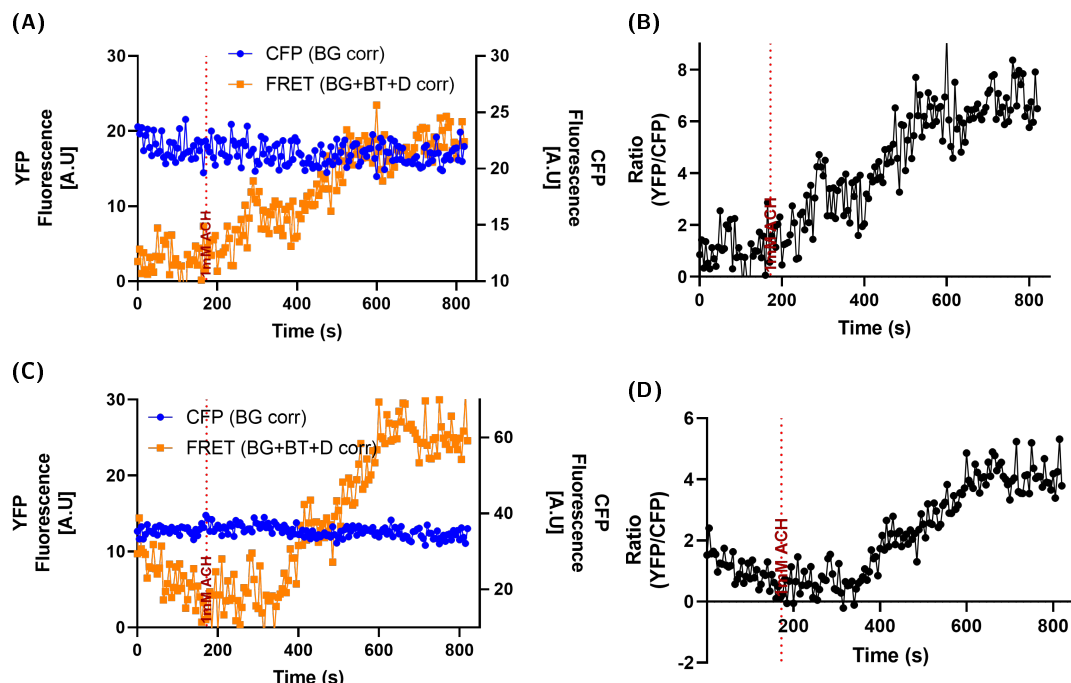


Figure 5.11.: Exemplary trace FRET-change measurement: M2Rwt-extracellular signal-regulated kinase activity reporter (EKAR) co-transfection. Left: individual fluorescence intensity over time for the donor- (CFP) and the acceptor-fluorophore (YFP). Right: Acceptor/Donor ratio. Examples of two individual cells, (A,B) and (C,D).

Exemplary individual traces for cells co-transfected with M2R-Mut8, the orthogonal system and EKAR are given in Figure 5.11. The fluorescence intensities of most of the analysed cells are lower than those of the M2R-wt EKAR co-transfected cells shown above. This might be explained by a lower general sensor expression due to the fact that, additionally to a receptor and the sensor, now also the bioorthogonal system needs to be expressed by the cell. Therefore, starting from considerably lower values but otherwise similar to the M2R-wt example, there is a distinct increase in FRET-signal visible after stimulation with 1 mM ACh and a plateau reached after five to seven minutes. Thus, the functionality of the mutated and labelled M2R receptor can be shown on a single-cell level.

These single-cell results can also be summarized by normalizing the individual timelines (setting the stimulation time-point to 0 seconds) and additionally normalizing the FRET-ratios (setting

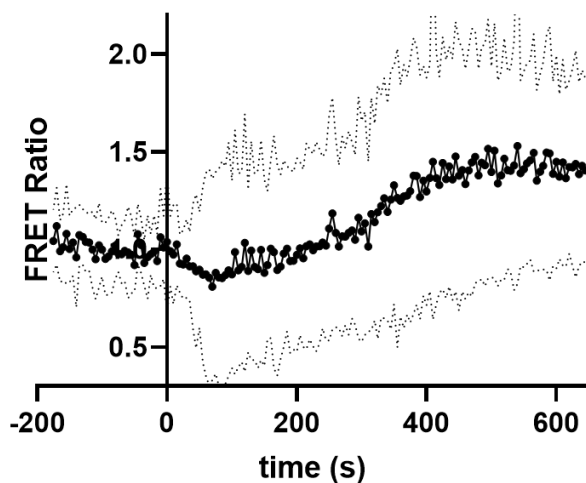


Figure 5.12.: Averaged ratio of the FRET-change measurements of all M2R-Mut8-EKAR co-transfections ($n=40$). The 95% confidence interval is marked as dotted line. Stimulation at 0 seconds.

the pre-stimulation FRET-ratio to one). The resulting mean and the 95% confidence interval are shown in figure 5.12. The mean FRET ratio is here again seen to be constant before stimulation. A small decrease in the FRET ratio values represents the addition effect right after stimulation which is present in some samples. Then it shows an increase in FRET ratio up to a plateau after about six minutes post stimulation, thus confirming the performance observed in the individual cell traces. The confidence interval broadens after stimulation. This might be explained, both, by the sometimes-present addition effect and by the varying sensor expression strength in different cells and on different days (a total of 40 cells is averaged in this graph).

5.3. Developing a Python3 script for line-scan analysis

The aim of this thesis was to analyse the change of the M2R diffusion behaviour upon activation using line-scan-FCS. In order to do so, we worked to develop a script for analysing line-scan data by extracting spatial-temporal correlation spectroscopy functions (STICS), using Python.

The logical first step was to understand and implement the classic STICS function as introduced before in section 3.6.4. Thus, the initial first variant of the script (version 1) simplified the problem to a one-dimensional autocorrelation as stated in equation 5.1.

$$G(\tau) = \frac{\langle I(t) \cdot I(t + \tau) \rangle}{\langle I(t) \rangle^2} \quad (5.1)$$

The temporal image correlation of each x-position of the line was calculated individually, binned, and in the end averaged to a common autocorrelation curve over τ as given in 5.14A. This procedure is depicted in 5.13. It shows an exemplary LS (not scaled). Each row along the x-axis refers to the very same line (for example positioned at the base membrane before acquisition as mentioned in 5.6). Every subsequent row along the time axis shows thus the same line (spatial position) but at changing time points. Therefore, the line features changing intensities at the individual pixels as particles are diffusing in and out of the line of view. The window of calculation (red rectangle) is moved column by column over the acquired LS. The initial script included nested FOR-loops that calculated, binned, and averaged the FCS for every x-position of a LS and gave the mean AC function over τ as output. The calculation time using this approach exceeded 10 h per LS, even after a process parallelization over x was implemented. This was caused by the interlacing FOR-loops which inherently imply a sequential and therefore inefficient calculation that still handled one τ -interval at a time. The resultant AC plot of this procedure for a test-dataset is shown in 5.14A. The test-dataset used here was taken from the publication ‘Line-scan microscopy data to extract diffusion coefficient of a fluorescent species using a commercial confocal microscope’ [15] which provides benchmark line scans and corresponding AC plots. The paper encompasses, among other things, three individual LS of Alexa647 diffusing in different glycerol concentrations (50%, 70%, and 90% glycerol). Those were used for testing the individual stages of the script during the development as outlined in the next few pages.

The side-by-side comparison (figure 5.14A) of the AC curves generated by the LS analysis script (version 1) and those of the reference paper shows that the rough general curve char-

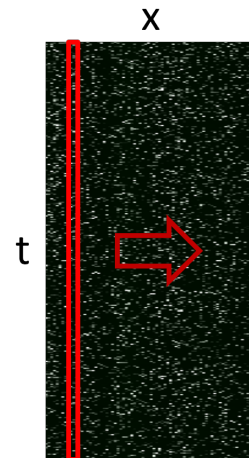


Figure 5.13.: A outline of the STICS function calculation in its simplified version (t only). The temporal image correlation as stated in 5.1 is calculated for every column of the LS, binned and subsequently averaged over x. This results in a autocorrelation curve as is given in 5.14A

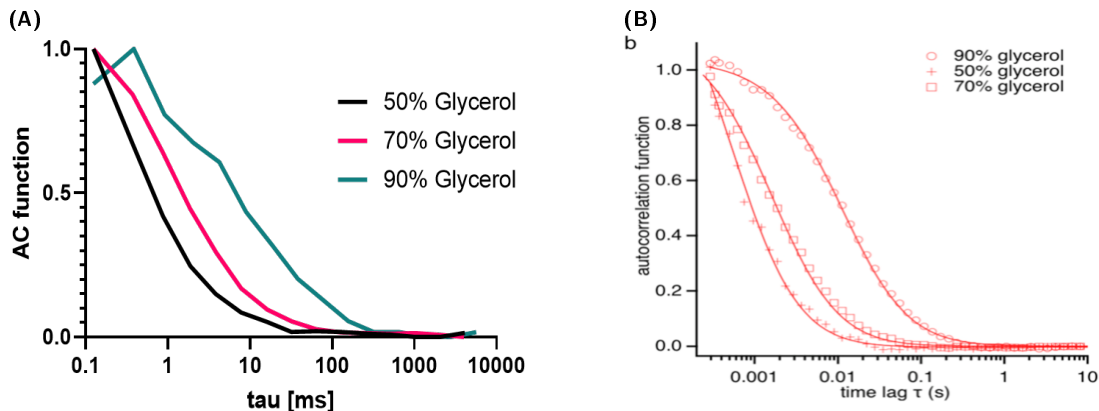


Figure 5.14.: Side-by-side comparison of the AC curves generated by the LS analysis script version 1 and those of the reference paper. (A) shows the normalized autocorrelation curve over τ calculated by the simplified STICS function 5.1 of the Python script version 1. (B) shows the reference autocorrelation curves taken from Figure 2b) ‘Line-scan microscopy data to extract diffusion coefficient of a fluorescent species using a commercial confocal microscope’ [15]. In both cases is the τ axis scaled logarithmically while the AC-axis is in linear scale.

acteristics are reproduced. The 50% Glycerol shows the fastest drop, followed by 70% and ending with 90% having the smallest decline but also showing a additional maximum between tau 0.1 and 1 ms. Also, the levelling-off τ -values are alike in both graphs. Therefore, it can be stated, that this approach works for a initial approximation of the diffusive behaviour readout from LS. Still, the binning of this first analysis is too rough and the processing time per LS too big to be practical.

The next step was to replace the autocorrelation calculation over time by a Fourier-transformation based calculation over time (1DFFT), subsequently by a calculation over time and space individually calculated (2x1DFFT) and combined into one two dimensional Fourier-Transformation calculation (2DFFT). This is grounded on the theoretical reasoning outlined in the introduction 3.6.4. An overlay of the AC curves of all three calculation methods using FFT can be found in the Appendix (B.2). They result in almost identical curves, making it possible to choose the two dimensional FFT calculation as being the fastest performer.

The overlay of the AC curves of the very first version shown above and the finally used 2DFFT calculation is given in 5.15A. The binning of the 2DFFT calculated curves is much finer (as visible in the finer curve shapes and the standard deviation (SD) lines) but otherwise overlaps nicely with the first AC calculation for the 50% and 70% Glycerol samples. The 90% sample 2DFFT diverges more from the roughly binned, first AC curve. It includes the local maximum around $\tau = 1$ ms that also influences the curve shape depending on the binning and leads to the shift of the 2DFFT curve compared to the version 1 curve. This local maxima is also visible in the AC curve of the reference paper 5.14B.

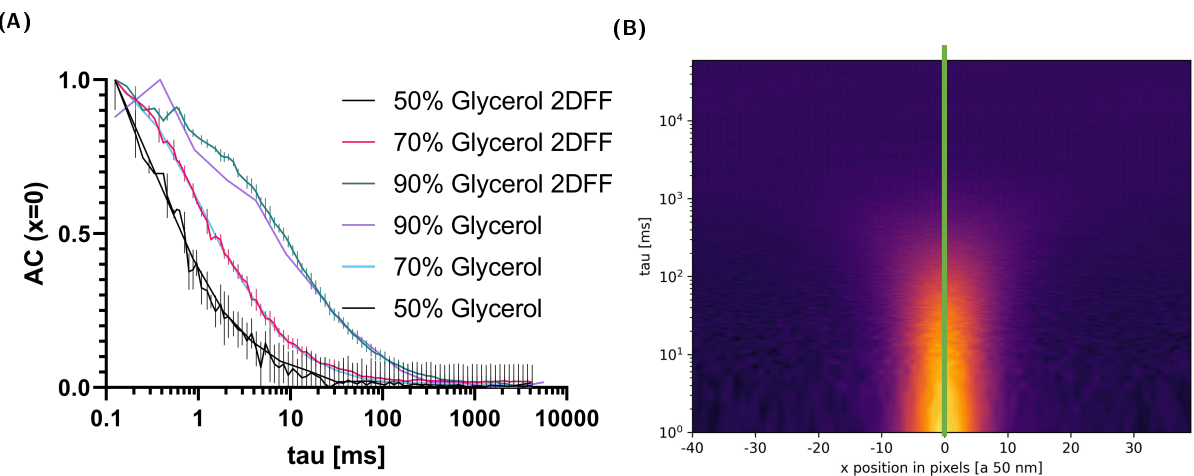


Figure 5.15.: The AC curve overlay of the initial and finally used calculation method (A). It shows the normalized autocorrelation curve over τ calculated by the simplified STICS function 5.1 of the Python script version 1 and the calculation using the 2DFFT approach. (B) shows an exemplary STICS function heat map (90% Glycerol) with the position of the AC curves as depicted in (A) indicated as a green line.

As the two dimensional FFT calculation results in a spatio-temporal image correlation and thus not only includes the information of the change over time but also over space, the resulting STICS function heat map is exemplary given for the 90% glycerol LS in 5.15B. The previously discussed AC curves are a integral part of this matrix and here depicted as colour change from light yellow (high values) to dark purple (small values) along the τ axis at position $x=0$ (position indicated by the green line).

The STICS function incorporates information about the diffusive behaviour in two different dimensions. Thus, there are also two strategies how to harvest these information. One possibility is to fit a diffusion model (here 3D diffusion as previously introduced in equation 3.7 in section 3.6.4) to the AC curve and thus directly read-out the diffusion coefficient D . This method was applied to the glycerol samples. The corresponding AC curve fits and STICS heat maps are summarized in B.3 of the appendix. The matrix of the STICS function also contains information about the changes in the spatial dimension. The spacial changes are evident as Gaussian curves along the x-axis at a constant τ -value. This is visible when looking at the colour change in the heat map along the x-axis as shown in figure 5.16A. Thus, it is also possible to fit these changes and subsequently calculate the MSD from the σ -values of the individual Gaussian fittings according to the equations 3.9 and 3.10 as introduced in section 3.6.4. Such a Gaussian profile of a STICS function is given in 5.16B for the 90% glycerol sample. The MSD values obtained from the Gaussian fits are further plotted against their corresponding τ -values and linearly fitted. The slope of the linear section of the plot (small τ -values) correlates to the diffusion coefficient, depending on the diffusion mode (2D: equation 3.8 or 3D: equation 3.7). The y-intercept of the fit correlates to the particle size and the

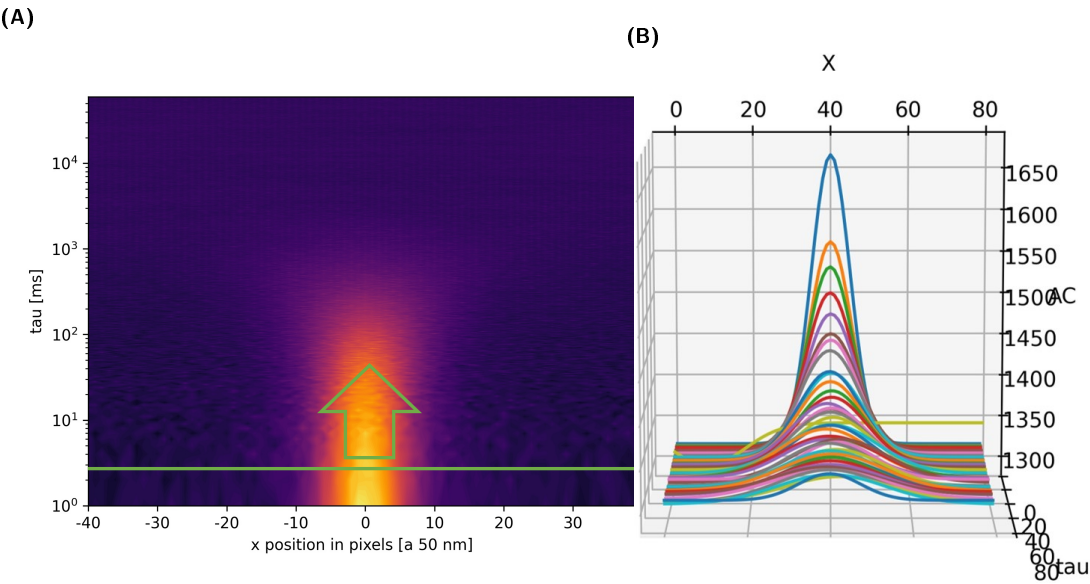


Figure 5.16.: Example for the diffusion analysis by Gaussian fitting along the x-axis. Exemplary STICS function heat map (90% Glycerol) (A) with the position of the Gaussian fits indicated as a green line, progressed τ value by τ value indicated by the arrow and resulting in a Gaussian curve collection along τ as given as an example in (B). The amplitude of the Gaussian functions decreases over τ while σ increases. Every 25th fit is plotted. One τ -step corresponds to 14.75 ms.

resolution limit of the used system. The MSD-plot of the glycerol-LS is shown in 5.17. The curve with the highest slope and thus highest D is the 50% glycerol sample (black), followed by the 70% glycerol (green) and the 90% glycerol sample with the smallest diffusion coefficient.

The resulting D-values and particle sizes derived by the thus far applied methods are summarized in table 5.1 with the first column stating the glycerol concentration and the second column the experimental diffusion speed as it was derived by the authors of “Linescan microscopy data to extract diffusion coefficient of a fluorescent species using a commercial confocal microscope” [15]. The other two columns give the results of the analysis performed within this thesis. First, the diffusion coefficients from the Gaussian fitting along the x-axis and MSD-plot analysis. Second, the AC curve fit performed along the time axis at $x=0$. For the fastest diffusion, evident in the 50% glycerol sample, the Gaussian fit method yields a $D = 50 \pm 5 \mu\text{m}^2/\text{s}$ compared to $53 \pm 3 \mu\text{m}^2/\text{s}$ as stated in the paper. The AC curve fit on the other hand seems

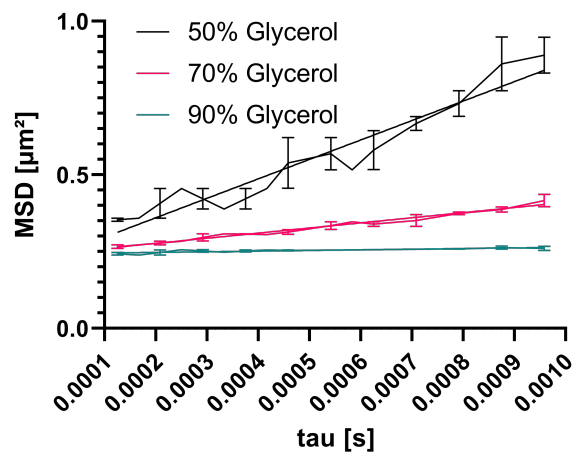


Figure 5.17.: MSD plot of the glycerol samples derived from the σ values of the Gaussian fits. The MSD - τ value pairs where linear fitted and the slope used for D calculation according to equation 3.1.

to underestimate D with $36 \pm 1 \mu\text{m}^2/\text{s}$. When taking the visual fitting result of this sample into account (Figure B.3), it also shows a downshift of the fit (orange) compared to the data (blue) for low τ values, resulting in a lower D.

For the 70% Glycerol sample, both calculation methods implemented in Python agree on a D around $15 \mu\text{m}^2/\text{s}$ compared to the $17 \pm 1 \mu\text{m}^2/\text{s}$ calculated by [15]. The slowest diffusing sample containing 90% glycerol should show a D of $2.45 \pm 0.05 \mu\text{m}^2/\text{s}$ according to the reference values but shows a diffusion coefficient of $1.8 \pm 0.4 \mu\text{m}^2/\text{s}$ when analysed by Gaussian fitting and a D of $3.36 \pm 0.07 \mu\text{m}^2/\text{s}$ when done so by AC curve fit.

Based on these results we could assess that the developed Python script provides a correct STICS function and can output proper diffusion values. For the AC fit, the fast diffusion (50% Glycerol sample) seems to get underestimated.

Table 5.1.: Diffusion coefficients calculated with two different methods and the corresponding values given in the paper

Glycerol [%]	reference Paper D [$\mu\text{m}^2/\text{s}$]	Gaussian fit D [$\mu\text{m}^2/\text{s}$]	AC ($x = 0$) D [$\mu\text{m}^2/\text{s}$]
50	53 ± 3	50 ± 5	36 ± 1
70	17 ± 1	15.4 ± 0.6	15.6 ± 0.3
90	2.45 ± 0.05	1.8 ± 0.4	3.36 ± 0.07

5.3.1. Verifying the results of the Python-implemented line-scan analysis

The results from the Python analysis method were now compared to those generated by the benchmark script generally used in the 'AG Receptor signaling'[5]. The goal of this comparison was to validate the analysis results and identify possible differences. We used a simulated data set with a known diffusion coefficient of $0.1 \mu\text{m}^2/\text{s}$ for this purpose. [5]. The output of the Igor-implemented analysis [10] was exported as the STICS function (matrix) and also as MSD - τ value pairs in table-format.

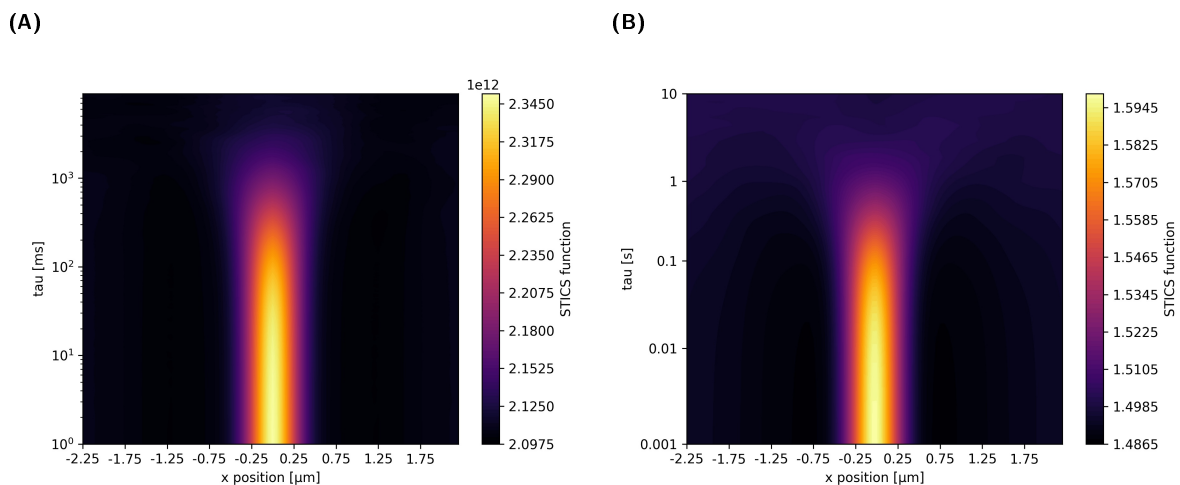


Figure 5.18.: The STICS function of the simulated test-data with D set to $0.1 \mu\text{m}^2/\text{s}$ visualized as heat map. (A) shows the non-binned STICS result from the Python analysis while (B) shows the STICS matrix calculated in Igor and in that process averaged in 64 logarithmic bins and subsequently visualized in Python. In both cases the plotting settings are otherwise the same with the contour levels set to 100 for high resolution.

Figure 5.18 shows the respective STICS functions as heat maps. (A) shows the result generated by the Python script. This means the not binned STICS function calculated by 2DFFT as explained in the previous section. (B) depicts the STICS function as exported from the Igor-analysis. Here, the STICS function is binned logarithmic in 64 bins along the τ -axis. Therefore, the resolution of the STICS function as heat map is limited. It is clear that the relative plume shapes are alike while absolute values differ by orders of magnitude. This may be explained by different methods of LS to intensity-matrix imports. The pixel intensity matrix shows a scale ranging between 10^2 and 10^4 when the LS are imported by Pythons scikit-image package [85]. Visualizing the grey scale e.g. in ImageJ results in a grey-scale ranging in magnitudes between 0 and 10^1 as seen in figure 5.7. This can also impact the accuracy of the intensity matrix. However, the gradients within the matrices are more crucial for a correct end-result than the absolute values, as the subsequent analysis uses the variance and not the individual absolute values within the STICS function matrix. The Igor plume seems to show more broadening and generally higher relative values in the area over $\tau = 1\text{s}$. Besides being influenced by the

underlying intensity matrix, this might also be influenced by the choice of algorithm for the FFT calculation, as different algorithms can output slightly different outcomes. Many other individual choices in writing the code do also exert an influence. Examples are pre-calculation data corrections (e.g. bleaching correction) or binning settings. A clearer comparison is feasible by looking at the AC curves at $x=0$ as shown in figure 5.19.

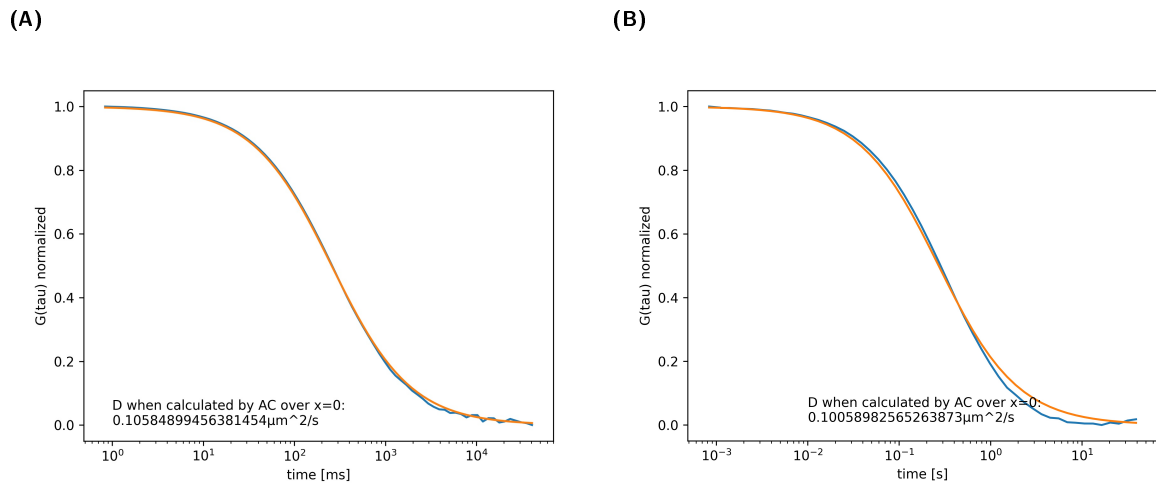


Figure 5.19.: The auto-correlation curve fittings (orange) performed on the STICS results as depicted in 5.18 at position $x=0$ (change over time, blue line). In case of the pure Python analysis (A), this results in a diffusion coefficient D of $0.106 \mu\text{m}^2/\text{s}$, while the AC fit on the Igor calculated STICS values (B) results in $D = 0.101 \mu\text{m}^2/\text{s}$.

The figure 5.19A shows the AC curve fit of the pure Python analysis. The fitting (orange) nicely retraces the underlining STICS data (blue) over all τ points. This fitting results in a diffusion coefficient of $0.106 \pm 0.001 \mu\text{m}^2/\text{s}$. The fit over the Igor-derived analysis diverges from the actual data for τ over 1s because it encompasses a slight rise beginning at about 10s that can not be captured by the function for the 2D diffusion. The resulting D of this fit is $0.101 \pm 0.001 \mu\text{m}^2/\text{s}$. The Gaussian fitting method was also applied to both STICS functions shown above and the thus ex-

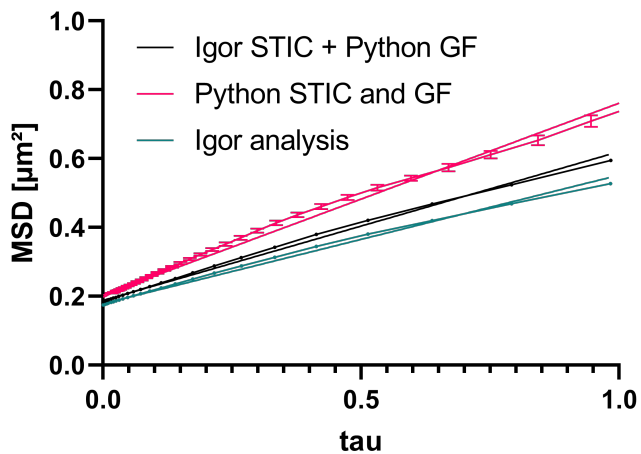


Figure 5.20.: The resultant MSD plots when analysing the diffusion behaviour in three different ways and applying a linear fit for $\tau < 1$ second to obtain the diffusion coefficients. The reference analysis method, all calculations done in Igor is delineated in green. The plots generated by Gaussian fitting the STICS functions shown in 5.18 are colour-coded in pink for pure Python analysis and black for Python Gaussian fitting upon the STICS result of the Igor analysis.

tracted MSD - τ value pairs are plotted in figure 5.20. Already, by just looking at the graphs, it is evident, that the pure Python analysis (pink) shows the highest slope (and therefore highest diffusion) followed by the Gaussian fitting (Python) when applied to the Igor-STICS function (delineated in black). The MSD - τ value pairs as exported from the purely Igor analysis are added in the figure in green. This curve shows the smallest slope. All analysis methods agree on a y-axis intercept around $0.2 \mu\text{m}^2$. The absence of standard deviations in the to Igor-derived plots is caused by the fact that the corresponding STICS function was already binned before applying the analysis while the purely Python analysis was non-binned previous to the Gaussian fitting (as explained in figure 5.18) and only the resulting MSD - τ value pairs were in the end logarithmically binned.

Table 5.2.: Diffusion coefficient and particle size from one test dataset when analysed with different methods and programs as shown in more detail in 5.19 and 5.20.

	D [$\mu\text{m}^2/\text{s}$]	particle size [μm]
ACC fit in Python on Igor STICS	0.101 ± 0.001	0.33 (set parameter)
ACC fit all Python	0.106 ± 0.001	0.33 (set parameter)
Gaussian fit Python on Igor STICS	0.108 ± 0.001	0.31 ± 0.02
Gaussian fit all Python	0.139 ± 0.001	0.32 ± 0.03
All Igor analysis (MSD vs. τ)	0.093 ± 0.001	0.30 ± 0.03

The results outlined in this section are summarized in table 5.2. Comparing all extracted D values, it is evident, that the AC curve fits performed best on this simulated data set, together with the combination of the Python-performed Gaussian fit upon the Igor-derived STICS function. The purely Python analysis overestimates the diffusion coefficient with $D = 0.139 \pm 0.001 \mu\text{m}^2/\text{s}$ while the pure Igor analysis underestimates it with $D = 0.093 \pm 0.001 \mu\text{m}^2/\text{s}$. All three Gaussian fittings agree on a particle size of around 300 to 320 nm. All in all the results are in qualitative agreement.

5.4. Analysing the diffusion behaviour of the M2R-Mut8 - Cy3

The previous section demonstrated, that the script is functional and yields reliable results. Therefore, it can be used to analyse LS experiments. The analysis workflow, including the steps performed within the script, is now shown in more detail for one of the M2R-Mut8 non-stimulated LSs.

The cell used in this example is shown in figure 5.21. (A) shows the base membrane of the whole cell while (B) shows the magnification used for the LS acquisition, the line position

is indicated in yellow.

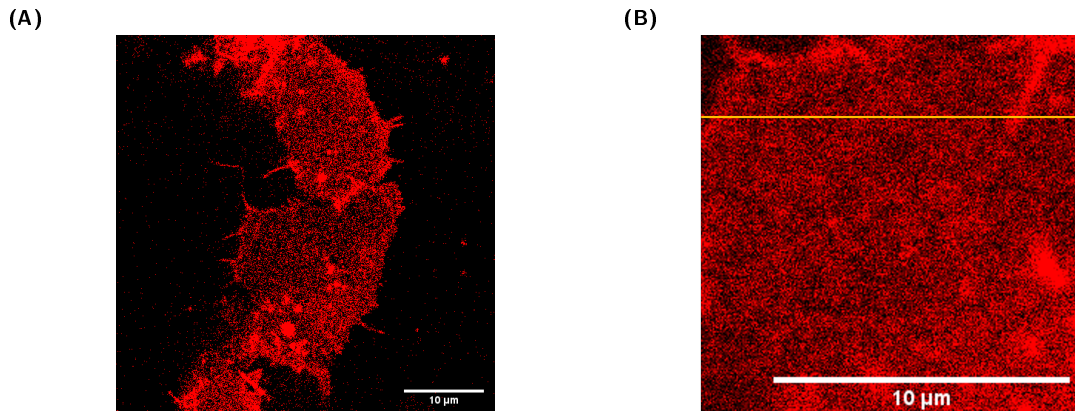


Figure 5.21.: The cell of the experiment example shown in this section. (A) shows the base membrane of the whole cell while (B) shows the magnification used for the LS acquisition, the line position is indicated in yellow.

First, the LS needs to be saved as a one-paged tif file and is loaded into the 'data' folder within the Python environment. The settings of the script 'LS mainAnalysis' need to be checked and adapted according to the used acquisition settings as explained in more detail in section F (Appendix). Now the script 'LS mainAnalysis' is executed. The script loads the tiff and converts it to a numpy matrix with the individual pixel intensities as values. The y-axis of the matrix corresponds to the time points. Therefore, it is in the same orientation as the exemplary LS already shown in figure 5.13 in another context.

The user is now prompted to give an identifier, which in turn is used from there on to mark all script-analysis exports derived from this LS. Then, it shows a pixel intensity-sum plot over the line-width and subsequently over the time-axis as shown for the example LS in figure 5.22. The intensity-sum over line-width plot has in this case sharp peaks around 500 and 10 000 nm which must be avoided, but it also encompasses a quite flat region between 1000 and 9000 nm. This region was chosen for the analysis. The strong bleaching up to 50 000 ms was also excluded. In order to be reproducible, all user-made decisions throughout the Python-analysis are documented and exported in a csv-file, flagged with the Identifier named beforehand.

The user settings now completed, the script calculates the STICS function and prints the result as a heat map. It also saves it as numpy-matrix in a NPY-file (binary file format [86]) for later use. Subsequently it first fits the AC curve, prints the fitting result as plot for the user and saves the τ -AC value pairs as csv-file. Afterwards it proceeds to do the Gaussian fitting along the x-axis for every τ . All graphs for the example LS are shown in figure 5.23.

The STICS function plot in figure 5.23A shows a clearly defined plume, thus moving particles have been found by the analysis. A counterexample of a STICS function where this is not

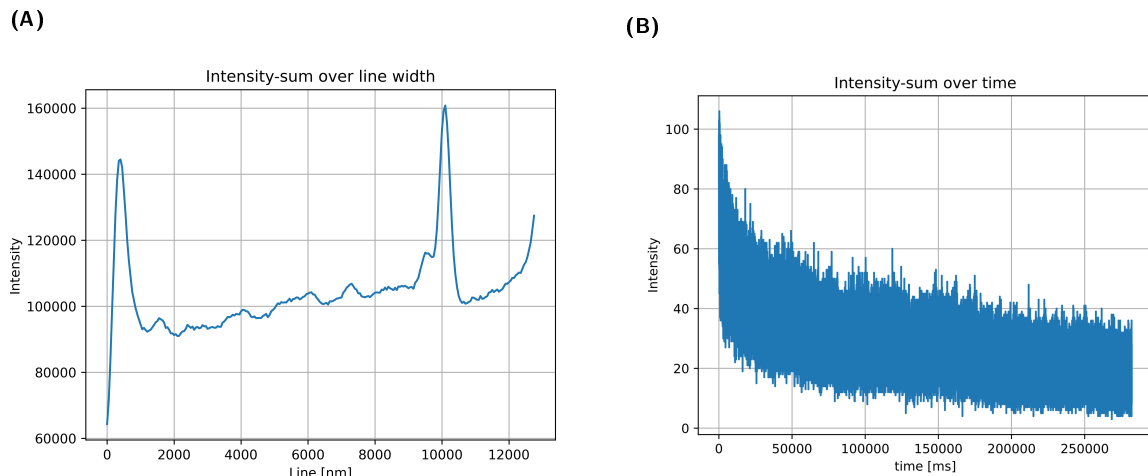


Figure 5.22.: Intensity-sum figures for the user to decide upon time and x boundaries in which the LS is to be analysed. (A) shows the pixel-intensity-sum plot over the line width of the LS (x-axis). (B) shows the pixel-intensity-sum plot over the time axis (y-axis) of the LS. In this case, the boundaries were set to 1000 nm to 9000 nm region in the x-direction in order to stay within that homogenous area. Everything from 50 000 ms onwards was used in the time direction, thus excluding the strong bleaching in the beginning.

the case can be found e.g. in figure D.7(14) for comparison. The AC curve fit results in a diffusion coefficient of $0.8 \mu\text{m}^2/\text{s}$ but the fitting (orange) is imprecise up to 50 ms. The Gaussian fit (orange) in (c) seems to capture the broadening of the underlying data (blue) nicely but gives no further information besides functioning as a visual control of the fitting quality. The fitting quality can also be shown by plotting the residuals of the fit as shown in figure 5.23D. The data shown here was normalized prior fitting, otherwise the residual values would have been too small to visualize together with the fit. The residuals (orange) fluctuate around zero, thus demonstrating that the fit captures the curve shape of the underlying data nicely. The resulting MSD plots are depicted in figure 5.24.

Looking at the τ -MSD plots in different τ -intervals allows to observe different properties of the diffusion process. The plot 5.24A shows the MSD values up to 1 s. As the binning is logarithmic, the dots are not evenly spaced in a linear scaled plot. The general MSD over τ seems to be roughly linear, showing a normal diffusion. Therefore, no diffusion barriers are evident in this sample. A counter example with clearly confined diffusion is shown in figure 5.25. The MSD plot depicted there plateaus at about $0.11 \mu\text{m}^2$.

To get the diffusion coefficient of the analysed process, the linear part for small τ values needs to be fitted. Here exemplarily shown for $\tau < 100$ ms. The fitting yields two parameters, subsequently used for further calculation: The y-axis intercept, $0.0445 \mu\text{m}^2$, and the slope of the linear fit, $1.019 \mu\text{m}^2/\text{s}$ for the example of normal diffusion in figure 5.24B. Based on the theoretical background described in section 3.6.4, the particle size is now derived by calculating the square root of the y-intercept, thus here the estimated size is 210 ± 20 nm. The

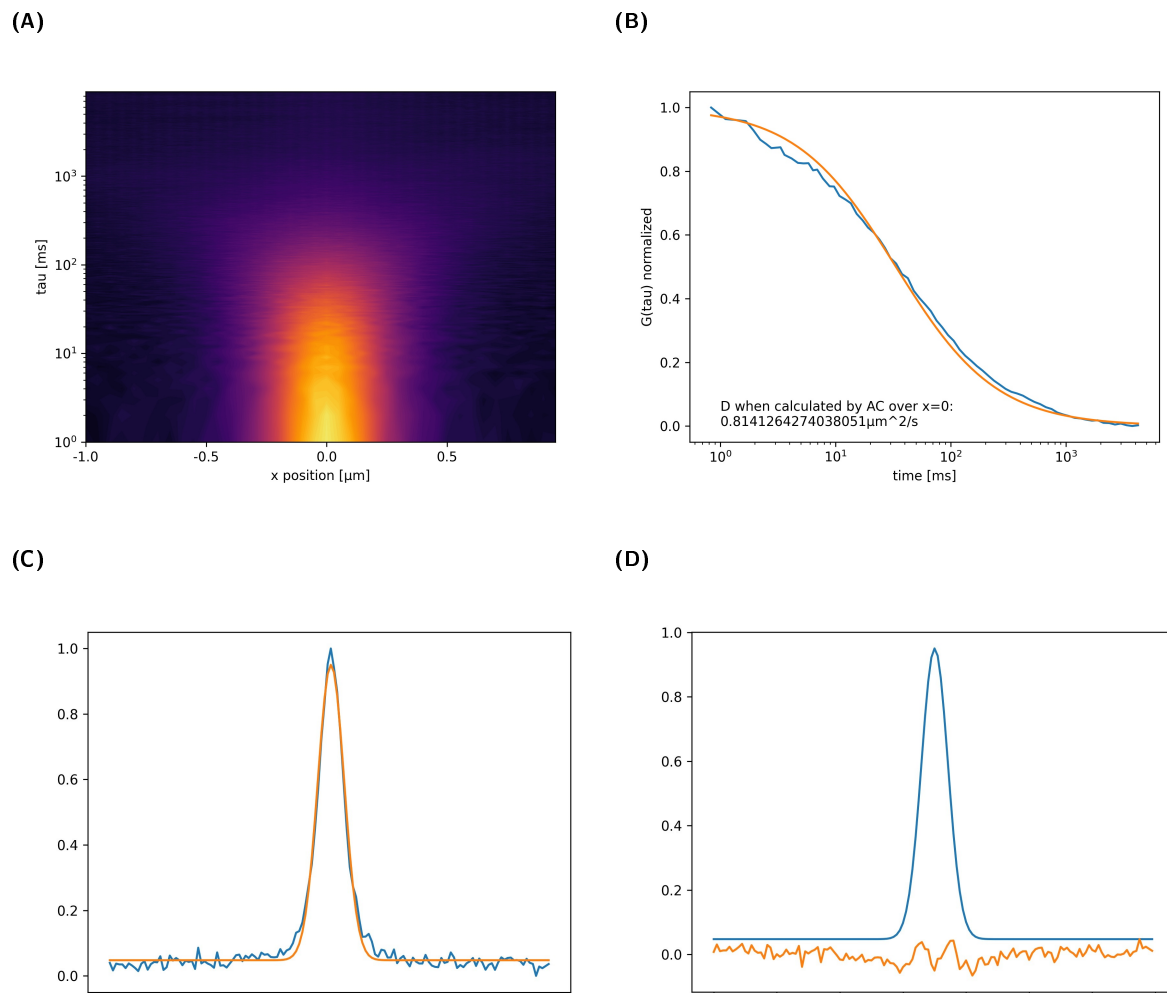


Figure 5.23.: Intermediate analysis results of the exemplary LS analysis for a non-stimulated M2R-Mut8. The STICS function (A) shows a clear plume, therefore the analysis picked up moving particles. (B) shows the AC curve fit which results in a diffusion coefficient of $0.8 \mu\text{m}^2/\text{s}$. (C) shows exemplary the Gaussian fit for the first τ -value ($\tau = 0.55 \text{ ms}$) (previously normalized for visualization). The fitting (orange) delineates the true data (blue) nicely. (D) shows the residuals of the fit (previously normalized for visualization, $\tau = 0.55 \text{ ms}$). The corresponding MSD plots are depicted in figure 5.24.

diffusion coefficient of this example is $0.255 \pm 0.002 \mu\text{m}^2/\text{s}$ when assuming a 2D diffusion as this is membrane diffusion (Applying equation 3.1 with $n=2$).

The confined diffusion example, figure 5.25B, on the other hand results in a diffusion coefficient of $0.114 \pm 0.003 \mu\text{m}^2/\text{s}$ and an apparent particle size of $220 \pm 20 \text{ nm}$. Therefore, there is a considerable cell to cell variability evident, as becomes clearer, the more samples are analysed.

This analysis workflow as described above is done for every individual LS of a certain condition. All heat maps of the non-stimulated M2R-Mut8-LSs are shown in figure D.7 of the appendix. This overview already offers some information. While many samples show clearly defined plumes and thus indicate that the individual experiments worked, there are also two general types of anomalies found in this data-set.

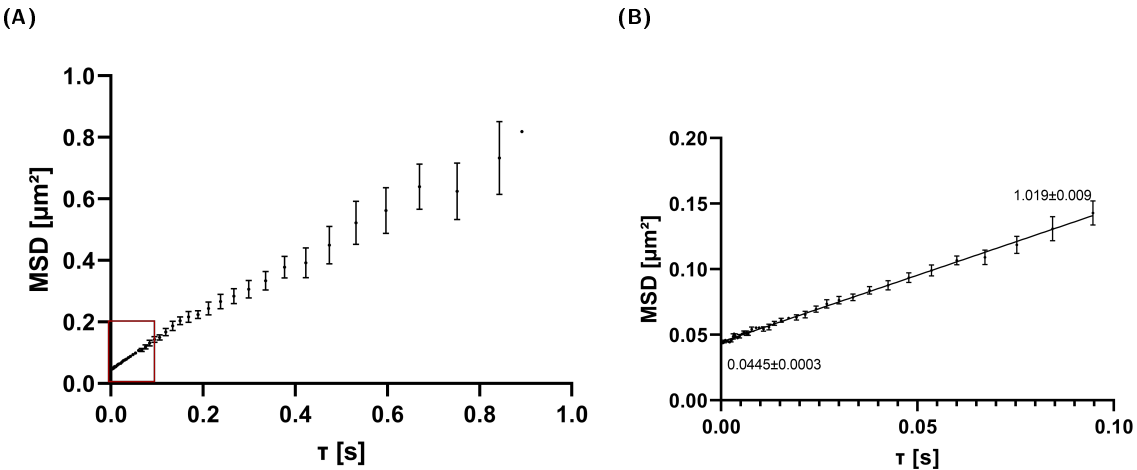


Figure 5.24.: The MSD-plots derived from the Gaussian fitting results of the STICS function shown in figure 5.23A. (A) shows the MSD values up to $\tau = 1$ s. It shows a normal diffusion, no clear confinement visible. (B) shows the MSD values up to $\tau = 0.1$ s, the area used for determining the diffusion coefficient by linear fitting (black line).

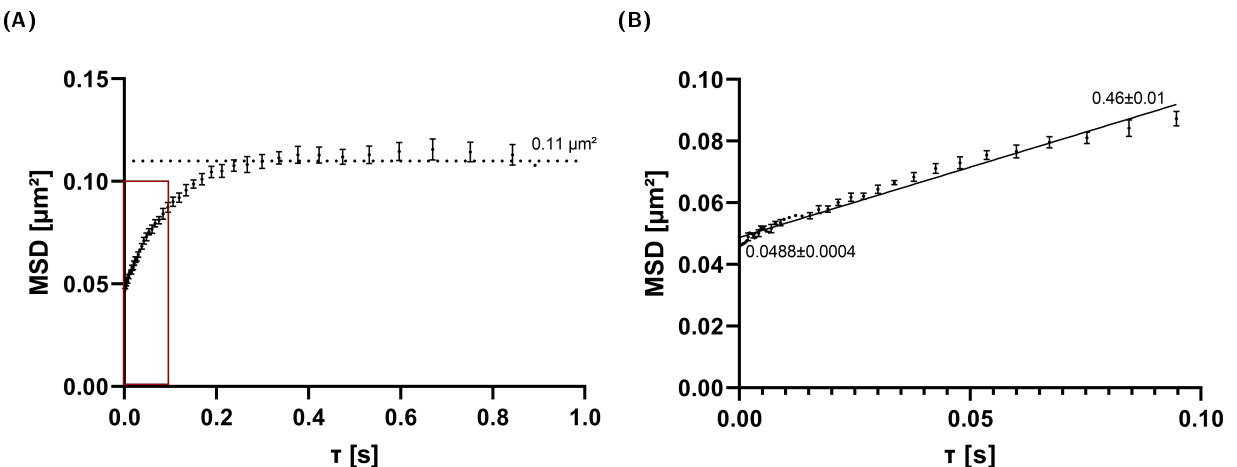


Figure 5.25.: The MSD-plots derived from the Gaussian fitting results of the STICS function shown in figure 5.23A. (A) shows the MSD values up to $\tau = 1$ s. It shows a normal diffusion, no clear confinement visible. (B) shows the MSD values up to $\tau = 0.1$ s, the area used for determining the diffusion coefficient by linear fitting (black line).

First, there are some heat maps that show none or at least not a very clearly defined plume like for example the plots 5, 8, 14 and 15 in figure D.7. Here, the analysis did not pick up any clear movement signal. One of the possible explanations is, that the sample was overcrowded. It is the intensity fluctuation (the change) that gets analysed with this approach. The amplitude of those fluctuations due to diffusion decreases if too many fluorescent particles are always present (to small a change if the signal is generally high).

Second, there are some samples that show a very sharp, thin and high peak at $x=0$ that does not fit to the general broadening of the plume. Examples can be found in the plots 4, 9 or 10

of D.7. Those correspond to samples that did not only harbour diffusing receptors but also a second subset of very slow moving particles for example due to stuck Cy3-labels/receptors.

Now there are two basic possibilities how to evaluate this collection of individual analysis outcomes. One could either analyse the individual LS and then compare the individual results or one can use the STICS matrices, average all of them for one experimental condition (e.g. all non-stimulated samples) and run the diffusion analysis on a averaged STICS plot.

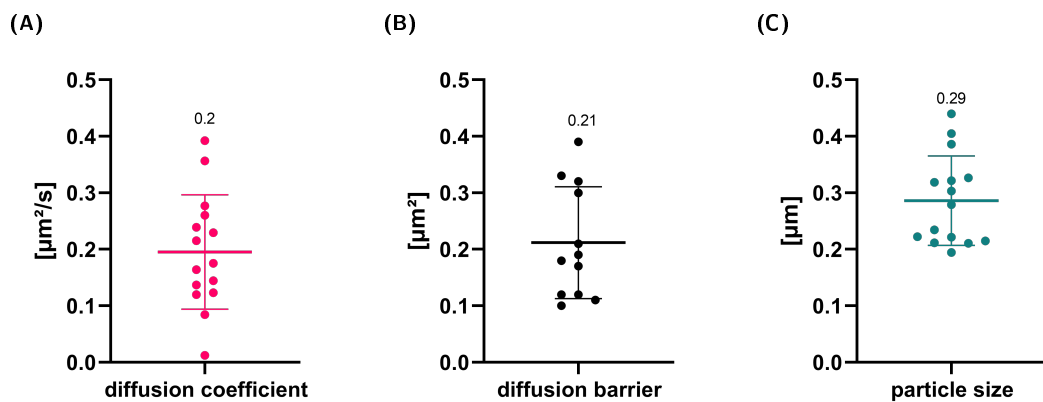


Figure 5.26.: Results of the individual LS analysis of the pre-selected non-stimulated M2R-Mut8 dataset ($n=16$). Results obtained from the Gaussian fitting derived MSD plots. (A) shows the scatter plot of the individual diffusion coefficients with a mean D of $0.2 \pm 0.1 \mu\text{m}^2/\text{s}$, (B) of the apparent diffusion barrier in the MSD plots up to 1 s with a mean diffusion barrier of $0.210 \pm 0.10 \mu\text{m}^2$ and (C) the apparent particle size with a mean of $290 \pm 80 \text{ nm}$.

Figure D.10 summarizes the individually analysed LS of non-stimulated M2R-Mut8 that did not display the anomalies discussed above (therefore from here on referred to as pre-selected). Of those 16 analysed LS, only three showed no clear confinement while all other samples levelled out to a clear plateau. The analysis outcomes of the individual samples is summarized in figure 5.26. The mean diffusion coefficient of the individual LSs (figure 5.26A) is $0.2 \pm 0.1 \mu\text{m}^2/\text{s}$. The mean apparent receptor size (particle size plus PSF) is $290 \pm 80 \text{ nm}$ and the mean confinement area of those samples showing a confinement ($n=13$) is $0.210 \pm 0.10 \mu\text{m}^2$. The high SDs corresponding to the also visually widely scattered data points in figure 5.26 clearly indicate a high cell to cell variability. Simply averaging the single cell result does not take the signal quality (definition of the plume) into account but instead weights all individual cell results equally.

Next, the individual non-stimulated M2R-Mut8 STICS function matrices were averaged and the averaged STICS function subsequently analysed as outlined in section 4.2.11.1. This averaged analysis is shown side-by-side for all LS of the non-stimulated data-set and for the pre-selected subset.

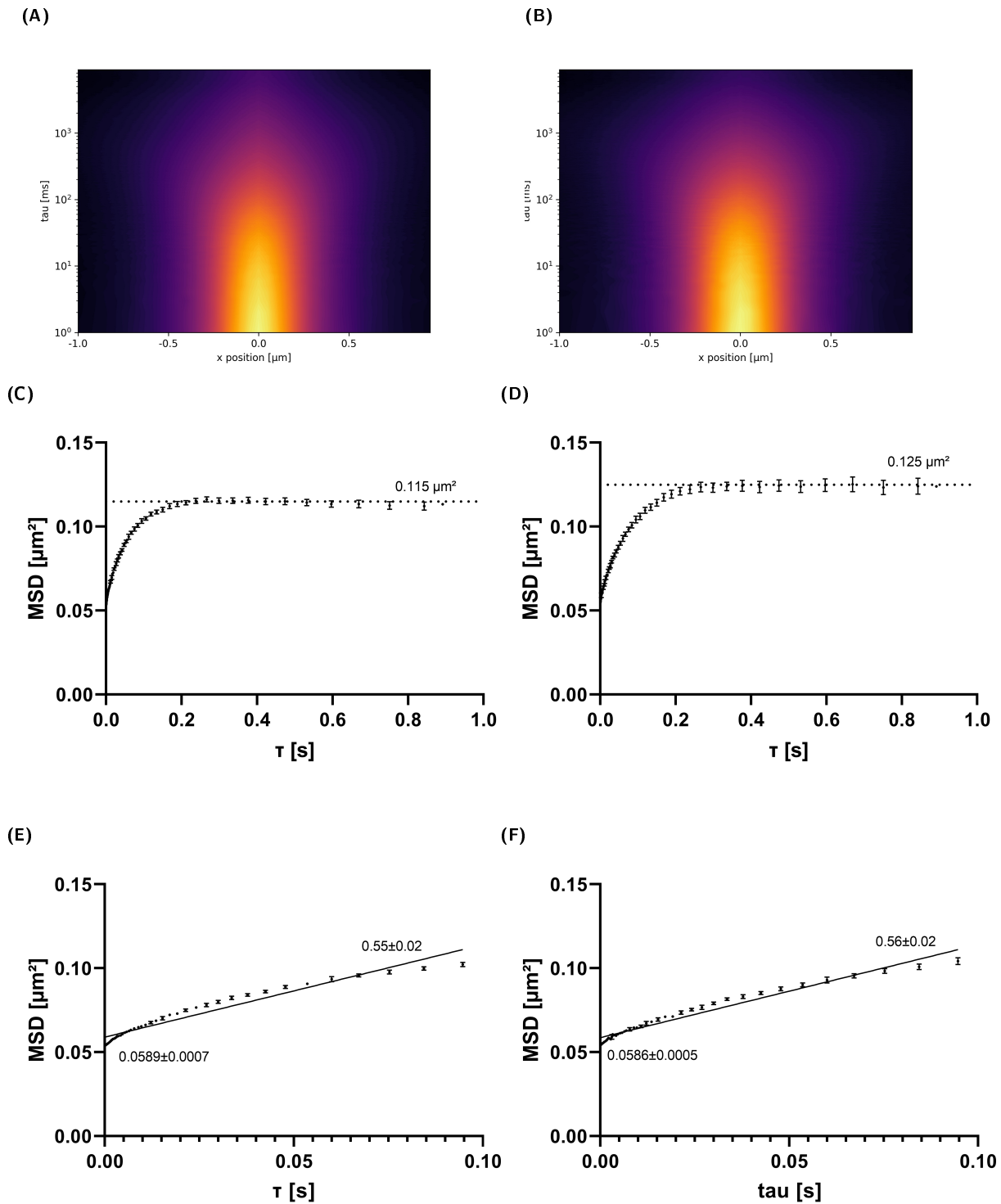


Figure 5.27.: Heat maps of the averaged STICS function matrices of (A) all non-stimulated M2R-Mut8 samples ($n=32$) or (B) the pre-selected subset ($n=32$). MSD plots of all non-stimulated M2R-Mut8 samples (left side) and the preselected subset (right side). (C) shows the MSD plot for $\tau < 1 \text{ s}$ of all non-stimulated M2R-Mut8 LSs ($n=32$). (D) shows the MSD plot for $\tau < 1 \text{ s}$ of the pre-selected non-stimulated M2R-Mut8 LSs ($n=16$). (E) shows the MSD plot for $\tau < 0.1 \text{ s}$ of all non-stimulated M2R-Mut8 LSs ($n=32$) and (F) shows the MSD plot for $\tau < 0.1 \text{ s}$ of the pre-selected non-stimulated M2R-Mut8 LSs ($n=16$).

Figure 5.27 shows the averaged STICS function plots for all non-stimulated LS (A) and the pre-selected data-set of the non-stimulated LS (B). Comparing them purely visually, the main difference is a slightly visible thin peak in (A) of a slowly-diffusing subset of particles as mentioned earlier. Otherwise the plumes look quite alike. This again stresses the difference between individual analysis and subsequent averaging (taking all STICS functions equally into account) to the STICS function averaging as performed here: even though the samples with the high background generally show a broader plume, they don't change the averaged plume too much as the amplitude of this STICS functions is small. Thus, when averaging over all STICS matrices, their influence is slight. This way, the STICS function averaging takes the data quality already into account without introducing a bias by selecting by hand.

The resulting MSD curves of the Gaussian fitting performed on those two averaged STICS function plots are shown in figure 5.27. The middle row gives the MSD plots up to $\tau = 1\text{ s}$. The plots differ slightly in the individual plateau height. The MSD plot of all LSs shows confinement at about $0.115\text{ }\mu\text{m}^2$ while the pre-selected subset levels out at about $0.125\text{ }\mu\text{m}^2$. The differences in the linear fits up to $\tau = 0.1\text{ s}$ are also minor. The fitting of all LS-averaged (E) results in a diffusion coefficient of $0.138 \pm 0.005\text{ }\mu\text{m}^2/\text{s}$ with a particle size of $240 \pm 30\text{ nm}$. Taking the pre-selected subset (F) results in a diffusion coefficient of $0.138 \pm 0.004\text{ }\mu\text{m}^2/\text{s}$ with a particle size of $240 \pm 20\text{ nm}$. Looking at the data points in (E) and (F), it is apparent, that the fitted region is not completely linear. Thus, decreasing the τ -values to only incorporate the truly linear region could be more precise. Still, the $\tau < 0.1\text{ s}$ region was chosen, in order to reliably compare the results to those yielded by Serfling, Seidel, Bock, *et al.*[10] on the diffusion behaviour of the very same receptor. The results shown in this chapter match those generated in [10], where M2Rs, bio-orthogonally labelled in different positions, were also investigated on their diffusion behaviour. They also used $\tau < 0.1\text{ s}$ for the MSD fit for D extraction, making these analysis very comparable. They observed a D of 0.11 to $0.13\text{ }\mu\text{m}^2/\text{s}$ and a intercept of 0.053 to $0.055\text{ }\mu\text{m}^2$ which translates to a apparent particle size of 230 to 235 nm .

5.5. Analysing the diffusion behaviour of the M2R-Mut8 upon receptor activation

All other data-sets were analysed by STICS function matrix averaging as shown in the previous section. For the comparison of these samples, all linear fits were performed for $\tau < 50$ ms in order to stay in the linear region in all cases. The corresponding STICS functions as well as the fits are summarized in figure E.14.

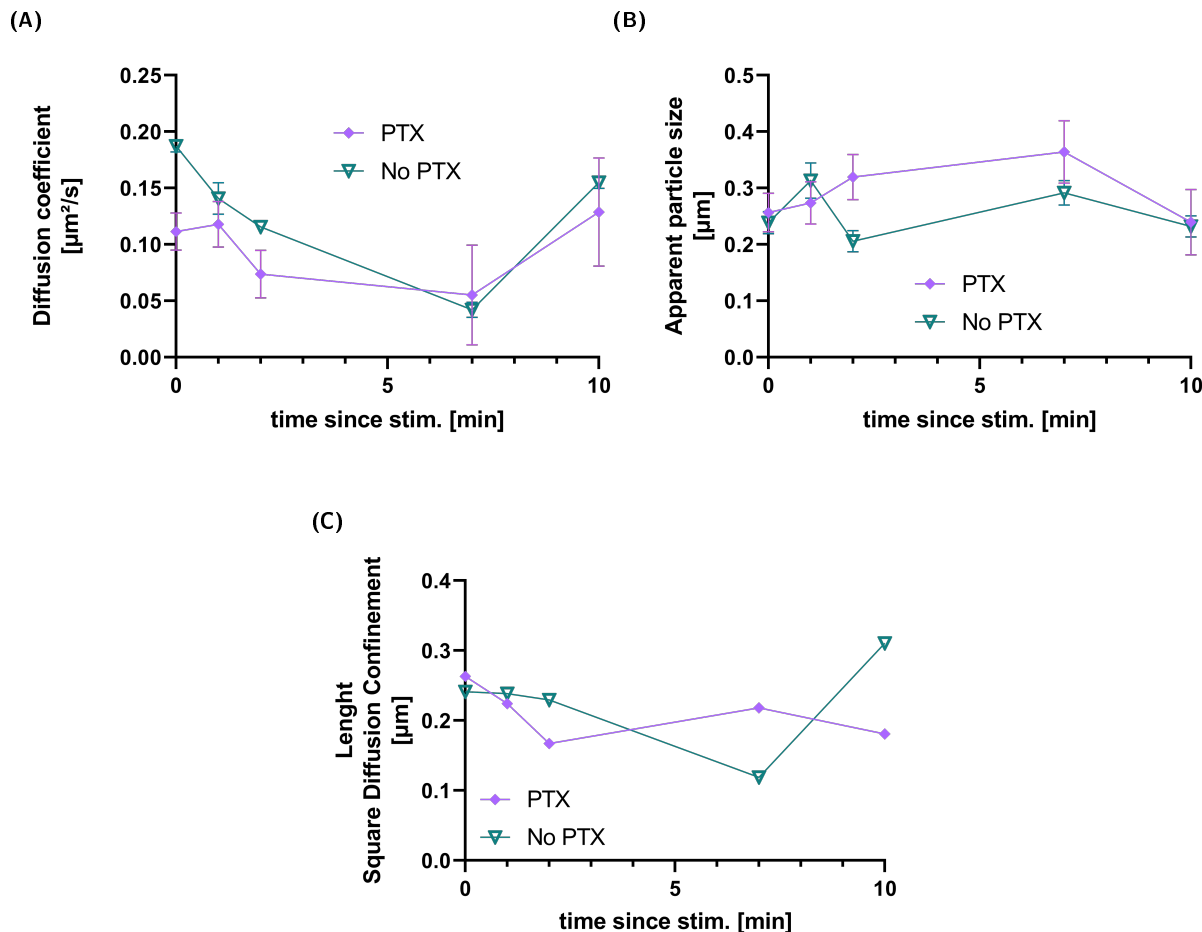


Figure 5.28.: Meta-Analysis of all performed M2R-Mut8 LS experiments. All results were extracted from the 50 ms linear fits of the MSD curves derived from the analysis of the averaged STICS function matrices as shown in figure E.14. (A) shows the diffusion coefficients of the averaged M2R-Mut8 non-stimulated samples (time point 0) or at different time points after ACh stimulation (green). The same set of experiments was performed with PTX pre-treated cells (purple). (B) shows the apparent particle sizes (particle size plus PSF) for both data-sets. (C) shows the calculated approximate length of the diffusion confinements derived from the individual plateau height of the averaged MSD-plots in figure E.14. Number of samples of the individual data-points: Untreated: nonstim = 39, 1min = 7, 2min = 10, 7min = 5, 10min = 11 PTX: nonstim = 19, 1min = 14, 2min = 4, 7min = 12, 10min = 4.

The readout diffusion coefficients, apparent particle sizes and the length of the square diffusion confinements are depicted in figure 5.28. The M2R-Mut8-experiments without pre-treatment

with PTX are delineated in green. Before stimulation (time point 0), the diffusion coefficient when extracted from the 50 ms fit, is at about $0.187 \pm 0.005 \mu\text{m}^2/\text{s}$. This already shows the dependence of the outcome on the chosen τ -range to fit. In the section above, when extracted from the 100 ms fit (in order to use the same settings as used in the reference paper), the diffusion coefficient of the very same STICS function matrix was $0.138 \pm 0.005 \mu\text{m}^2/\text{s}$. Therefore, it is important to decide on one τ interval for the fitting, which is then constantly used throughout the analysis, in order to allow for a comparison between the samples.

Looking at the D development over time after stimulation, the diffusion coefficient drops till seven minutes after stimulation to $0.042 \pm 0.007 \mu\text{m}^2/\text{s}$ but returns to the non-stimulated level after ten minutes ($0.155 \pm 0.005 \mu\text{m}^2/\text{s}$). The changes in the PTX pre-treated samples are smaller and show a higher SD. The diffusion coefficient starts from a lower level with $0.11 \pm 0.02 \mu\text{m}^2/\text{s}$ in the non-stimulated condition. The D value also drops in this case after stimulation, to $0.06 \pm 0.04 \mu\text{m}^2/\text{s}$ after seven minutes and rebounds to $0.13 \pm 0.05 \mu\text{m}^2/\text{s}$ after ten minutes. Thus, the diffusion coefficient of the PTX treated sample seems to be generally lower prior stimulation but levels out with the non-PTX-treated samples at 7 min after stimulation. Both data-sets show a recovery of the diffusion speed up to the unstimulated values ten minutes after stimulation.

The development of the apparent particle sizes upon stimulation is depicted in figure 5.28B. Again, in green the non-treated data-set and in purple the PTX pre-treated data-set. In both cases the starting apparent particle size lies at around 250 nm and seems to generally vary between 250 nm and 350 nm. This is consistent with the typical waist of a confocal microscope of about 250 nm. There is no clear pattern after stimulation that suggests some change in aggregation upon activation as both, the PTX pre-treated samples and the non-treated samples vary around the same values.

The M2R-Mut8 diffusion confinement (given in length of the square diffusion confinement) in the PTX-treated samples varies between 180 nm and 250 nm without a clear pattern. The non-PTX-treated data-set on the other hand shows a stable confinement of around 240 nm up to two minutes after stimulation, a slight decrease in the confinement length at seven minutes after stimulation to 220 nm length of the square diffusion confinement and again a lessening of the confinement at ten minutes after stimulation as the length of the square diffusion confinement increases to 310 nm.

The same analysis as performed in figure 5.28 was performed on the $\tau < 10$ ms region, in order to understand the diffusion behaviour of the M2R-Mut8 in more detail. The corresponding linear fits of the MSD-plots can be viewed in figure E.16. The analysis results are summed in figure 5.29. The SDs of the PTX treated dataset is much larger than in the previous figure,

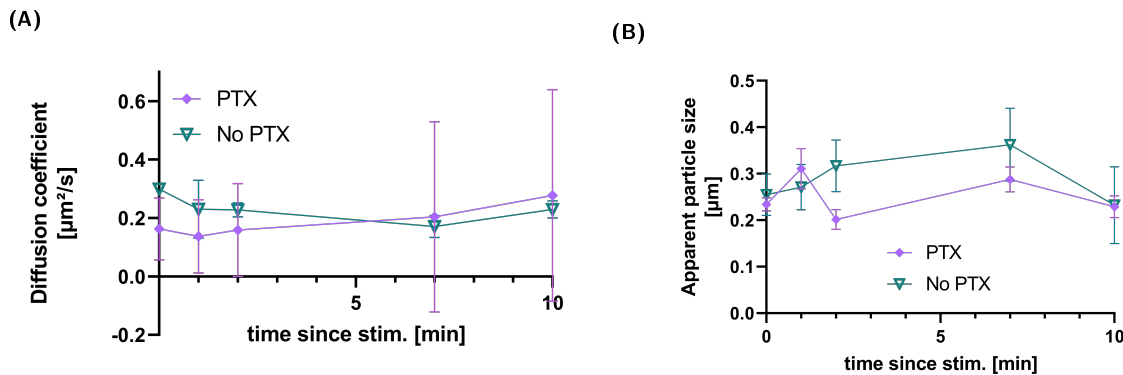


Figure 5.29.: Meta-Analysis of all performed M2R-Mut8 LS experiments from the 10 ms linear fits: MSD curves were derived from the analysis of the averaged STICS function matrices as shown in figure E.14. (A) shows the diffusion coefficients of the averaged M2R-Mut8 non-stimulated samples (time point 0) or at different time points after ACh stimulation (green). The same set of experiments was performed with PTX pre-treated cells (purple). (B) shows the apparent particle sizes for both data-sets. Number of samples of the individual data-points: Untreated: nonstim = 39, 1min = 7, 2min = 10, 7min = 5, 10min = 11 PTX: nonstim = 19, 1min = 14, 2min = 4, 7min = 12, 10min = 4.

thus reflecting the imprecise fittings in the 10ms range. However, the non-treated samples yield reliable fits with small SDs compared to the PTX samples. The diffusion in this τ -range is generally faster compared to the 50 ms data-set. The non-PTX-treated, non-stimulated M2R-Mut8 shows here for example a $D = 0.30 \pm 0.01 \mu\text{m}^2/\text{s}$ compared to the $0.187 \pm 0.005 \mu\text{m}^2/\text{s}$ of the 50 ms fit or the $0.138 \pm 0.005 \mu\text{m}^2/\text{s}$ of the 100 ms fit. The receptor diffusion is therefore increasing with decreasing τ -intervals. The up-shift of the diffusion coefficient 10 min after stimulation which was observed in both data-sets of the 50 ms fit is not evident in the 10 ms fit, indicating an effect coming into play only for larger areas. The higher diffusion speed of the non-PTX treated samples compared to the PTX-treated samples does still show with a $D = 0.30 \pm 0.01 \mu\text{m}^2/\text{s}$ for the non-treated samples compared to a $D = 0.2 \pm 0.1 \mu\text{m}^2/\text{s}$ for the PTX-treated samples. Also, the non-treated M2R-Mut8 still slows upon activation from $0.30 \pm 0.01 \mu\text{m}^2/\text{s}$ prior stimulation to $0.17 \pm 0.03 \mu\text{m}^2/\text{s}$ seven minutes after stimulation. All in all, the effects detected in this smaller analysis range (10 ms) are generally smaller but they support the observation of a PTX effect on the diffusion behaviour of the M2R-Mut8.

5.6. Analysing the diffusion behaviour with SMT

The diffusion behaviour of the M2R-Mut8 upon stimulation was also checked by single molecule tracking. The acquisition was started, the ACh added by hand-addition and the time point noted. The tracking movie of about three minutes was cut into half a minute batches after stimulation. Subsequently, the MSD plots were individually extracted from those 30 s batches. This made it possible to check if there is a change over time in the diffusion behaviour by SMT.

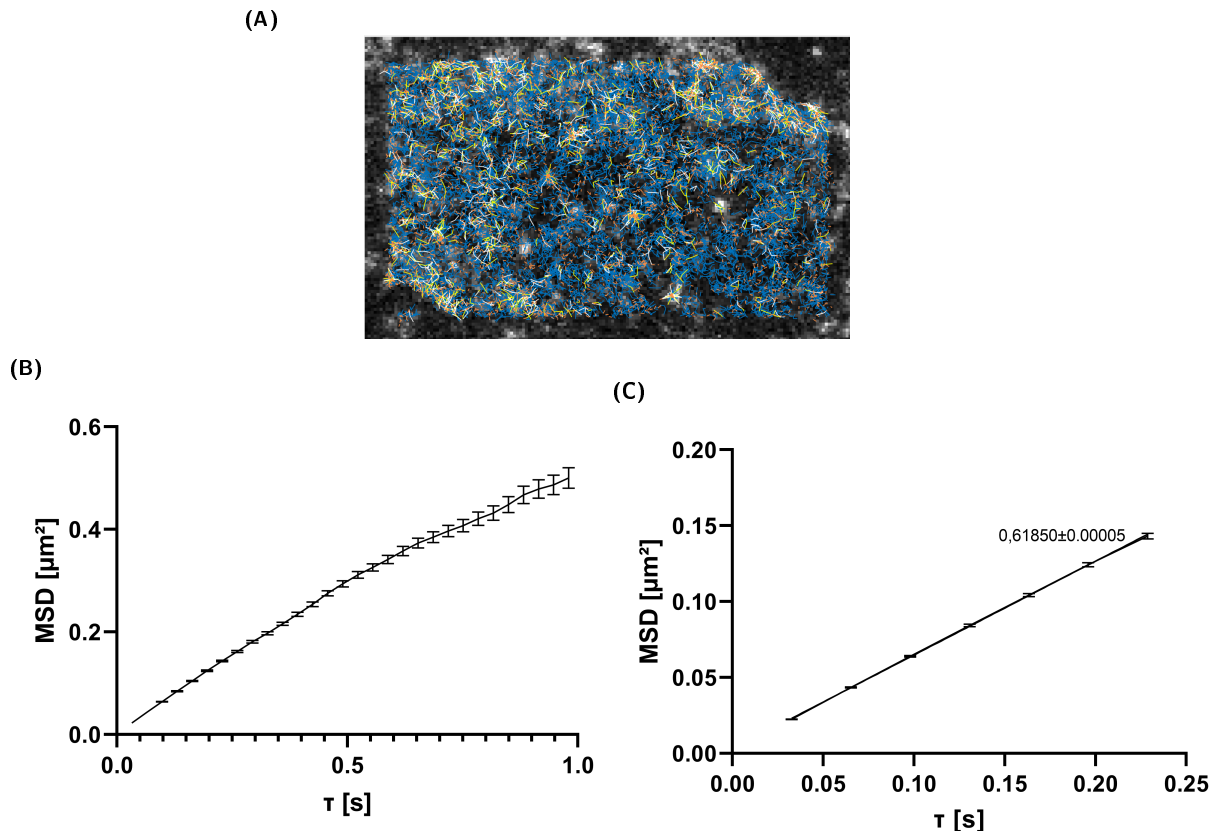


Figure 5.30.: Exemplary data-extraction from one SMT experiment. (A) shows the extracted traces of a 30 s time interval. These are used to calculate the MSD-values over τ as described in section 4.2.11.2. (B) shows the resulting MSD plot for $\tau < 1$ s. The τ interval $\tau < 0.25$ s (C) was subsequently used for linear fitting and D value extraction.

An exemplary cell picture with the overlaid traces of a 30 s tracing interval is depicted in figure 5.30A. Those traces were then used to extract to MSD values depicted in figure 5.30B. In this case, it is a non-confined diffusion with a D of $0.155 \pm 0.000 \mu\text{m}^2/\text{s}$. A counterexample of a region of interest (ROI) with confined diffusion can be viewed in figure E.18 of the appendix.

The extracted diffusion coefficients from the linear fits of those MSD plots are delineated in figure 5.31A. Each individual colour/shape corresponds to one analysed cell ROI on individual cover slips as exemplified above. The D values of different ROIs vary between $0.06 \mu\text{m}^2/\text{s}$

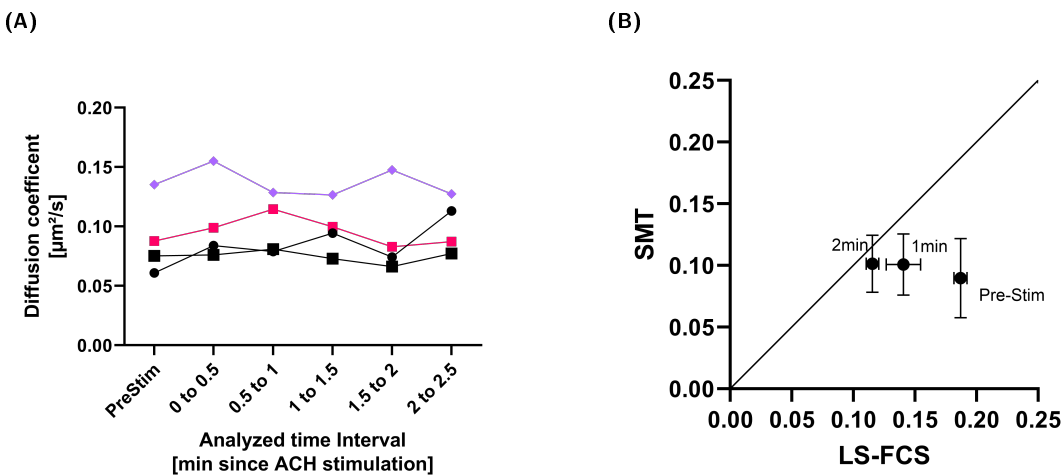


Figure 5.31.: (A) shows the diffusion coefficient results of the SMT experiments of M2R-Mut8 in four individual cells. Analysis intervals of 30 s after stimulation. The SD is too small to be plotted (All SD values lie between 0.00001 and $0.0005 \mu\text{m}^2/\text{s}$). (B) compares those diffusion coefficients to the D-values extracted at the same time points after stimulation from the LS-FCS experiment as shown above.

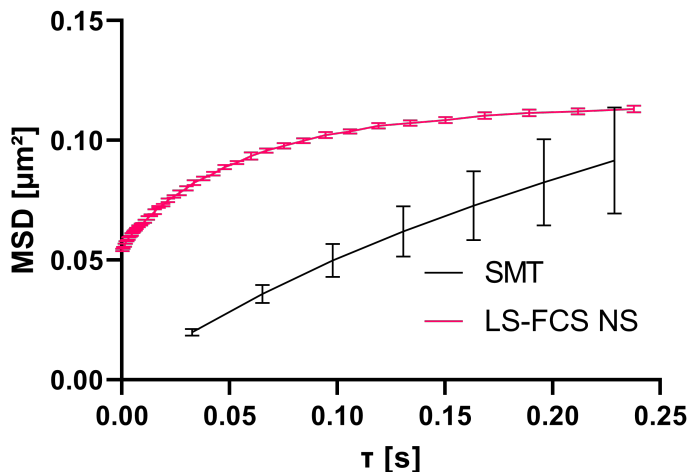


Figure 5.32.: Visualizing the difference between MSD-values extracted by SMT compared to LS-FCS. The MSD-plot from the non-stimulated M2R-Mut8 (same data-set as shown above, $n=39$) is delineated in pink while the MSD-plot from the SMT-experiment is delineated in black ($n=4$).

and $0.15 \mu\text{m}^2/\text{s}$ but stay almost constant within one cell throughout the measurement. Now, reconsidering the results from the LS analysis, if there is a effect up to 2.5 minutes, it should be a drop of the diffusion coefficient upon stimulation. In fact the progression of the D values after stimulation in figure 5.31A show no change upon stimulation. This difference in analysis outcome becomes visible when directly comparing the D-values of the same time-points after stimulation of both methods as done in figure 5.31B. The line indicates an exact accordance of the values. The SMT-derived diffusion coefficients strongly diverge from the LS-FCS-derived values for the non-stimulated samples but seem to be more in agreement for the 2 min time point.

A possible reason why the SMT-analysis does not show the differences detected by LS-FCS may lay in the methods themselves. The MSD-curves of the SMT-experiment and of the non-PTX-treated LS-FCS data-set are shown in figure 5.32 (up to $\tau = 0.25$ s). The LS-FCS MSD-curve (pink) shows a clear confinement already in this τ interval and is very well defined by finely interspaced data points. The SMT-derived MSD-curve (black) on the other hand offers in this τ interval only seven data-points due to the longer acquisition interval. The sampling rate in the LS-FCS experiments is 1800 Hz (a line every 0.55 ms). The sampling rate of the SMT experiments is about 30 Hz (a picture every 30 ms). This makes the SMT less sensitive for the detection of subtle changes in the diffusion behaviour as seen before in the FCS analysis.

6. Discussion

The aim of this thesis was to investigate the diffusion behaviour of a prototypical G_i-coupling receptor under conditions near to a native system with FCS. Therefore, the labeling needed to exercise as little influence on the receptor properties as possible. We chose to incorporate a non-canonical amino acid for bioorthogonal labeling as the preferred method over, for example, the addition of a fluorescent protein or alike. Additionally, the goal was to develop an open-source, freely downloadable script for LS analysis based on Python 3. This script needed to be tested on functionality by applying it to data of known outcome. It was afterwards used for analysis of the receptor diffusion behaviour. Thus, the discussion is also divided into a first, methodological discussion concerned with the development of the Python script and a second part, concerned with the insights into the M2R diffusion dynamics.

6.1. A functional Python script for LS-FCS analysis was developed

The first implementation of the one dimensional AC calculation via interlaced FOR-loops showed the limitations of such a sequential procedure as the calculation time with >10h exceeded any reasonable limit for a everyday analysis. It could have been further optimized for example by optimizing the parallel computing with Dask [87] but this was not followed up as using Fourier transformations reduced the needed pure calculation time to seconds or minutes, depending on the size of the input data. Thus, showing again the value of the FFT algorithms [72], [88].

The time-intense step now is the actual visualization of the heat map as it takes the non-binned STICS matrix and generates a freely scalable vector-graphic. This can take up to two minutes, depending on the used bin size. Bins of 10 seconds were used in this thesis as they encompass the region of interest for receptor diffusion (they need 20 to 30 seconds to get visualized). To speed this up, one could consider to set a fixed resolution (rasterization [89]) or pre-binning of the matrix prior plotting.

Another time costly point is the Gaussian fitting to the individual τ -rows of the STICS matrix. A parallelization might also improve the performance here but is also highly depended on the

individual hardware used for the analysis (RAM and CPU).

In general, we showed that the Python script generates analysis results comparable to the benchmark analysis by a script in Igor Pro (WaveMetrics, [90]) which is typically used in the research group 'AG Receptor signaling'. This is shown in table 5.2. The differences that do exists are most likely due to differences in the analysis procedure of the scripts. The Python script, for example, was designed to cut the line scan into pieces depending on the user-chosen max τ . It averages the STICS matrix from those while not binning over τ prior fitting. The Igor version instead calculates the STICS directly over the full length LS (not over individual pieces) but then bins the resultant matrix into 64 log-bins. It also encompasses data corrections for bleaching and alike that are not yet realized in the Python program. Here, the only data-correction made is the area selection by the user prior analysis. Thus, the exclusion of very strong disturbances like the initial bleaching or signal inhomogeneities due to, for example, membrane-folds. Additionally, the method chosen to import the LS may influence the analysis outcome.

The big advantage in using Python instead of Igor is, that Python is cost-free. No deeper knowledge of the Python programming language is needed for simply running the script, as it only requires very few user inputs that correspond to the acquisition settings. These are outlined in section F of the appendix. Furthermore, the use of the freeware Python makes the analysis script amenable to further developments and contributions by the wider community.

Another interesting point lies in the comparison of the two different calculation strategies of the diffusion coefficient implemented within the Python code. Either by fitting a diffusion model (2D or 3D) to the autocorrelation curve, or by Gaussian fitting at the individual τ -values. The big advantage of the first method is, that it needs only one fit and is therefore very fast to directly extract D. Its advantage is at the same time also its biggest disadvantage. This method of calculation relies on one single fit along the τ -axis at $x=0$. A one dimensional fit is intrinsically less robust than a sequence of one dimensional fits. This was also observed within this thesis. The Gaussian fitting loops over all x-values for every individual τ -value of the used τ -interval. This results in about 1800 individual fits for the typically used τ -interval of $\tau < 1\text{ s}$, making the end result very robust.

Another advantage of the Gaussian fitting above the fitting of a diffusion model is, that it does not need as much user input prior fitting. The AC-curve fitting needs the wavelength specific PSF values ω_0 and ω_z determined before running the analysis.

6.2. A data-preselection was shown to be unnecessary and the analysis could thus be performed user-bias free

Several line scans showed no or very small and noisy fluctuations in their STICS matrices as is shown in figure D.7. There are several possible explanations for this. A too low receptor expression or labeling can be excluded, as this is checked by the workflow of choosing a line of acquisition. Furthermore, the receptor diffusion coefficient generally fluctuates in a range picked up by the analysis setup [10], so this is also no explanation. The most likely explanation is the earlier mentioned overcrowding of the sample. If the signal generally is too high, the intensity fluctuations induced by the diffusion in turn is too small to be picked up [91][64]. This suggests, that we are already working at the upper limit of the concentration range suitable for this method. The expression could be optimized by decreasing the expression time (for these experiments set to over night expression).

Still, the presence of these STICS matrices with low signals or anomalies does not generally impede the analysis. As we showed, it makes no significant difference in the analysis outcome if the STICS matrices are preselected to exclude samples with low signals or highly confined, slow moving sub-populations or not. This is grounded in the averaging procedure done in the script. Those STICS matrices with a noisy signal and small fluctuation-to-background differences will have a small effect on the overall averaged STICS plot compared to the well defined plume of a strong fluctuation signal. Thus, the individual LS are weighted in their influence on the analysis outcome based on their signal to noise ratio. Therefore, the selection by hand that could possibly induce a human bias can be skipped. This makes the approach neutral to outcome expectations that may influence the selection.

6.3. The SMT does not record a change in diffusion behaviour upon receptor activation

The same M2R-Mut8 used for the LS experiments was also checked with SMT under stimulation. Interestingly, the diffusion coefficients derived from the SMT do fall in the very same range as they vary also in the FCS experiments but fail to register any change upon stimulation. Instead, the D of an individual cell always stays the same, also after ligand addition. As pointed out in the Results section, this might be explained by the different frame rates of the methods. The LS-FCS acquires a line every 0.55 ms for the settings used in this thesis compared to one picture every 30 ms for the SMT. As the M2R-Mut8 showed confinement already

within the $\tau < 100$ ms range, the SMT is unable to actually register the diffusion coefficients in the unconfined, linear part of the MSD as shown in figure 5.32. Instead, it offers the diffusion coefficients in a lower resolution and thus less sensitive to subtle effects in the small τ -intervals.

6.4. The M2R was successfully expressed and labelled at amino acid position 8

It was shown by the ELISA assay, that the mutant can be expressed in the chosen system but in significantly smaller amounts than the wild-type receptor. This is actually beneficial for two reasons. The extremely high overexpression as achieved by the wt M2R versions is not very akin to the endogenous situation. GPCRs in general are mostly quite lowly expressed with 10^3 to 10^6 copies per cell [50] but specific in their expression patterns. The M2R in particular shows a moderate but very specific expression pattern in the nervous system but for example a high expression in the heart muscle [92]. As the number of the GPCRs is in a balance to the correspondent interaction partners like G proteins, an extreme overexpression does not replicate the natural situation in the cell but is instead a highly artificial system.

The second upside of this significantly lower expression compared to the wild-type is more of an experimental consideration. As pointed out in the Introduction, the fluctuation analysis via FCS is sensitive to the particle concentration [91]. The fluctuations due to receptor movement might get lost to the analysis if the general signal is too high. In this case, the fluctuations are too small in comparison to get differentiated from the background signal[64] as pointed out above. Thus, the important point is not to yield a very strong mutant expression but to stay in the applicable concentration range for FCS experiments and being able to specifically label those membrane receptors.

The last point was also demonstrated by staining the EGFP-tagged version of the M2R-Mut8 additionally with the Cy3. Only cells that really expressed the full length receptor (as the EGFP is attached at the C-terminus) and also showed clear Cy3-staining showed yellow stained membranes as the red and green coloured signals overlap (figure 5.4).

As labeling strategies can have a significant impact on the receptor functionality [9][8], [10], the mutant needed to be tested for its ability to induce downstream signaling upon activation. The EKAR-assay [83] showed clear signaling in the wt controls and no signal in the EKAR-only transfected control. Thus, it worked as expected to indicate M2R downstream signaling. However, considerable addition effects disturbed the fluorescence intensity signals. To avoid these, it might be advantageous to shift to a perfusion system for the ligand addition. A perfusion system allows cell specific stimulation with minimal liquid perturbation.

The M2R-Mut8 showed a generally lower sensor expression compared to the wild type sam-

6.5. The M2R-Mut8 shows clear compartmentalization and a considerable cell-to-cell variability

ples. This is not unexpected as these cells did not only receive two different plasmid constructs taxing on their protein synthesis system but three, as they also got the bioorthogonal system to express. This was also evident in the exemplary pictures of the three different acquisition channels, visualizing the expression of the receptor (Cy3) and of the sensor (CFP and YFP) (figure 5.10). The cells showing a high membrane signal in the Cy3-channel were those with a rather low sensor signal compared to their neighbour-cells. However, this lower expression also resulted in lower mean fluorescence intensities and thus in a noisier signal in the functionality assay (Figure 5.11) compared to the wt samples. This could possibly be optimized further by trying additional different plasmid concentration ratios. One could also consider using one of the improved EKAR versions, e.g. EKAR-TTV as it has a higher dynamic range [93] and thus should give a clearer signal compared to the background fluctuations.

Still, the mutant was shown to be sufficiently expressed, specifically labelled and functional. Therefore, it was deemed usable for the subsequent diffusion analysis.

6.5. The M2R-Mut8 shows clear compartmentalization and a considerable cell-to-cell variability

The single LS analysis done for the non-stimulated samples generated some interesting insides. First, there is a considerable cell-to-cell variability , as visualized in the scatter plots in figure 5.26. Second, almost all LS (except two) showed a clear confinement of the receptor, indicating a strong compartmentalization, also in the inactive state. The localization of the receptor within micro-domains does effect the signalling as pointed out in [29]. The M2R was e.g. shown to be strongly regulated upon ACh stimulation by endocytosis in neurons [94], [95]. It was reported to be able to adapt any oligomeric state between monomeric and tetrameric [40]–[42]. Thus, it was interesting to see if the confinement or particle size of the M2R-Mut8 shows any dependence to the ACh stimulation.

The particle size varies between 250 nm and 350 nm (figure 5.28B) without any obvious dependence on the ACh stimulation. The non-PTX-treated receptor seems to show a stable or slightly enhancing confinement up to seven minutes that is lessened at ten minutes. Still, this variations are small and do not indicate receptor recruitment into clathrin coated pits upon stimulation as might have been expected due to the receptor internalization pathway, as the M2R was shown to undergo clathrin dependent endocytosis [95], [96].

The next step here would be to check if the M2R-Mut8 does internalize upon stimulation. This could, for example, be done by confocal time course imaging, capturing the receptor in the membrane every few minutes up to 30 minutes or an hour after stimulation. The bioorthogonal

labelled M2R (but labelled in a different position) was shown to internalize after one hour by Serfling, Seidel, Bock, *et al.* [10], and we relied on these findings in this thesis.

6.6. The diffusion behaviour of the M2R-Mut8 might support the hypothesis of G protein pre-coupling

Starting by looking at the diffusion coefficients prior stimulation, the D values of the untreated samples show a considerable faster diffusion with a D of around $0.187 \mu\text{m}^2/\text{s}$ compared to the PTX-treated samples with a D of about $0.111 \mu\text{m}^2/\text{s}$ in the 50 ms fits. This seems to fit nicely to the observations made by Yanagawa, Hiroshima, Togashi, *et al.*[37], which suggest that the receptor could show a pre-coupling to the G-protein which in turn might lead to a higher diffusion coefficient when compared to the uncoupled receptor. Counter-intuitively, G protein coupling leads to higher diffusion rates. The receptor in the data-set that is pretreated with PTX should be unable to pre-couple with the G-protein and this could explain the lower diffusion coefficient. The diffusion coefficient of the non-PTX treated data-set decreases upon stimulation till it reaches the level of the PTX treated data-set at seven minutes. This could be explained if the M2R activation triggers the release of the G protein and thus, decreases the fast moving receptor fraction. The diffusion coefficient increases again in both cases after ten minutes stimulation. Still, when looking at the 10 ms fits, this effect is gone. Therefore, the increase in D after ten minutes stimulation does not show in small scale diffusion. The difference in diffusion speed prior stimulation between PTX-treated and untreated samples is also confirmed in the 10 ms fitting of the MSD.

An explanation for the difference in the diffusion coefficients at ten minutes post stimulation may be found in the internalization process [94], [95]. If the activated receptors get recruited into internalization complexes, this might leave only the non-activated receptors freely diffusing in the membrane while the activated receptors are confined. Thus, it would make sense that the increase of the diffusion speed after ten minutes is not visible in the small-scale diffusion.

All in all this thesis provides a tool for LS diffusion analysis within an open-source and freely adaptable software. Additionally, a M2R-Mut8 mutant has been generated and shown to be able to induce the downstream signalling cascade upon activation. The diffusion behaviour analysis of the M2R-Mut8 opens several questions. The FCS analysis might suggest an interesting effect of the G-protein on the diffusion behaviour but additional experiments are needed before one could draw any clear conclusions on this.

7. Outlook

The next steps to be done can be classified in two categories: First on the biological side concerning the actual diffusion behaviour of the M2R-Mut8 and second the further development and improvement of the Python scripts designed within this thesis.

On a programming side, there are two main things to do next. First, there is now a Graphical User Interface (GUI) under construction using Qt for Python (PyQt). This will enable an intuitive use of the program without the need for a command line dialogues or code modifications by the user. The GUI will set the ground for a good, user-friendly application that can be subsequently optimized in its functionalities.

The first additional functionality to be included is a MSD curve analysis within the Python environment. So far, the steps following the MSD curve extraction are performed in GraphPad Prism. The user needs to be able to individually set the boundaries for the linear fitting and thus, needs to be able to decide this upon seeing the MSD curve. Therefore, a user dialogue as done for the setting of the LS boundaries is needed. Also, this analysis could be extended to finer parameters like the confinement strength and micro- and macro-diffusivity as shown in [16]. However, doing so would again necessitate thorough testing and verification of the reliability of those calculations within the code.

An interesting point related to the receptor functionality would be to investigate qualitatively if the M2R-Mut8 does get internalized after stimulation with ACh by confocal time course imaging. The G-protein pre-coupling idea to explain the diffusion behaviour of the M2R-Mut8 could be proven or falsified by further experiments using a co-expression of the G-protein and the receptor. When keeping the pre-coupling idea in mind, an overexpression of the G protein should increase the fast moving receptor fraction, also after stimulation. Another very convenient experiment, in terms of observing unaltered diffusion behaviours, would be a dual-bioorthogonal labeling as is discussed in [97] to individually minimally label both proteins under investigation. The co-localization times could then be investigated either by SMT or for example dual-colour fluorescence cross-correlation spectroscopy [98]. However, this would require intracellular labeling which is challenging [99].

8. Acknowledgements

First, I would like to thank Prof. Dr. Paolo Annibale and Prof. Dr. Andreas Bock for giving me the opportunity to work in their research group 'AG Receptor Signaling'. All the people in the group share a true passion for science and created a collaborative and supportive working environment that made my year of delving into GPCR research not only instructive but also truly enjoyable.

Also, I would like to thank Prof. Dr. Jens Kurreck for agreeing to be the first Examiner and for his support throughout this thesis.

I especially thank Prof. Dr. Paolo Annibale for supervising me and examining this thesis. You gave me all the guidance I needed to come from zero knowledge about FCS to build my own little analysis script. The way there was quite long and winding but you always managed to point me back on track when I wondered off while still letting me figuring it out on my own.

My thanks also belong to Prof. Dr. Andreas Bock who mainly supervised me in the first half of my internship and on who's guidance and open ears I could rely on the whole time. I am looking forward to continue learning in your lab.

Many many thanks go out to all the other members of the lab group. I have peppered everyone of you with questions at some point and you always take the time to help each other grow and share your knowledge freely. That is worth a lot! I will also dearly miss the tea sessions and good talks with all of you!

Appendix

A. Expression and functionality of the M2R-Amber-mutant

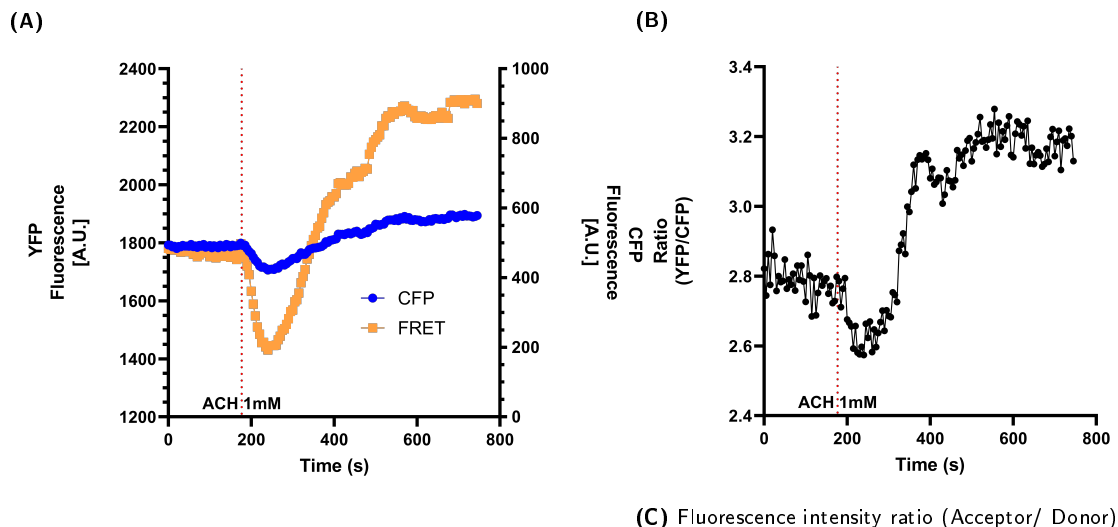


Figure A.1.: Exemplary trace FRET-change measurement: M2Rwt-extracellular signal-regulated kinase activity reporter (EKAR) co-transfection. (A) individual fluorescence intensity over time for the donor- (CFP) and the acceptor-fluorophore (YFP). (B) Acceptor/Donor ratio.

B. Developing a Python3 script for line-scan analysis

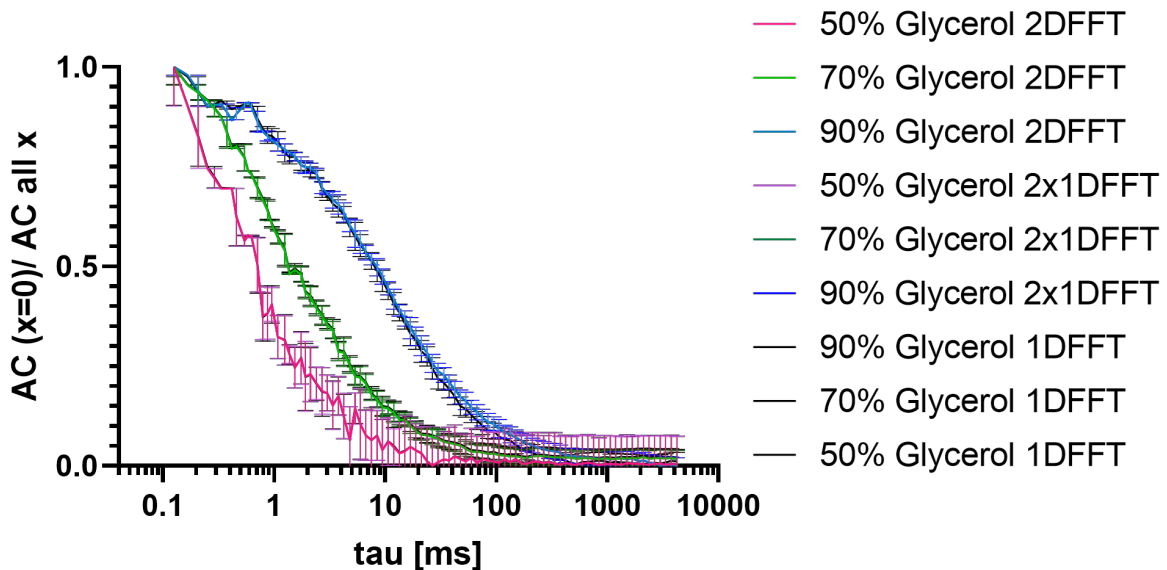


Figure B.2.: Normalized auto-correlation curve over τ calculated by the three different calculation methods: only over τ (1DFFT), over τ and subsequently Δx (2x1DFFT) and a two dimensional FFT (2DFFT). The curves overlap almost perfectly.

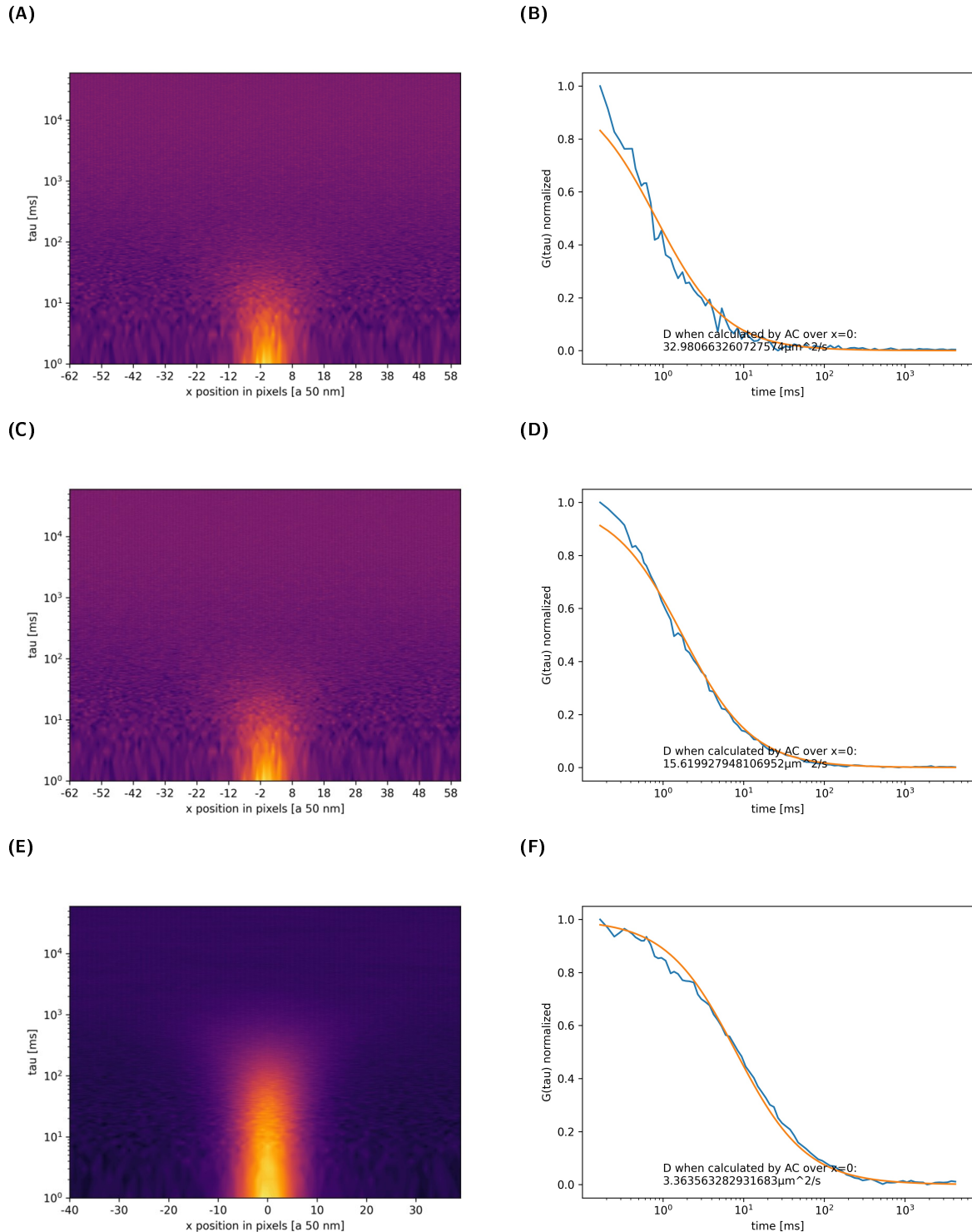


Figure B.3.: STICS function heat maps (left-hand) for the different glycerol conditions and the corresponding AC curves fitted to a 3D diffusion model (right-hand). (A) and (B) correspond to the 50% glycerol sample, (C) and (D) to the 70% glycerol sample and lastly (E) and (F) correspond to the 90% glycerol sample.

C. Verifying the results of the Python-implemented line-scan analysis

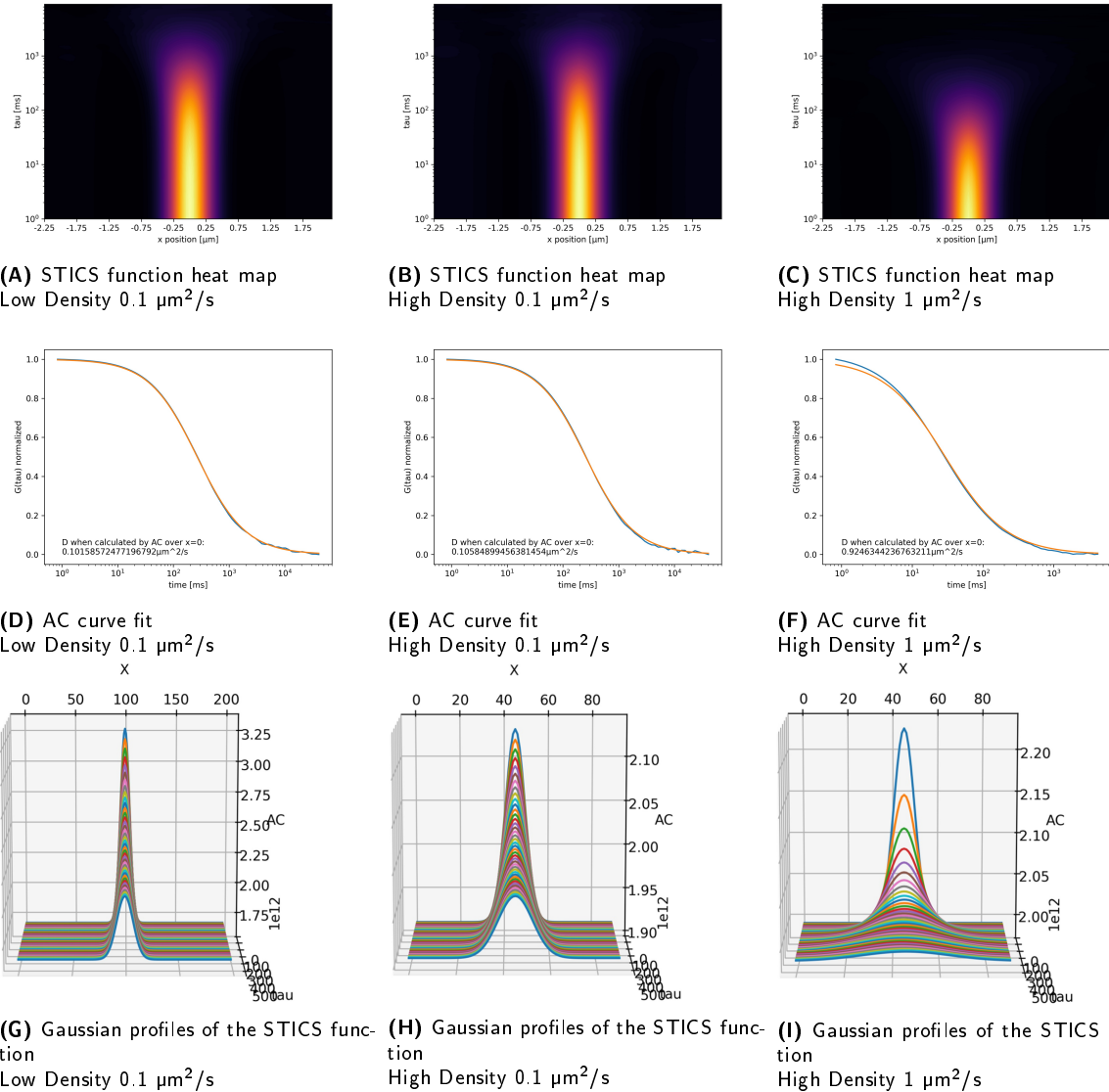


Figure C.4.: Closer look at the STICS function of the three different test data sets. Differing in particle density and diffusion speed. The upper row shows the STICS function results as heat map, giving a first impression of the diffusive behaviour (broadening of the plum over τ). The second row shows the AC curves in blue and the fits in orange. This corresponds a cut through the heat map along the τ axis in position $x=0$. The individual values of the STICS function matrix, made visible by the colour change in the upper row, can also be visualized as Gaussian fits at the individual τ values, thus uncovering the rising σ /amplitude shift with rising τ .

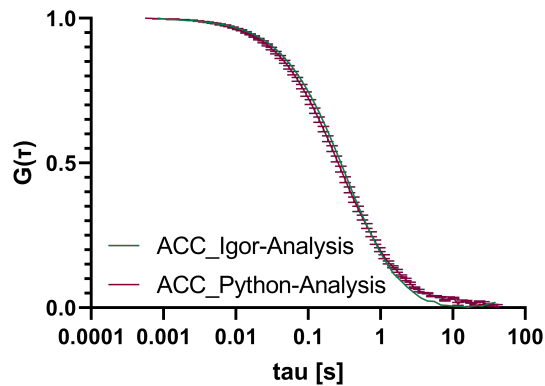


Figure C.6.: Exemplary cell used for LS, Cy3-channel.

From left to right: First a suitably well labelled cell is chosen, subsequently focused on its base membrane, and set to a 50nm/pixel 256X256 image size.

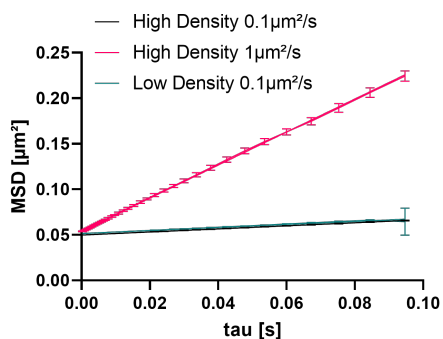


Figure C.5.: M2R-Mut8 expression check in the Cy3-channel

D. Analysing the diffusion behaviour of the M2R-Mut8 - Cy3 with the Python script

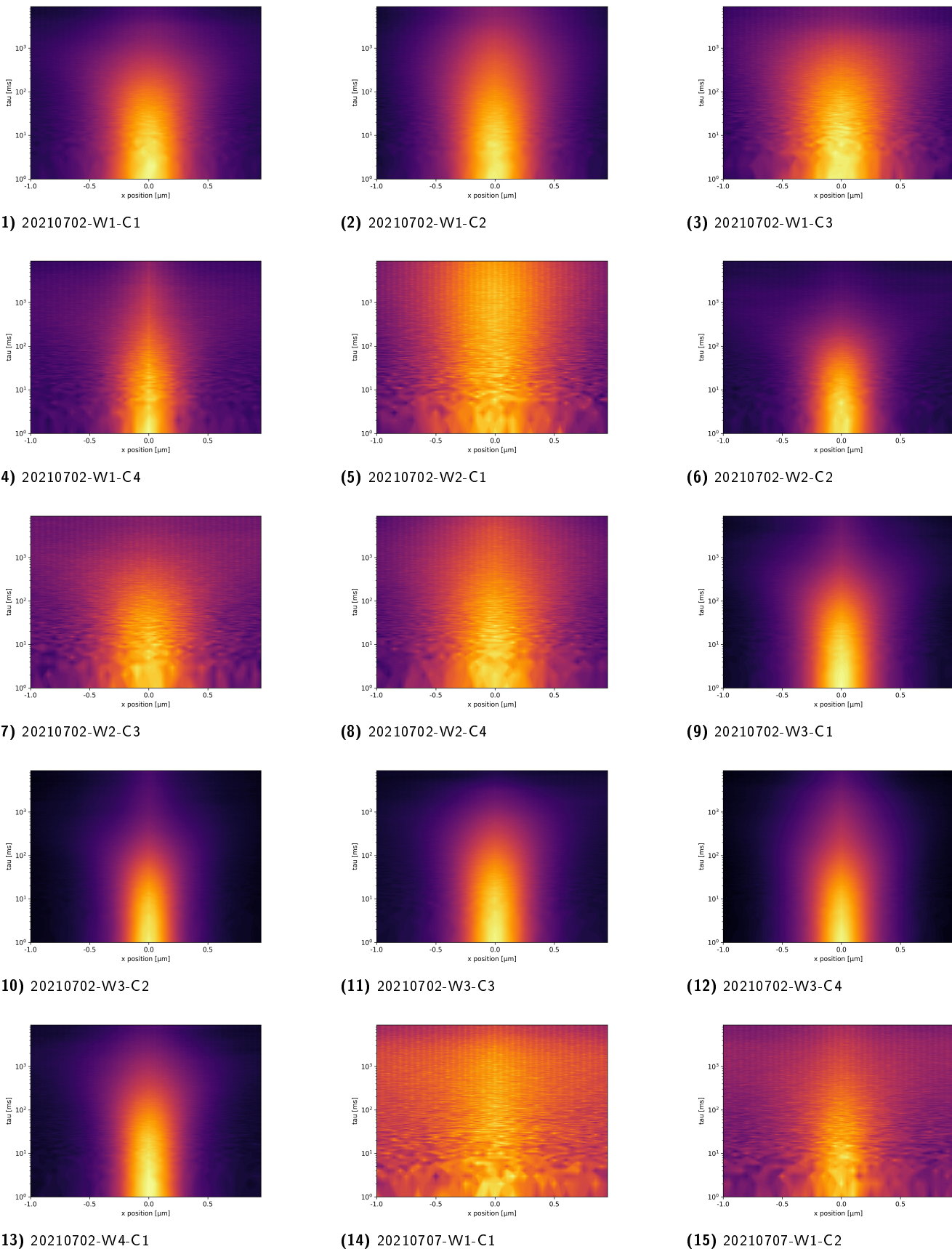


Figure D.7.: Collection of all STICS function heat maps of the non-stimulated M2R-Mut8 samples. Part I

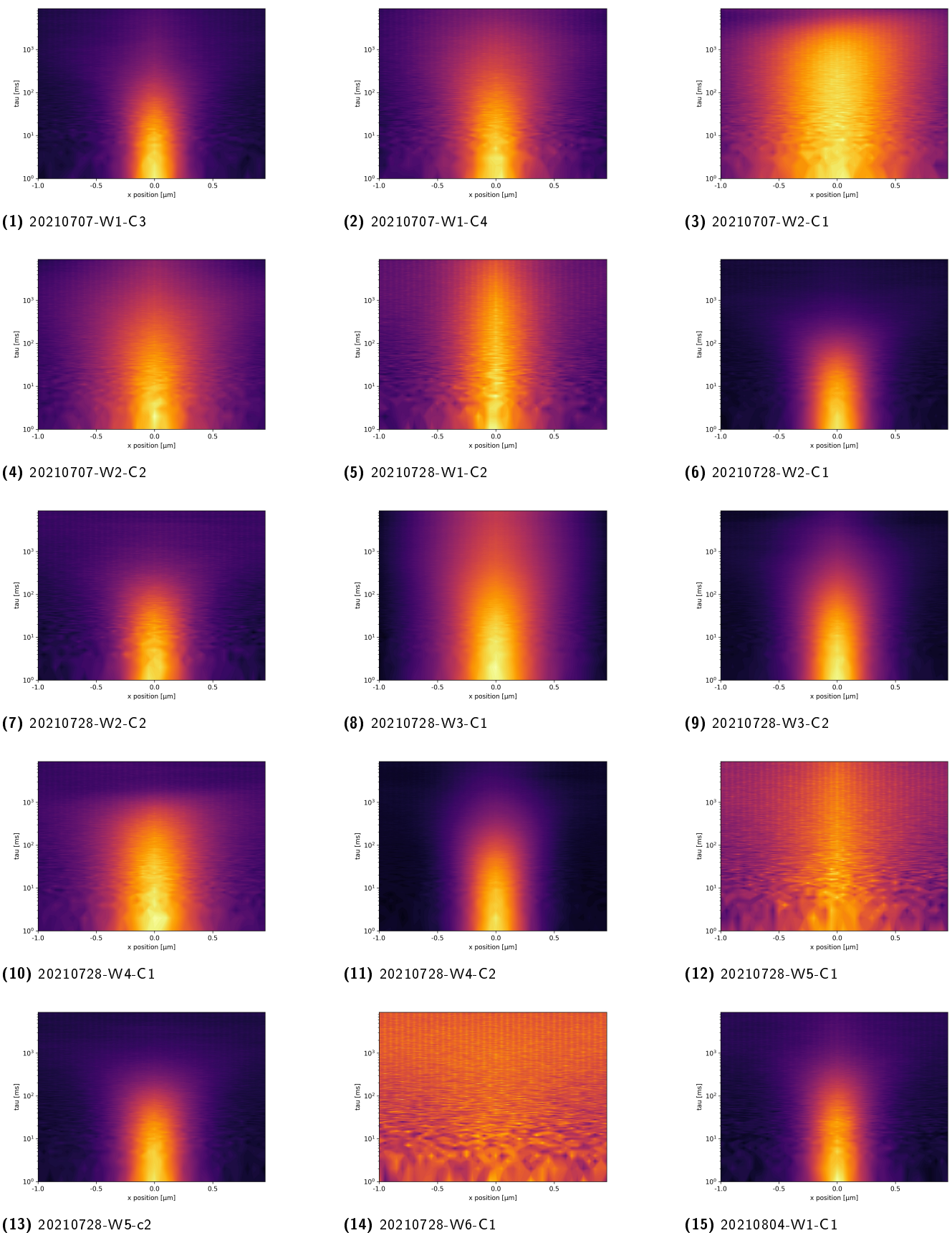
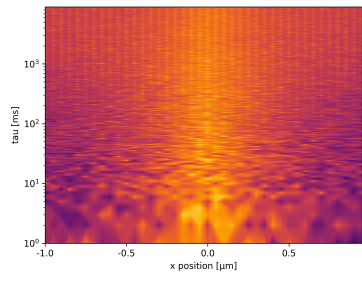
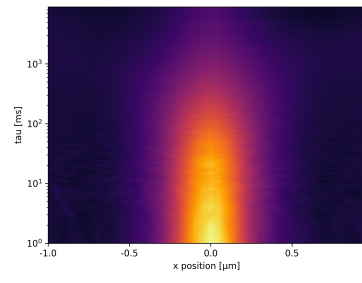


Figure D.8.: Collection of all STICS function heat maps of the non-stimulated M2R-Mut8 samples. Part II



(1) 20210804-W2-C1

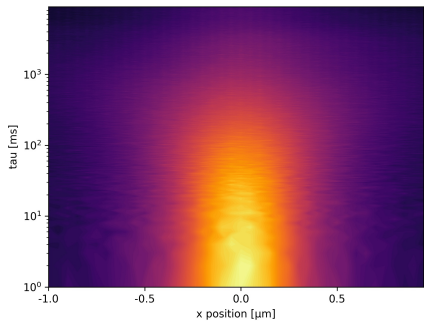


(2) 20210804-W2-C2

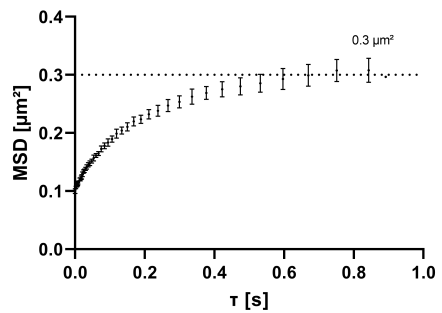
Figure D.9.: Collection of all STICS function heat maps of the non-stimulated M2R-Mut8 samples. Part III

E. Analysing the diffusion behaviour of the M2R-Mut8 upon receptor activation

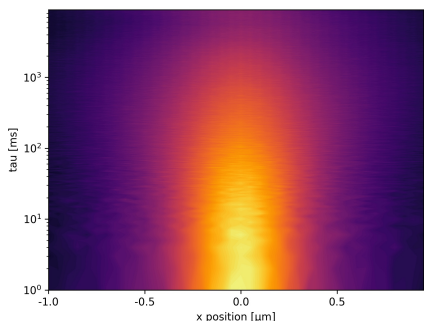
E. Analysing the diffusion behaviour of the M2R-Mut8 upon receptor activation



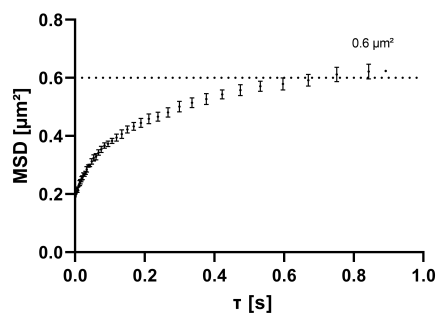
(1) 20210702-W1-C1
STICS function



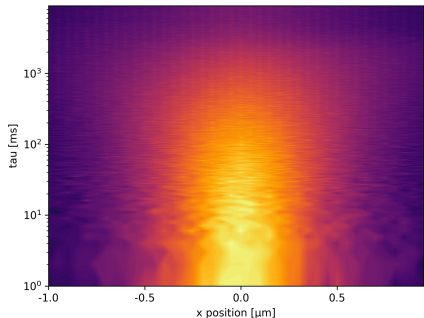
(2) 20210702-W1-C1
MSD-plot ($\tau < 1$ s)



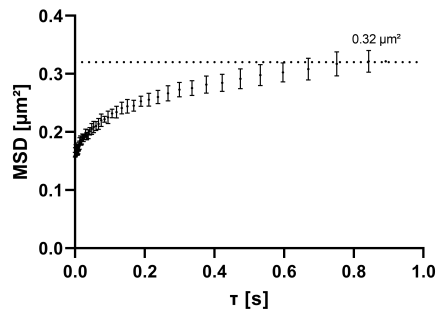
(3) 20210702-W1-C2
STICS function



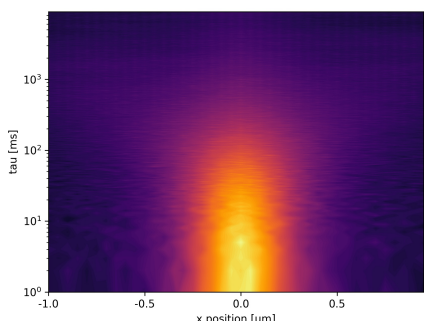
(4) 20210702-W1-C2
MSD-plot ($\tau < 1$ s)



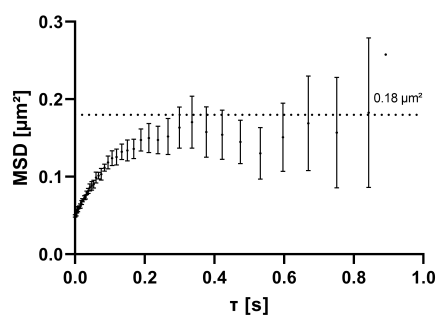
(5) 20210702-W1-C3
STICS function



(6) 20210702-W1-C3
MSD-plot ($\tau < 1$ s)

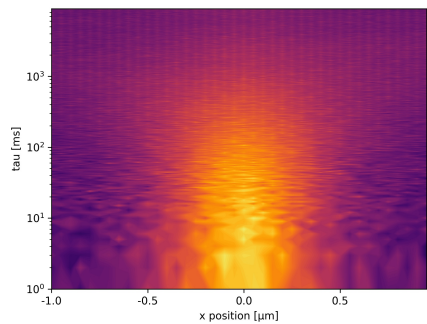


(7) 20210702-W2-C2
STICS function

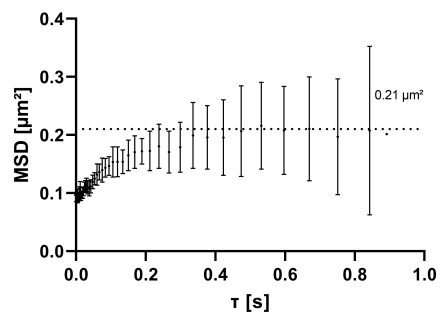


(8) 20210702-W2-C2
MSD-plot ($\tau < 1$ s)

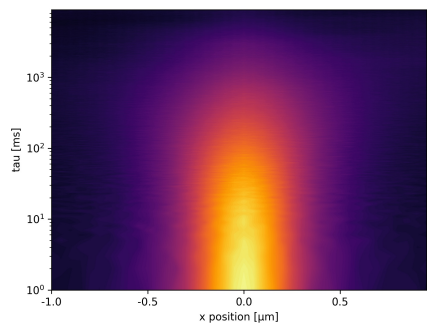
Figure D.10.: The STICS function heat maps of the pre-selected non-stimulated M2R-Mut8 subset and the corresponding MSD plots. Part I



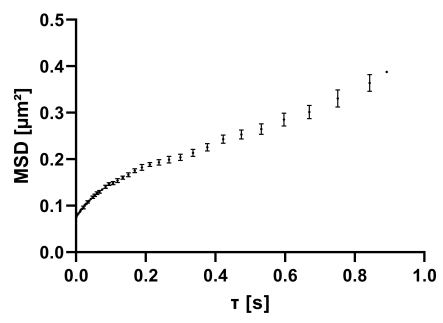
(1) 20210702-W2-C3
STICS function



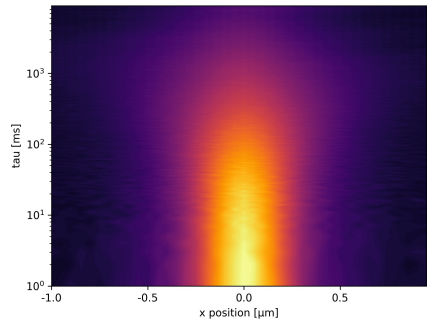
(2) 20210702-W2-C3
MSD-plot ($\tau < 1$ s)



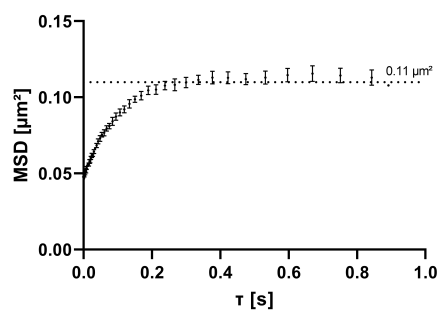
(3) 20210702-W3-C3
STICS function



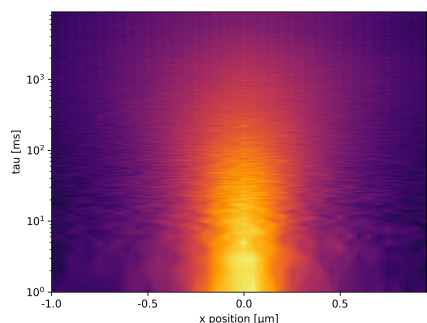
(4) 20210702-W3-C3
MSD-plot ($\tau < 1$ s)



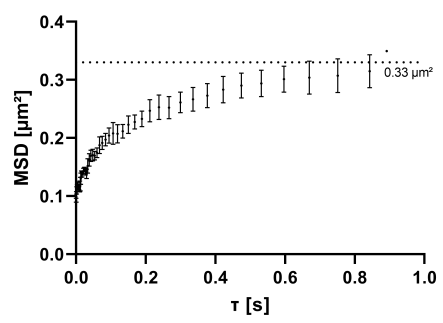
(5) 20210702-W4-C1
STICS function



(6) 20210702-W4-C1
MSD-plot ($\tau < 1$ s)

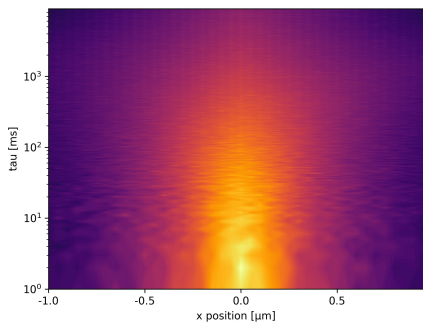


(7) 20210707-W1-C4
STICS function

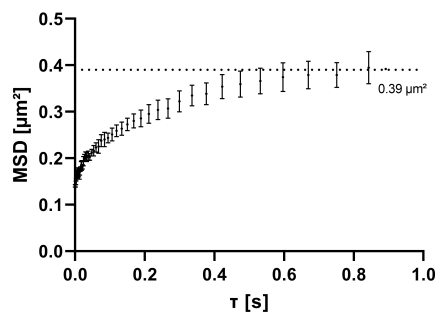


(8) 20210707-W1-C4
MSD-plot ($\tau < 1$ s)

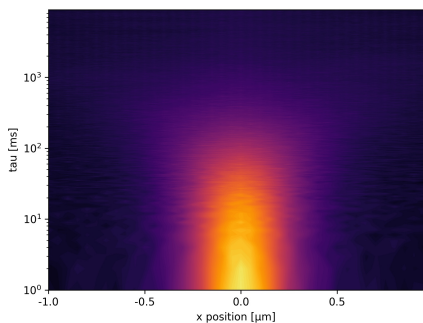
Figure D.11.: The STICS function heat maps of the pre-selected non-stimulated M2R-Mut8 subset and the corresponding MSD plots. Part II



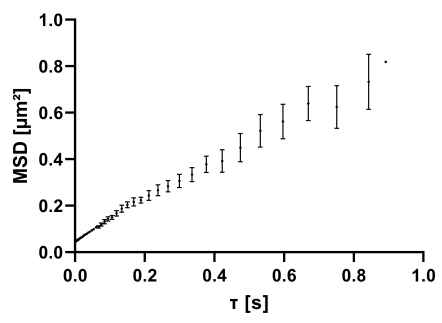
(1) 20210707-W2-C2
STICS function



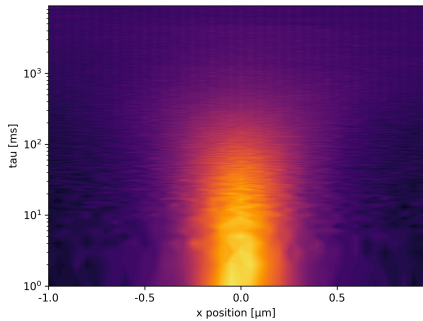
(2) 20210707-W2-C2
MSD-plot ($\tau < 1$ s)



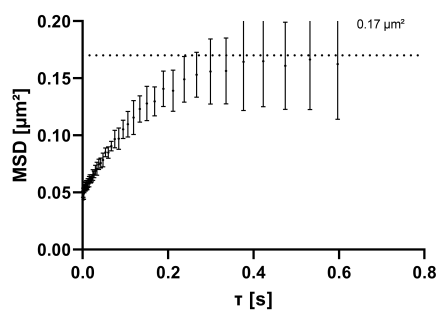
(3) 20210728-W2-C1
STICS function



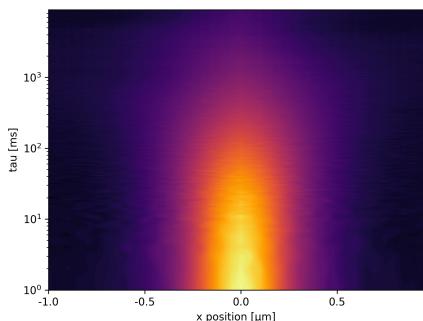
(4) 20210728-W2-C1
MSD-plot ($\tau < 1$ s)



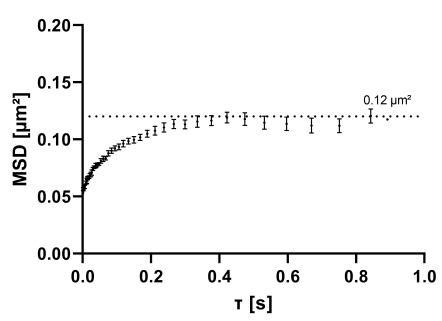
(5) 20210728-W2-C2
STICS function



(6) 20210728-W2-C2
MSD-plot ($\tau < 1$ s)

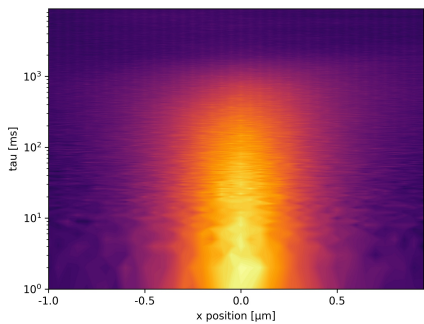


(7) 20210728-W3-C2
STICS function

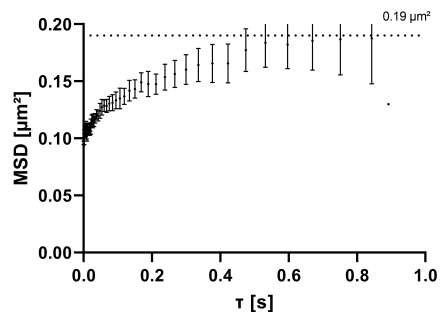


(8) 20210728-W3-C2
MSD-plot ($\tau < 1$ s)

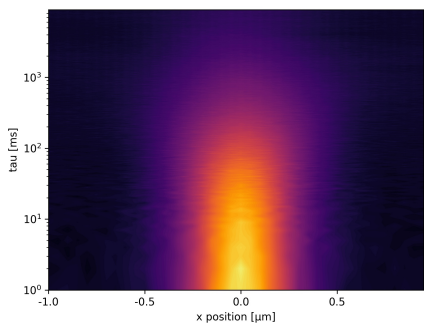
Figure D.12.: The STICS function heat maps of the pre-selected non-stimulated M2R-Mut8 subset and the corresponding MSD plots. Part III



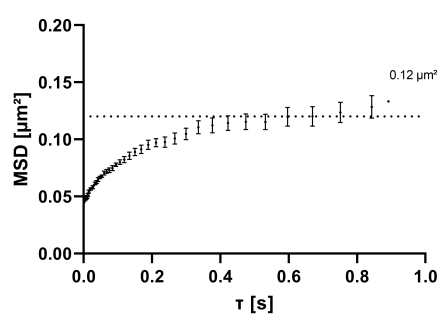
(1) 20210728-W4-C1
STICS function



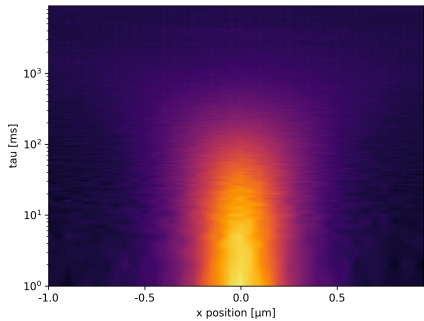
(2) 20210728-W4-C1
MSD-plot ($\tau < 1 \text{ s}$)



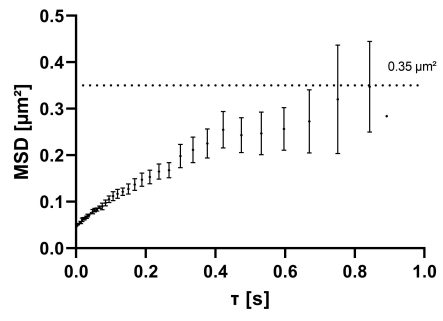
(3) 20210728-W4-C2
STICS function



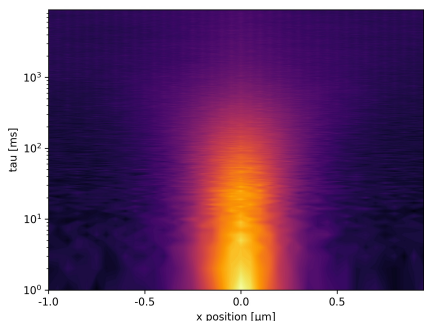
(4) 20210728-W4-C2
MSD-plot ($\tau < 1 \text{ s}$)



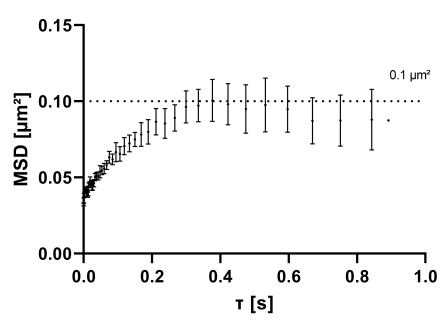
(5) 20210728-W5-c2
STICS function



(6) 20210728-W5-c2
MSD-plot ($\tau < 1 \text{ s}$)



(7) 20210804-W1-C1
STICS function



(8) 20210804-W1-C1
MSD-plot ($\tau < 1 \text{ s}$)

Figure D.13.: The STICS function heat maps of the pre-selected non-stimulated M2R-Mut8 subset and the corresponding MSD plots. Part IV

E. Analysing the diffusion behaviour of the M2R-Mut8 upon receptor activation

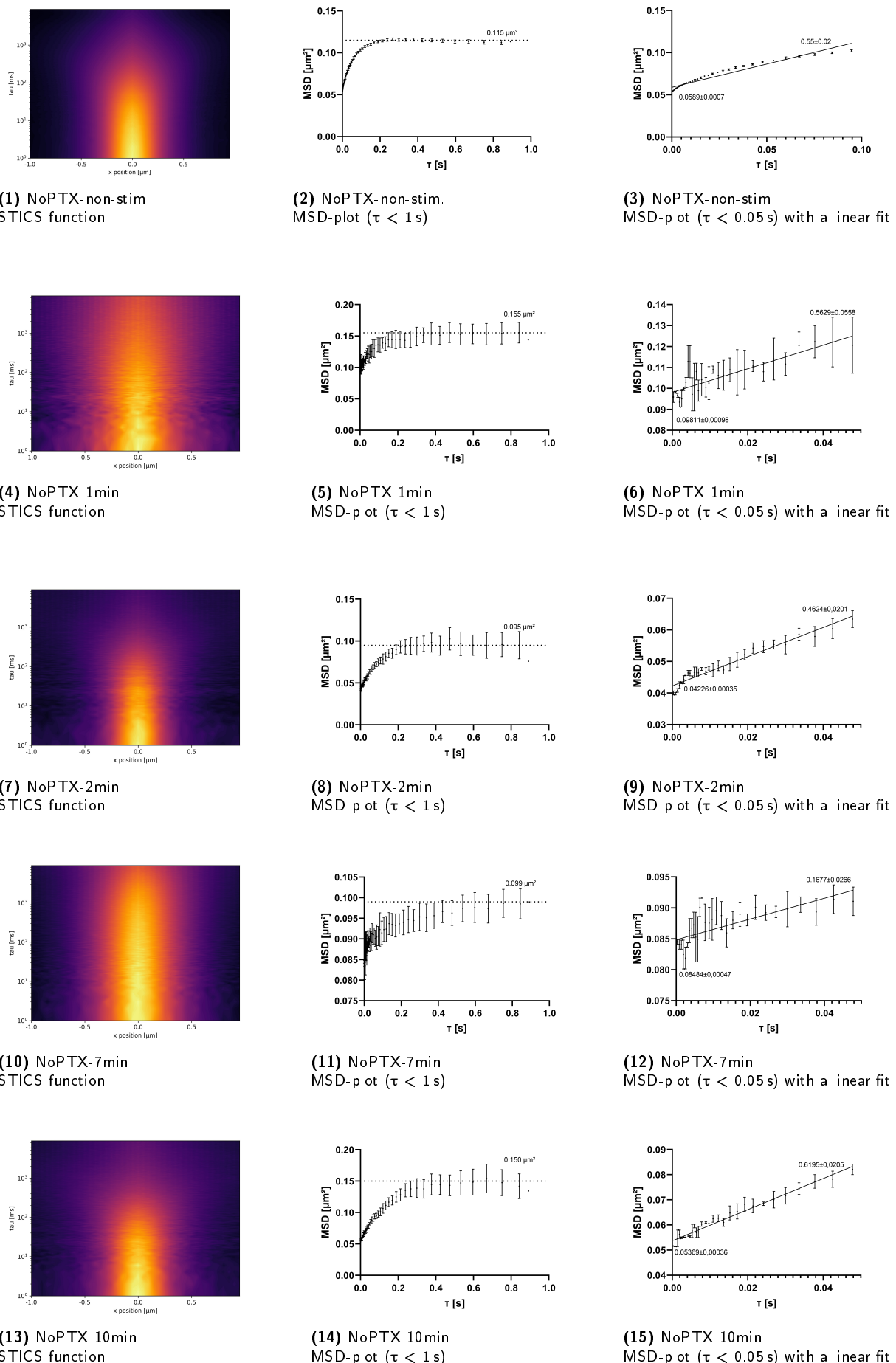


Figure E.14.: Averaged STICS function plots and MSD plots of all non-PTX-treated M2R-Mut8 experiments at different time-points after ACh stimulation.

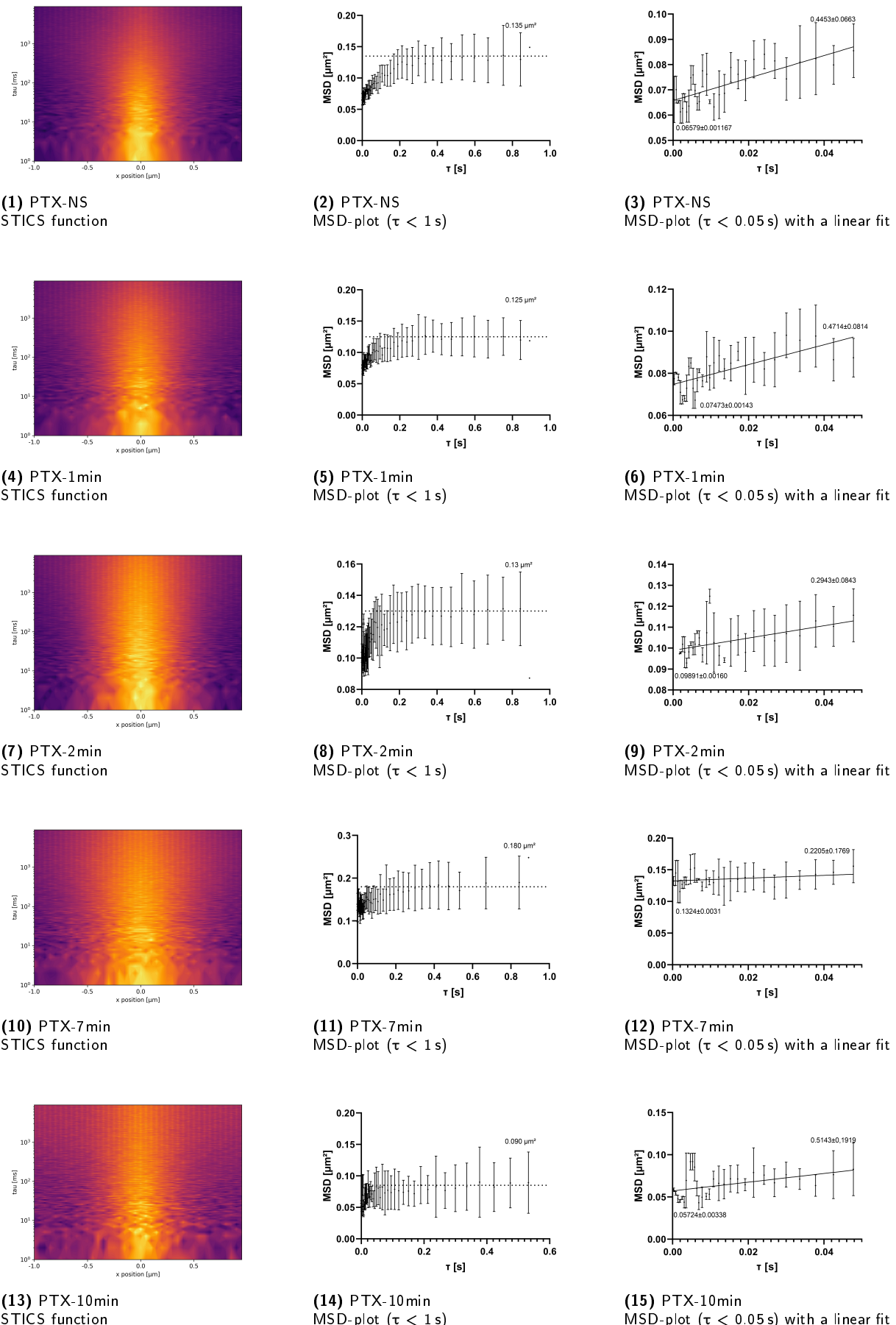
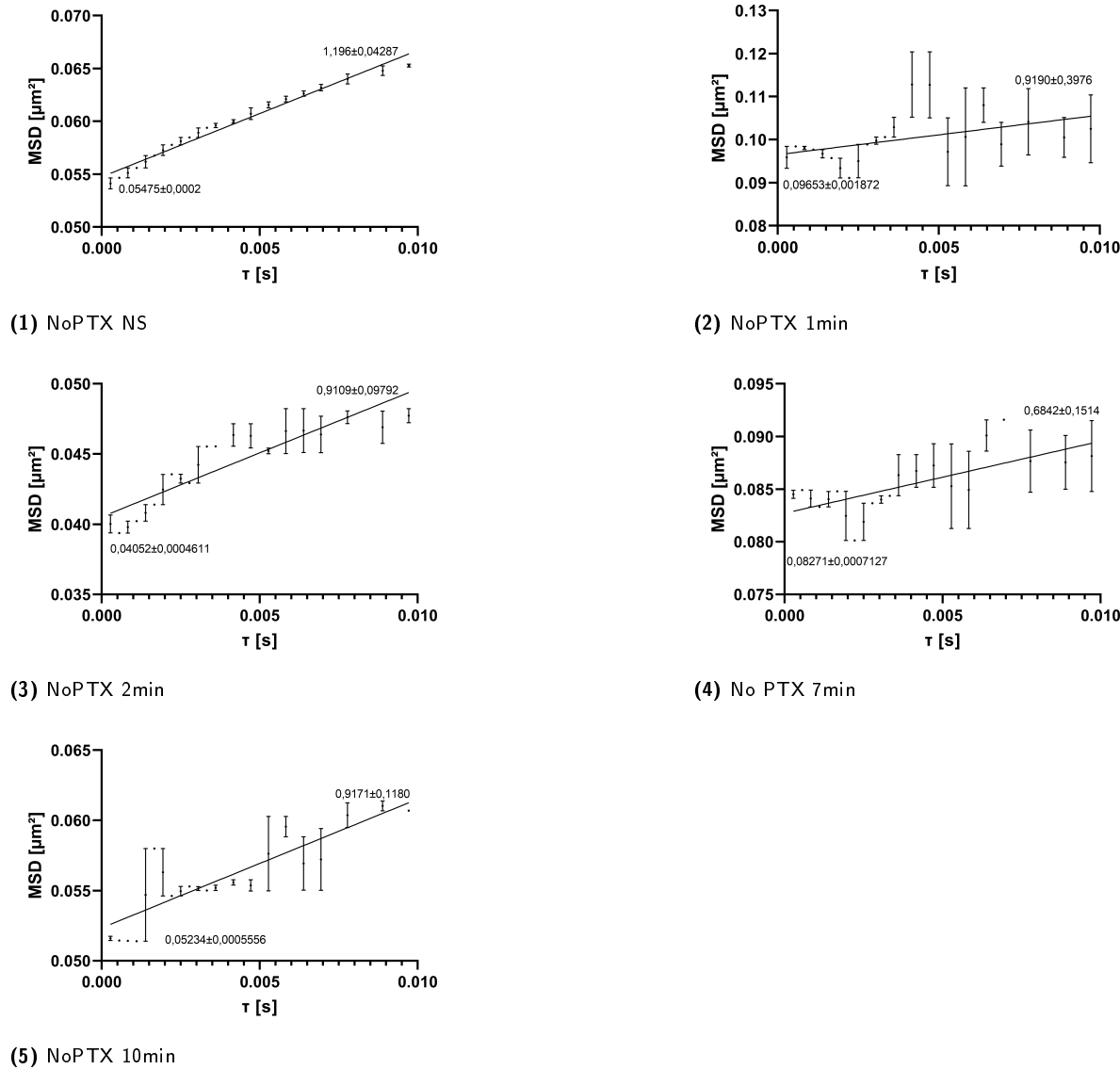


Figure E.15.: Averaged STICS function plots and MSD plots of all PTX-treated M2R-Mut8 experiments, non-treated and at different time-points after ACh stimulation.



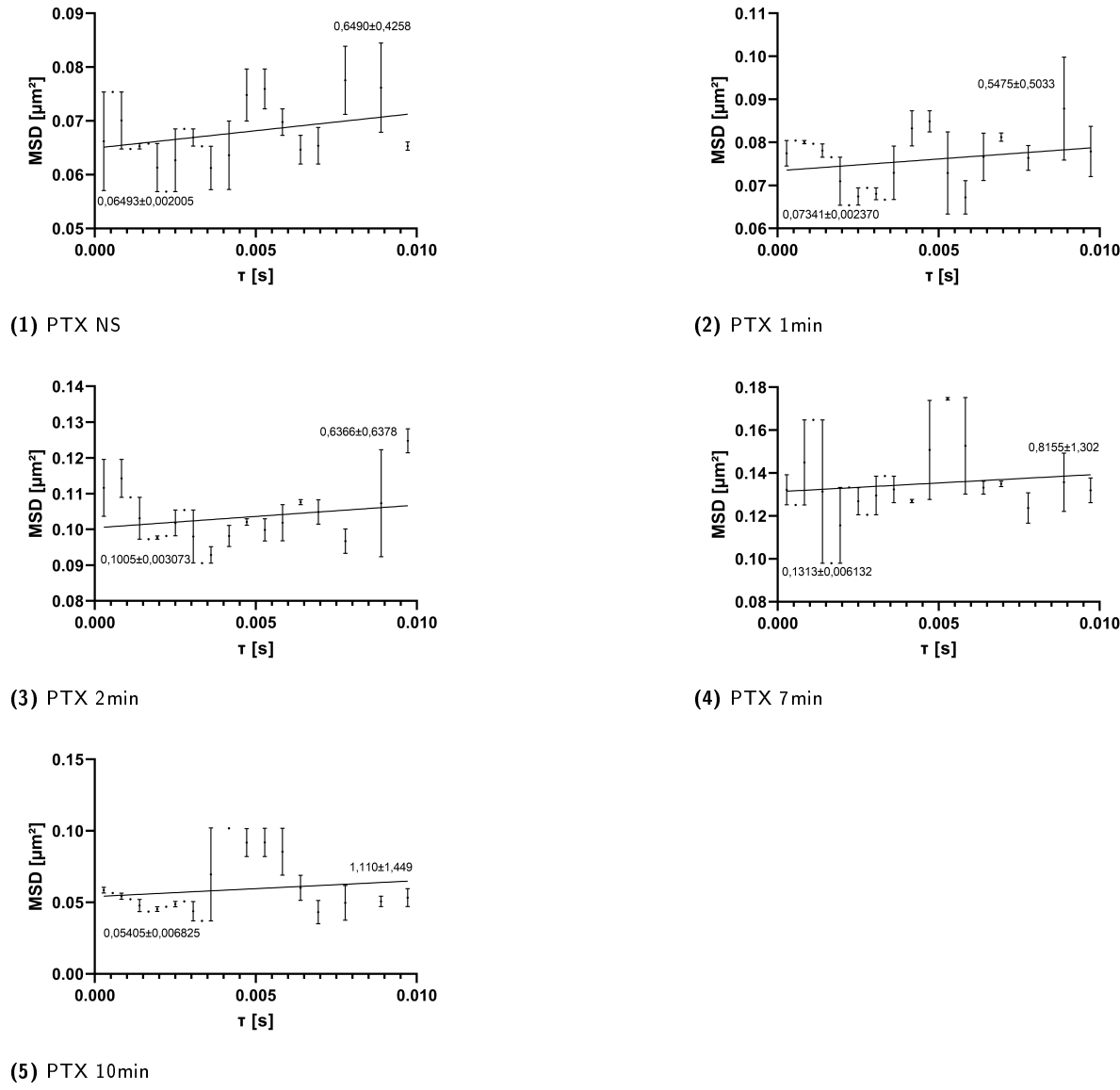


Figure E.17.: Linear fit for $\tau < 10\text{ms}$ of the MSD plots of all PTX treated M2R-Mut8 samples.

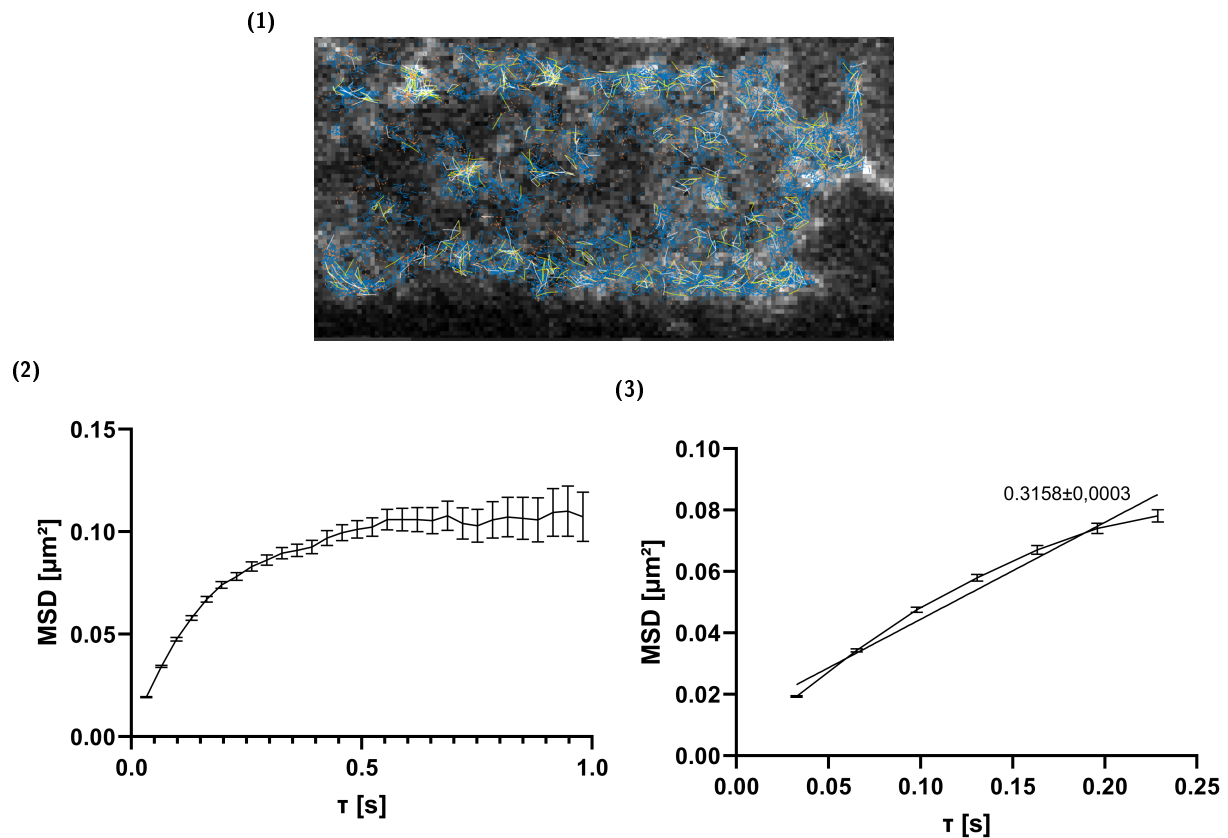


Figure E.18.: Exemplary data-extraction from one SMT experiment. (A) shows the extracted traces of a 30 s time interval. These are used to calculate the MSD-values over τ as described in section 4.2.11.2. (B) shows the resulting MSD plot for $\tau < 1$ s. The τ interval $\tau < 0.25$ s (C) was subsequently used for linear fitting and D value extraction.

F. Settings to be checked and adapted by the user

Several settings have to be adapted for the individual analysis of line scans. Until now, they have to be changed in the first lines of the main program. Further down the road, it would be more user-friendly to have a graphical user interface to prompt the user to specify those values.

- **Hz Aquisition:** Lines per second (acquisition setting)
- **Pixellength:** Pixel diameter in nm (acquisition setting).
- **max tau Gaussian in ms:** The maximal tau value to consider when calculating D by Gaussian fitting over the spatial domain. Taking higher tau values makes the execution of the program slower and does not necessarily give any benefit as the amplitude of the gaussian distribution decreases with increasing tau and finally decorrelates depending on the diffusion speed. Thus, one should choose this value to be the smallest that still

incorporates the area which shows a clear Gaussian distribution, verifiable by checking the implemented 3D plot of the Gaussian profiles over tau. For molecular processes, 1 second is a generous choice.

- **BinSeconds:** A typical LS is way longer than the needed max tau interval. For calculation of the STICS function, it is cut through the time axis into equally long intervals that are then individually calculated and averaged to get a robust STICS result that can be checked in the plume/contour plot visualization. Consequently, it is also used to set the bin sizes and log axis boundaries for the subsequent display and export of the calculated analysis outputs. The setting here again depends on the speed of the observed process.

Additionally, the program asks the user to check the Intensity-sum plots both in the spatial and the temporal domain and to define the area to be used for calculation. This enables the user to exclude for example vesicles/membrane folds which show as intensity sum peaks in the spatial direction and to exclude time intervals of strong bleaching which results in a drop in intensity sum over time.

Bibliography

- [1] Kristen L. Pierce, Richard T. Premont, and Robert J. Lefkowitz, “Seven-transmembrane receptors”, *Nature Reviews Molecular Cell Biology*, vol. 3, no. 9, pp. 639–650, Sep. 2002, Bandiera_abtest: a Cg_type: Nature Research Journals Number: 9 Primary_atype: Reviews Publisher: Nature Publishing Group, ISSN: 1471-0080 (cit. on pp. 1, 2, 4).
- [2] Malin C. Lagerström and Helgi B. Schiöth, “Structural diversity of g protein-coupled receptors and significance for drug discovery”, *Nature Reviews Drug Discovery*, vol. 7, no. 4, pp. 339–357, Apr. 2008, Bandiera_abtest: a Cg_type: Nature Research Journals Number: 4 Primary_atype: Reviews Publisher: Nature Publishing Group, ISSN: 1474-1784 (cit. on pp. 1, 2).
- [3] Khaled Alhosaini, Asim Azhar, Asma Alonazi, and F Al-Zoghaibi, “GPCRs: The most promiscuous druggable receptor of the mankind”, *Saudi Pharmaceutical Journal : SPJ*, vol. 29, no. 6, pp. 539–551, Jun. 2021, ISSN: 1319-0164 (cit. on p. 1).
- [4] Jean-Pierre Vilardaga, Moritz Bünenmann, Timothy N. Feinstein, Nevin Lambert, Viacheslav O. Nikolaev, Stefan Engelhardt, Martin J. Lohse, and Carsten Hoffmann, “Minireview: GPCR and g proteins: Drug efficacy and activation in live cells”, *Molecular Endocrinology*, vol. 23, no. 5, pp. 590–599, May 1, 2009, ISSN: 0888-8809 (cit. on p. 1).
- [5] Marc Bathe-Peters, Philipp Gmach, Horst-Holger Boltz, Jürgen Einsiedel, Michael Gotthardt, Harald Hübner, Peter Gmeiner, Martin J. Lohse, and Paolo Annibale, “Visualization of β-adrenergic receptor dynamics and differential localization in cardiomyocytes”, *Proceedings of the National Academy of Sciences of the United States of America*, vol. 118, no. 23, e2101119118, Jun. 8, 2021, ISSN: 1091-6490 (cit. on pp. 1, 44).
- [6] Maria Julia Marinissen and J. Silvio Gutkind, “G-protein-coupled receptors and signaling networks: Emerging paradigms”, *Trends in Pharmacological Sciences*, vol. 22, no. 7, pp. 368–376, Jul. 1, 2001, ISSN: 0165-6147 (cit. on pp. 1–3).
- [7] Davide Calebiro and Zsombor Koszegi, “The subcellular dynamics of GPCR signaling”, *Molecular and Cellular Endocrinology*, vol. 483, pp. 24–30, Mar. 1, 2019, ISSN: 0303-7207 (cit. on p. 1).

- [8] Ali İşbilir, Robert Serfling, Jan Möller, Romy Thomas, Chiara De Faveri, Ulrike Zabel, Marco Scarselli, Annette G. Beck-Sickinger, Andreas Bock, Irene Coin, Martin J. Lohse, and Paolo Annibale, “Determination of g-protein–coupled receptor oligomerization by molecular brightness analyses in single cells”, *Nature Protocols*, pp. 1–36, Jan. 29, 2021, Publisher: Nature Publishing Group, ISSN: 1750-2799 (cit. on pp. 1, 31, 63).
- [9] Carsten Hoffmann, Guido Gaietta, Moritz Bünenmann, Stephen R. Adams, Silke Oberdorff-Maass, Björn Behr, Jean-Pierre Vilardaga, Roger Y. Tsien, Mark H. Ellisman, and Martin J. Lohse, “A FlAsH-based FRET approach to determine g protein–coupled receptor activation in living cells”, *Nature Methods*, vol. 2, no. 3, pp. 171–176, Mar. 2005, Bandiera_abtest: a Cg_type: Nature Research Journals Number: 3 Primary_atype: Research Publisher: Nature Publishing Group, ISSN: 1548-7105 (cit. on pp. 1, 7, 63).
- [10] Robert Serfling, Lisa Seidel, Andreas Bock, Martin J. Lohse, Paolo Annibale, and Irene Coin, “Quantitative single-residue bioorthogonal labeling of g protein-coupled receptors in live cells”, *ACS Chemical Biology*, vol. 14, no. 6, pp. 1141–1149, Jun. 21, 2019, Publisher: American Chemical Society, ISSN: 1554-8929 (cit. on pp. 1, 2, 7, 44, 53, 62, 63, 65).
- [11] “Click amino acid / trans-cyclooct-2-en – l - lysine (TCO*a)”. (), [Online]. Available: <https://shop.sichem.de/en/sc-8008.html> (visited on 01/08/2022) (cit. on pp. 1, 7).
- [12] Jena Bioscience GmbH. “Tetrazine-cy3, tetrazine-containing fluorescent dyes”, Jena Bioscience. (), [Online]. Available: <https://www.jenabioscience.com/probes-epigenetics/reactive-components/reactive-fluorescent-dyes/tetrazines/clk-014-tetrazine-cy3> (visited on 01/08/2022) (cit. on pp. 1, 7).
- [13] “EGFP sequence and map”, SnapGene. (), [Online]. Available: https://www.snapgene.com/resources/plasmid-files/?set=fluorescent_protein_genes_and_plasmids&plasmid=EGFP (visited on 01/08/2022) (cit. on pp. 1, 7).
- [14] “SNAP-tag sequence and map”, SnapGene. (), [Online]. Available: https://www.snapgene.com/resources/plasmid-files/?set=basic_cloning_vectors&plasmid=SNAP-tag (visited on 01/08/2022) (cit. on p. 1).
- [15] Marc Bathe-Peters, Philipp Gmach, Paolo Annibale, and Martin J. Lohse, “Linescan microscopy data to extract diffusion coefficient of a fluorescent species using a commercial confocal microscope”, *Data in Brief*, vol. 29, p. 105 063, Apr. 1, 2020, ISSN: 2352-3409 (cit. on pp. 2, 14, 39, 40, 42, 43).
- [16] Carmine Di Renzo, Enrico Gratton, Fabio Beltram, and Francesco Cardarelli, “Fast spatiotemporal correlation spectroscopy to determine protein lateral diffusion laws in live cell membranes”, *Proceedings of the National Academy of Sciences of the United*

- States of America*, vol. 110, no. 30, pp. 12 307–12 312, Jul. 23, 2013, ISSN: 0027-8424 (cit. on pp. 2, 12, 14–16, 66).
- [17] Jonas Ries, Salvatore Chiantia, and Petra Schwille, “Accurate determination of membrane dynamics with line-scan FCS”, *Biophysical Journal*, vol. 96, no. 5, pp. 1999–2008, Mar. 4, 2009, ISSN: 0006-3495 (cit. on p. 2).
- [18] Krishna Sriram and Paul A. Insel, “G protein-coupled receptors as targets for approved drugs: How many targets and how many drugs?”, *Molecular Pharmacology*, vol. 93, no. 4, pp. 251–258, Apr. 2018, ISSN: 0026-895X (cit. on p. 2).
- [19] Andreas Bock and Marcel Bermudez, “Allosteric coupling and biased agonism in g protein-coupled receptors”, *The FEBS Journal*, vol. 288, no. 8, pp. 2513–2528, 2021, _eprint: <https://febs.onlinelibrary.wiley.com/doi/pdf/10.1111/febs.15783>, ISSN: 1742-4658 (cit. on p. 2).
- [20] Ning Ma, Anita K. Nivedha, and Nagarajan Vaidehi, “Allosteric communication regulates ligand-specific GPCR activity”, *The FEBS Journal*, vol. 288, no. 8, pp. 2502–2512, 2021, _eprint: <https://febs.onlinelibrary.wiley.com/doi/pdf/10.1111/febs.15826>, ISSN: 1742-4658 (cit. on p. 2).
- [21] Nina Wettschureck and Stefan Offermanns, “Mammalian g proteins and their cell type specific functions”, *Physiological Reviews*, vol. 85, no. 4, pp. 1159–1204, Oct. 1, 2005, Publisher: American Physiological Society, ISSN: 0031-9333 (cit. on p. 3).
- [22] Kouki K Touhara and Roderick MacKinnon, “Molecular basis of signaling specificity between GIRK channels and GPCRs”, *eLife*, vol. 7, Kenton Jon Swartz and Richard Aldrich, Eds., e42908, Dec. 10, 2018, Publisher: eLife Sciences Publications, Ltd, ISSN: 2050-084X (cit. on p. 3).
- [23] Edda S. F. Matthees, Raphael S. Haider, Carsten Hoffmann, and Julia Drube, “Differential regulation of GPCRs—are GRK expression levels the key?”, *Frontiers in Cell and Developmental Biology*, vol. 9, p. 687 489, May 24, 2021, ISSN: 2296-634X (cit. on p. 4).
- [24] Seungkirl Ahn, Sudha K. Shenoy, Louis M. Luttrell, and Robert J. Lefkowitz, “SnapShot: B-arrestin functions”, *Cell*, vol. 182, no. 5, 1362–1362.e1, Sep. 2020, ISSN: 00928674 (cit. on p. 4).
- [25] Jennifer J. Linderman, “Modeling of g-protein-coupled receptor signaling pathways *”, *Journal of Biological Chemistry*, vol. 284, no. 9, pp. 5427–5431, Feb. 27, 2009, Publisher: Elsevier, ISSN: 0021-9258, 1083-351X (cit. on p. 5).
- [26] Aviva M. Tolkovsky and Alexander Levitzki, “Mode of coupling between the β-adrenergic receptor and adenylate cyclase in turkey erythrocytes”, *Biochemistry*, vol. 17, no. 18, pp. 3795–3810, Sep. 5, 1978, Publisher: American Chemical Society, ISSN: 0006-2960 (cit. on p. 5).

- [27] S. J. Singer and Garth L. Nicolson, “The fluid mosaic model of the structure of cell membranes”, *Science*, Feb. 18, 1972, Publisher: American Association for the Advancement of Science (cit. on p. 5).
- [28] W. Gross and M. J. Lohse, “Mechanism of activation of a₂ adenosine receptors. II. a restricted collision-coupling model of receptor-effector interaction.”, *Molecular Pharmacology*, vol. 39, no. 4, pp. 524–530, Apr. 1, 1991, Publisher: American Society for Pharmacology and Experimental Therapeutics, ISSN: 0026-895X, 1521-0111 (cit. on p. 5).
- [29] John A. Allen, Robyn A. Halverson-Tamboli, and Mark M. Rasenick, “Lipid raft microdomains and neurotransmitter signalling”, *Nature Reviews Neuroscience*, vol. 8, no. 2, pp. 128–140, Feb. 2007, Bandiera_abtest: a Cg_type: Nature Research Journals Number: 2 Primary_atype: Reviews Publisher: Nature Publishing Group, ISSN: 1471-0048 (cit. on pp. 5, 64).
- [30] H. H. Patel, F. Murray, and P. A. Insel, “G-protein-coupled receptor-signaling components in membrane raft and caveolae microdomains”, in *Protein-Protein Interactions as New Drug Targets*, ser. Handbook of Experimental Pharmacology, Enno Klussmann and John Scott, Eds., Berlin, Heidelberg: Springer, 2008, pp. 167–184, ISBN: 978-3-540-72843-6 (cit. on p. 5).
- [31] Sean Munro, “Lipid rafts: Elusive or illusive?”, *Cell*, vol. 115, no. 4, pp. 377–388, Nov. 14, 2003, Publisher: Elsevier, ISSN: 0092-8674, 1097-4172 (cit. on p. 5).
- [32] Marek Cebecauer, Mariana Amaro, Piotr Jurkiewicz, Maria João Sarmento, Radek Šachl, Lukasz Cwiklik, and Martin Hof, “Membrane lipid nanodomains”, *Chemical Reviews*, vol. 118, no. 23, pp. 11259–11297, Dec. 12, 2018, ISSN: 0009-2665, 1520-6890 (cit. on p. 5).
- [33] Carla M. Rosetti, Agustín Mangiarotti, and Natalia Wilke, “Sizes of lipid domains: What do we know from artificial lipid membranes? what are the possible shared features with membrane rafts in cells?”, *Biochimica et Biophysica Acta (BBA) - Biomembranes*, vol. 1859, no. 5, pp. 789–802, May 1, 2017, ISSN: 0005-2736 (cit. on p. 5).
- [34] Thomas Huber and Thomas P. Sakmar, “Escaping the flatlands: New approaches for studying the dynamic assembly and activation of GPCR signaling complexes”, *Trends in Pharmacological Sciences*, vol. 32, no. 7, pp. 410–419, Jul. 1, 2011, ISSN: 0165-6147 (cit. on p. 5).
- [35] Andreas Bock, Paolo Annibale, Charlotte Konrad, Annette Hannawacker, Selma E. Anton, Isabella Maiellaro, Ulrike Zabel, Sivaraj Sivaramakrishnan, Martin Falcke, and Martin J. Lohse, “Optical mapping of cAMP signaling at the nanometer scale”, *Cell*, vol. 182, no. 6, 1519–1530.e17, Sep. 17, 2020, ISSN: 0092-8674 (cit. on p. 5).

Bibliography

- [36] Muriel Nobles, Amy Benians, and Andrew Tinker, “Heterotrimeric g proteins precouple with g protein-coupled receptors in living cells”, *Proceedings of the National Academy of Sciences of the United States of America*, vol. 102, no. 51, pp. 18 706–18 711, Dec. 20, 2005, ISSN: 0027-8424 (cit. on p. 5).
- [37] Masataka Yanagawa, Michio Hiroshima, Yuichi Togashi, Mitsuhiro Abe, Takahiro Yamashita, Yoshinori Shichida, Masayuki Murata, Masahiro Ueda, and Yasushi Sako, “Single-molecule diffusion-based estimation of ligand effects on g protein-coupled receptors”, *Science Signaling*, Sep. 18, 2018, Publisher: American Association for the Advancement of Science (cit. on pp. 5, 65).
- [38] Stefan Gahbauer and Rainer A. Böckmann, “Membrane-mediated oligomerization of g protein coupled receptors and its implications for GPCR function”, *Frontiers in Physiology*, vol. 7, p. 494, 2016, ISSN: 1664-042X (cit. on p. 6).
- [39] Stephen J. Briddon, Jorge Gandía, Olavo B. Amaral, Sergi Ferré, Carme Lluís, Rafael Franco, Stephen J. Hill, and Francisco Ciruela, “Plasma membrane diffusion of g protein-coupled receptor oligomers”, *Biochimica et Biophysica Acta (BBA) - Molecular Cell Research*, vol. 1783, no. 12, pp. 2262–2268, Dec. 1, 2008, ISSN: 0167-4889 (cit. on p. 6).
- [40] Paul S.-H. Park and James W. Wells, “Oligomeric potential of the m2 muscarinic cholinergic receptor”, *Journal of Neurochemistry*, vol. 90, no. 3, pp. 537–548, 2004, _eprint: <https://onlinelibrary.wiley.com/doi/pdf/10.1111/j.1471-4159.2004.02536.x>, ISSN: 1471-4159 (cit. on pp. 6, 64).
- [41] Juan C. Goin and Neil M. Nathanson, “Quantitative analysis of muscarinic acetylcholine receptor homo- and heterodimerization in live cells: REGULATION OF RECEPTOR DOWN-REGULATION BY HETERO-DIMERIZATION*”, *Journal of Biological Chemistry*, vol. 281, no. 9, pp. 5416–5425, Mar. 3, 2006, Publisher: Elsevier, ISSN: 0021-9258, 1083-351X (cit. on pp. 6, 64).
- [42] Luca F. Pisterzi, David B. Jansma, John Georgiou, Michael J. Woodside, Judy Tai-Chieh Chou, Stéphane Angers, Valerică Raicu, and James W. Wells, “Oligomeric size of the m2 muscarinic receptor in live cells as determined by quantitative fluorescence resonance energy transfer*”, *Journal of Biological Chemistry*, vol. 285, no. 22, pp. 16 723–16 738, May 28, 2010, ISSN: 0021-9258 (cit. on pp. 6, 64).
- [43] Davide Calebiro and Titiwat Sungkaworn, “Single-molecule imaging of GPCR interactions”, *Trends in Pharmacological Sciences*, Special Issue: Illuminating GPCRs in Living Cells, vol. 39, no. 2, pp. 109–122, Feb. 1, 2018, ISSN: 0165-6147 (cit. on p. 6).

- [44] Y. Cordeaux, S. J. Briddon, S. P. H. Alexander, B. Kellam, and S. J. Hill, “Agonist-occupied a₃ adenosine receptors exist within heterogeneous complexes in membrane microdomains of individual living cells”, *The FASEB Journal*, vol. 22, no. 3, pp. 850–860, 2008, _eprint: <https://onlinelibrary.wiley.com/doi/pdf/10.1096/fj.07-8180com>, ISSN: 1530-6860 (cit. on p. 6).
- [45] Gregory W. Fisher, Sally A. Adler, Margaret H. Fuhrman, Alan S. Waggoner, Marcel P. Bruchez, and Jonathan W. Jarvik, “Detection and quantification of β₂ar internalization in living cells using FAP-based biosensor technology”, *Journal of Biomolecular Screening*, vol. 15, no. 6, pp. 703–709, Jul. 1, 2010, Publisher: SAGE Publications Inc STM, ISSN: 1087-0571 (cit. on p. 6).
- [46] Romy Frenzel, Carsten Voigt, and Ralf Paschke, “The human thyrotropin receptor is predominantly internalized by β-arrestin 2”, *Endocrinology*, vol. 147, no. 6, pp. 3114–3122, Jun. 1, 2006, ISSN: 0013-7227 (cit. on p. 6).
- [47] N Trapaidze, I Gomes, S Cvejic, M Bansinath, and L. A Devi, “Opioid receptor endocytosis and activation of MAP kinase pathway”, *Molecular Brain Research*, vol. 76, no. 2, pp. 220–228, Mar. 29, 2000, ISSN: 0169-328X (cit. on p. 6).
- [48] Paula A. dos Santos Claro, Carolina Inda, Natalia G. Armando, Verónica G. Piazza, Alejandra Attorresi, and Susana Silberstein, “Chapter 15 - assessing real-time signaling and agonist-induced CRHR1 internalization by optical methods”, in *Methods in Cell Biology*, ser. G Protein-Coupled Receptors, Part B, Arun K. Shukla, Ed., vol. 149, Academic Press, Jan. 1, 2019, pp. 239–257 (cit. on p. 6).
- [49] Dmitry Zenko, Dawn Thompson, and James N. Hislop, “Endocytic sorting and down-regulation of the m₂ acetylcholine receptor is regulated by ubiquitin and the ESCRT complex”, *Neuropharmacology*, vol. 162, p. 107828, Jan. 2020, ISSN: 00283908 (cit. on pp. 6, 7).
- [50] He Tian, Alexandre Fürstenberg, and Thomas Huber, “Labeling and single-molecule methods to monitor g protein-coupled receptor dynamics”, *Chemical Reviews*, vol. 117, no. 1, pp. 186–245, Jan. 11, 2017, ISSN: 0009-2665, 1520-6890 (cit. on pp. 7, 63).
- [51] Roger Munier and Georges N. Cohen, “Incorporation d’analogue structuraux d’acides aminés dans les protéines bactériennes”, *Biochimica et Biophysica Acta*, vol. 21, no. 3, pp. 592–593, Sep. 1, 1956, ISSN: 0006-3002 (cit. on p. 7).
- [52] Jeremiah A. Johnson, Ying Y. Lu, James A. Van Deventer, and David A. Tirrell, “Residue-specific incorporation of non-canonical amino acids into proteins: Recent developments and applications”, *Current opinion in chemical biology*, vol. 14, no. 6, pp. 774–780, Dec. 2010, ISSN: 1367-5931 (cit. on pp. 7, 8).

- [53] Chang C. Liu and Peter G. Schultz, “Adding new chemistries to the genetic code”, *Annual Review of Biochemistry*, vol. 79, no. 1, pp. 413–444, Jun. 7, 2010, ISSN: 0066-4154, 1545-4509 (cit. on p. 8).
- [54] Kathrin Lang and Jason W. Chin, “Cellular incorporation of unnatural amino acids and bioorthogonal labeling of proteins”, *Chemical Reviews*, vol. 114, no. 9, pp. 4764–4806, May 14, 2014, ISSN: 0009-2665, 1520-6890 (cit. on p. 8).
- [55] Robert Serfling, Christian Lorenz, Maja Etzel, Gerda Schicht, Thore Böttke, Mario Mörl, and Irene Coin, “Designer tRNAs for efficient incorporation of non-canonical amino acids by the pyrrolysine system in mammalian cells”, *Nucleic Acids Research*, vol. 46, no. 1, pp. 1–10, Jan. 9, 2018, ISSN: 0305-1048 (cit. on p. 8).
- [56] Gerti Beliu, Andreas J. Kurz, Alexander C. Kuhleemann, Lisa Behringer-Pliess, Mara Meub, Natalia Wolf, Jürgen Seibel, Zhen-Dan Shi, Martin Schnermann, Jonathan B. Grimm, Luke D. Lavis, Sören Doose, and Markus Sauer, “Bioorthogonal labeling with tetrazine-dyes for super-resolution microscopy”, *Communications Biology*, vol. 2, no. 1, pp. 1–13, Jul. 19, 2019, Bandiera_abtest: a Cc_license_type: cc_by Cg_type: Nature Research Journals Number: 1 Primary_atype: Research Publisher: Nature Publishing Group Subject_term: Biological fluorescence;Biophysical chemistry Subject_term_id: biological-fluorescence;biophysical-chemistry, ISSN: 2399-3642 (cit. on p. 8).
- [57] Douglas B. Murphy and Michael W. Davidson, *Fundamentals of Light Microscopy and Electronic Imaging*. John Wiley & Sons, Aug. 22, 2012, 904 pp., Google-Books-ID: f8qhtqRjxQMC, ISBN: 978-1-118-38293-6 (cit. on p. 8).
- [58] Derek Toomre, “Cellular imaging using total internal reflection fluorescence microscopy: Theory and instrumentation”, *Cold Spring Harbor Protocols*, vol. 2012, no. 4, pdb.top068650, Apr. 2012, ISSN: 1940-3402, 1559-6095 (cit. on p. 9).
- [59] Kenneth N. Fish, “Total internal reflection fluorescence (TIRF) microscopy”, *Current protocols in cytometry / editorial board, J. Paul Robinson, managing editor ... [et al.]*, vol. 0 12, Unit12.18, Oct. 2009, ISSN: 1934-9297 (cit. on p. 9).
- [60] Ana J. García-Sáez and Petra Schwille, “Single molecule techniques for the study of membrane proteins”, *Applied Microbiology and Biotechnology*, vol. 76, no. 2, pp. 257–266, Aug. 2007, ISSN: 0175-7598, 1432-0614 (cit. on pp. 9, 11).
- [61] H.-H. Boltz, H.-H. Boltz, H.-H. Boltz, A. Sirbu, N. Stelzer, M. J. Lohse, M. J. Lohse, C. Schütte, C. Schütte, P. Annibale, and P. Annibale, “Quantitative spectroscopy of single molecule interaction times”, *Optics Letters*, vol. 46, no. 7, pp. 1538–1541, Apr. 1, 2021, Publisher: Optical Society of America, ISSN: 1539-4794 (cit. on p. 9).
- [62] Amicia D. Elliott, “Confocal microscopy: Principles and modern practices”, *Current protocols in cytometry*, vol. 92, no. 1, e68, Mar. 2020, ISSN: 1934-9297 (cit. on p. 10).

- [63] Lin Guo, Jia Yi Har, Jagadish Sankaran, Yimian Hong, Balakrishnan Kannan, and Thorsten Wohland, “Molecular diffusion measurement in lipid bilayers over wide concentration ranges: A comparative study”, *ChemPhysChem*, vol. 9, no. 5, pp. 721–728, Apr. 4, 2008, ISSN: 14394235 (cit. on p. 10).
- [64] Jagadish Sankaran and Thorsten Wohland, “Fluorescence strategies for mapping cell membrane dynamics and structures”, *APL Bioengineering*, vol. 4, no. 2, p. 020901, Jun. 1, 2020, ISSN: 2473-2877 (cit. on pp. 11, 62, 63).
- [65] Marie-Lena I. E. Harwardt, Marina S. Dietz, Mike Heilemann, and Thorsten Wohland, “SPT and imaging FCS provide complementary information on the dynamics of plasma membrane molecules”, *Biophysical Journal*, vol. 114, no. 10, pp. 2432–2443, May 22, 2018, ISSN: 0006-3495 (cit. on p. 11).
- [66] George E. P. Box, Gwilym M. Jenkins, Gregory C. Reinsel, and Greta M. Ljung, *Time Series Analysis: Forecasting and Control*. John Wiley & Sons, May 29, 2015, 709 pp., Google-Books-ID: rNt5CgAAQBAJ, ISBN: 978-1-118-67492-5 (cit. on p. 12).
- [67] Marco Vilela, Nadia Halidi, Sébastien Besson, Hunter Elliott, Klaus Hahn, Jessica Tytell, and Gaudenz Danuser, “Chapter nine - fluctuation analysis of activity biosensor images for the study of information flow in signaling pathways”, in *Methods in Enzymology*, ser. Fluorescence Fluctuation Spectroscopy (FFS), Part B, Sergey Y. Tetin, Ed., vol. 519, Academic Press, Jan. 1, 2013, pp. 253–276 (cit. on p. 12).
- [68] John Semmlow, “Basic concepts in signal processing”, in *Signals and Systems for Biologists*, Elsevier, 2012, pp. 35–80, ISBN: 978-0-12-384982-3 (cit. on pp. 12, 13).
- [69] John A Gubner, “PROBABILITY AND RANDOM PROCESSES FOR ELECTRICAL AND COMPUTER ENGINEERS”, p. 642, (cit. on p. 12).
- [70] Benedict Hebert, Santiago Costantino, and Paul W. Wiseman, “Spatiotemporal image correlation spectroscopy (STICS) theory, verification, and application to protein velocity mapping in living CHO cells”, *Biophysical Journal*, vol. 88, no. 5, pp. 3601–3614, May 2005, ISSN: 0006-3495 (cit. on pp. 13, 14).
- [71] P. Duhamel and M. Vetterli, “Fast fourier transforms: A tutorial review and a state of the art”, *Signal Processing*, vol. 19, no. 4, pp. 259–299, Apr. 1, 1990, ISSN: 0165-1684 (cit. on p. 14).
- [72] Matti Schneider, “A review of nonlinear FFT-based computational homogenization methods”, *Acta Mechanica*, vol. 232, no. 6, pp. 2051–2100, Jun. 1, 2021, ISSN: 1619-6937 (cit. on pp. 14, 60).
- [73] “NumPy.fft.fft2 — NumPy v1.22 manual”. (), [Online]. Available: <https://numpy.org/doc/stable/reference/generated/numpy.fft.fft2.html> (visited on 01/01/2022) (cit. on p. 14).

- [74] N O Petersen, P L Höddelius, P W Wiseman, O Seger, and K E Magnusson, “Quantitation of membrane receptor distributions by image correlation spectroscopy: Concept and application.”, *Biophysical Journal*, vol. 65, no. 3, pp. 1135–1146, Sep. 1993, ISSN: 0006-3495 (cit. on p. 14).
- [75] “Built-in fitting models in the models module — non-linear least-squares minimization and curve-fitting for python”. (), [Online]. Available: https://lmfit.github.io/lmfit-py/builtin_models.html (visited on 01/01/2022) (cit. on p. 15).
- [76] “History and license — python 3.10.1 documentation”. (), [Online]. Available: <https://docs.python.org/3/license.html> (visited on 01/09/2022) (cit. on p. 16).
- [77] Mark Lutz, *Programming Python*, Fourth edition. Beijing Boston Farnham Sebastopol Tokyo: O'Reilly, 2019, 1584 pp., ISBN: 978-0-596-15810-1 (cit. on p. 16).
- [78] “Computer programming for everybody”, Python.org. (), [Online]. Available: <https://www.python.org/doc/essays/cp4e/> (visited on 01/09/2022) (cit. on p. 16).
- [79] “NumPy”. (), [Online]. Available: <https://numpy.org/> (visited on 01/09/2022) (cit. on p. 16).
- [80] “What's new in python 3.10 — python 3.10.1 documentation”. (), [Online]. Available: <https://docs.python.org/3/whatsnew/3.10.html> (visited on 01/09/2022) (cit. on p. 16).
- [81] New England BioLabs Inc. “How gibson assembly® is changing synthetic biology | NEB”. (), [Online]. Available: <https://international.neb.com/tools-and-resources/feature-articles/gibson-assembly-building-a-synthetic-biology-toolset> (visited on 12/27/2021) (cit. on p. 23).
- [82] Pauline Sophie Löffler. “LynnLangstrumpf/master-thesis”. original-date: 2021-12-09T19:45:49Z. (Jan. 6, 2022), [Online]. Available: https://github.com/LynnLangstrumpf/Master-Thesis/releases/tag/final_master-thesis (visited on 01/07/2022) (cit. on pp. 27, 28, 30).
- [83] Christopher D. Harvey, Anka G. Ehrhardt, Cristina Cellurale, Haining Zhong, Ryohei Yasuda, Roger J. Davis, and Karel Svoboda, “A genetically encoded fluorescent sensor of ERK activity”, *Proceedings of the National Academy of Sciences*, vol. 105, no. 49, pp. 19 264–19 269, Dec. 9, 2008, Publisher: National Academy of Sciences Section: Biological Sciences, ISSN: 0027-8424, 1091-6490 (cit. on pp. 29, 35, 36, 63).
- [84] Albert J Kooistra, Stefan Mordalski, Gáspár Pándy-Szekerés, Mauricio Esguerra, Alibek Mamyrbekov, Christian Munk, György M Keserű, and David E Gloriam, “GPCRdb in 2021: Integrating GPCR sequence, structure and function”, *Nucleic Acids Research*, vol. 49, pp. D335–D343, D1 Jan. 8, 2021, ISSN: 0305-1048 (cit. on p. 31).

- [85] “Module: io — skimage v0.20.0.dev0 docs”. (), [Online]. Available: <https://scikit-image.org/docs/dev/api/skimage.io.html?highlight=imread#skimage.io.imread> (visited on 01/09/2022) (cit. on p. 44).
- [86] “Numpy.lib.format — NumPy v1.22 manual”. (), [Online]. Available: <https://numpy.org/doc/stable/reference/generated/numpy.lib.format.html#module-numpy.lib.format> (visited on 01/07/2022) (cit. on p. 47).
- [87] “Dask — dask documentation”. (), [Online]. Available: <https://docs.dask.org/en/latest/> (visited on 01/02/2022) (cit. on p. 60).
- [88] Ajit P. Yoganathan, Ramesh Gupta, and William H. Corcoran, “Fast fourier transform in the analysis of biomedical data”, *Medical & Biological Engineering*, vol. 14, no. 2, pp. 239–245, Mar. 1976, ISSN: 0025-696X, 1741-0444 (cit. on p. 60).
- [89] “Rasterization for vector graphics — matplotlib 3.6.0.dev1155+g170895612a documentation”. (), [Online]. Available: https://matplotlib.org/devdocs/gallery/misc/rasterization_demo.html (visited on 01/02/2022) (cit. on p. 60).
- [90] “Igor pro | igor pro by WaveMetrics”. (), [Online]. Available: <https://www.wavemetrics.com/products/igorpro> (visited on 01/02/2022) (cit. on p. 61).
- [91] Sally A. Kim, Katrin G. Heinze, and Petra Schwille, “Fluorescence correlation spectroscopy in living cells”, *Nature Methods*, vol. 4, no. 11, pp. 963–973, Nov. 2007, Number: 11 Publisher: Nature Publishing Group, ISSN: 1548-7105 (cit. on pp. 62, 63).
- [92] “Tissue expression of CHRM2 - summary - the human protein atlas”. (), [Online]. Available: <https://www.proteinatlas.org/ENSG00000181072-CHRM2/tissue> (visited on 01/02/2022) (cit. on p. 63).
- [93] Pauline Vandame, Corentin Spriet, Franck Riquet, Dave Trinel, Katia Cailliau-Maggio, and Jean-François Bodart, “Optimization of ERK activity biosensors for both ratio-metric and lifetime FRET measurements”, *Sensors (Basel, Switzerland)*, vol. 14, no. 1, pp. 1140–1154, Jan. 10, 2014, ISSN: 1424-8220 (cit. on p. 64).
- [94] Marion Decossas, Bertrand Bloch, and Veronique Bernard, “Trafficking of the muscarinic m₂ autoreceptor in cholinergic basalocortical neurons in vivo: Differential regulation of plasma membrane receptor availability and intraneuronal localization in acetylcholinesterase-deficient and -inhibited mice”, *Journal of Comparative Neurology*, vol. 462, no. 3, pp. 302–314, 2003, _eprint: <https://onlinelibrary.wiley.com/doi/pdf/10.1002/cne.10734>, ISSN: 1096-9861 (cit. on pp. 64, 65).
- [95] Lisa Lambert, David Dubayle, Assia Fafouri, Etienne Herzog, Zsolt Csaba, Pascal Dournaud, Salah El Mestikawy, and Véronique Bernard, “Endocytosis of activated muscarinic m₂ receptor (m₂r) in live mouse hippocampal neurons occurs via a clathrin-dependent pathway”, *Frontiers in Cellular Neuroscience*, vol. 12, p. 450, 2018, ISSN: 1662-5102 (cit. on pp. 64, 65).

Bibliography

- [96] Fadi F. Hamdan, Moulay Driss Rochdi, Billy Breton, Delphine Fessart, Douce E. Michaud, Pascale G. Charest, Stéphane A. Laporte, and Michel Bouvier, “Unraveling g protein-coupled receptor endocytosis pathways using real-time monitoring of agonist-promoted interaction between β-arrestins and AP-2 *”, *Journal of Biological Chemistry*, vol. 282, no. 40, pp. 29 089–29 100, Oct. 5, 2007, Publisher: Elsevier, ISSN: 0021-9258, 1083-351X (cit. on p. 64).
- [97] Yunan Zheng, Partha Sarathi Addy, Raja Mukherjee, and Abhishek Chatterjee, “Defining the current scope and limitations of dual noncanonical amino acid mutagenesis in mammalian cells †electronic supplementary information (ESI) available: Experimental details, supplementary data, figures and references. see DOI: 10.1039/c7sc02560b click here for additional data file.”, *Chemical Science*, vol. 8, no. 10, pp. 7211–7217, Oct. 1, 2017, ISSN: 2041-6520 (cit. on p. 66).
- [98] Radek Macháň and Thorsten Wohland, “Recent applications of fluorescence correlation spectroscopy in live systems”, *FEBS Letters*, vol. 588, no. 19, pp. 3571–3584, 2014, _eprint: <https://onlinelibrary.wiley.com/doi/pdf/10.1016/j.febslet.2014.03.056>, ISSN: 1873-3468 (cit. on p. 66).
- [99] Yulin Tian, Ming Fang, and Qing Lin, “Intracellular bioorthogonal labeling of glucagon receptor via tetrazine ligation”, *Bioorganic & Medicinal Chemistry*, vol. 43, p. 116 256, Aug. 1, 2021, ISSN: 0968-0896 (cit. on p. 66).